

**COMPUTATIONAL PROBE OF AN ALKYLATING PRODRUG:
TEMOZOLOMIDE AND ITS DERIVATIVES**

**A THESIS SUBMITTED IN PARTIAL FULFILLMENT OF THE
REQUIREMENTS FOR THE DEGREE OF DOCTOR OF
PHILOSOPHY**

DIPANTA GOGOI

MZU REGISTRATION NO. : 88 of 2014

Ph. D. REGISTRATION NO. : MZU/Ph. D./1006 of 15.05.2017



**DEPARTMENT OF CHEMISTRY
SCHOOL OF PHYSICAL SCIENCES
AUGUST, 2022**

**COMPUTATIONAL PROBE OF AN ALKYLATING PRODRUG:
TEMOZOLOMIDE AND ITS DERIVATIVES**

BY

DIPANTA GOGOI
Department of Chemistry

Under the supervision of
Dr. ZODINPUIA PACHUAU

Submitted
In partial fulfillment of the requirement of the Degree of Doctor of Philosophy in
Chemistry of Mizoram University, Aizawl.

MIZORAM UNIVERSITY
(A central University under the Act of Parliament)
Department of Chemistry
School of Physical Sciences

Dr. Zodinpuia Pachuau
Associate Professor

CERTIFICATE

This is to certify that the thesis entitled “*Computational Probe of an Alkylating Prodrug: Temozolomide and its Derivatives*” submitted by *Mr. Dipanta Gogoi*, for the degree of *Doctor of Philosophy* in the Mizoram University, Aizawl, Mizoram, embodies the record of original investigations carried out by him under my supervision. He has been duly registered and the thesis presented is worthy of being considered for the award of the Ph.D. degree. This work has not been submitted for any degree in any other university.

Dated : August 2, 2022

(Dr. ZODINPUIA PACHUAU)
Supervisor

Declaration of the Candidate

Mizoram University

August, 2022

I, Dipanta Gogoi, hereby declare that the subject matter of this thesis is the record of work done by me, that the contents of this thesis did not form basis of the award of any previous degree to me or to do the best of my knowledge to anybody else, and that the thesis has not been submitted by me for any research degree in any other University/ Institute.

This is being submitted to the Mizoram University for the degree of Doctor of Philosophy in Chemistry.

(DIPANTA GOGOI)

Candidate

(Prof. N. MOHANDAS)

Head

(Dr. ZODINPUIA PACHUAU)

Supervisor

ACKNOWLEDGEMENT

At the outset, I would like to thank almighty God for giving me the strength, power and wisdom to accept this research study and complete the research work with sincerity and dedication. By the grace of God, this achievement has been possible.

The journey of my research work begins wherein I found a teacher, a mentor, an inspirational model, a source of strength and a pillar of support in my supervisor, Dr. Zodinpuia Pachuau, Associate Professor, Department of Chemistry, Mizoram University for his immense support, motivation, and patience for my Ph.D study and allied research work. His constance guidance has been a key element to me in completing the research work and in drafting the thesis in a better way. His believe in me has been an inspiration during the tenure of research study and his knowledgeable advice has mould me to be a better person in the society.

I sincerely thank and give respect to Prof. Muthukumaran, R., Head, Department of Chemistry, MZU, for his constant encouragement and useful advice offered me throughout my academic career in the University.

I extend my valuable and sincere thanks to all the teaching, Dr. N. Mohandas Singh, Dr. Bimolini Devi, Dr. R. Lalrempuia, Dr. Joydeep Das, Dr. Manjeet Singh and non-teaching staff, Mr. Brojendro Singh Shagolsem, Sr. Laboratory Technician, and Mr. John Vanlalhraia, Technical Assistant, Department of Chemistry, Mizoram University for their immeasurable suggestions and support has motivate me during my research work.

The continuous encouragement received from Prof. Diwakar Tiwari, Dean, School of Physical sciences, Mizoram University is also to be acknowledged.

I also thank Dr. Ved Prakash Singh, Associate Professor, Department of Industrial Chemistry, Mizoram University for his continuous encouragement through out my academic career in the University.

I thank my fellow labmates and colleagues for their constant support, help and standing by my side at high and low pace of my life. Their immense contribution in my life shall always be remembered.

Last but not the least; I extend my sincere thanks and gratitude to my parents, brother and other family members for supporting and guiding me spiritually and religiously in drafting the thesis and my life in particular. I am thankful to all the well-wishers who have guided and motivated me throughout my research life.

Thank you God for everything.

(DIPANTA GOGOI)

TABLE OF CONTENTS

Title of the Thesis
Certificate
Declaration of the Candidate
Acknowledgement
Table of Contents
List of Figures
List of Tables

CHAPTER 1

INTRODUCTION

1.1	Background	1
1.2	Chemistry of temozolomide bio-synthesis	4
1.3	Resistance mechanisms	5
1.4	Literature review	6
1.5	Research aim and objectives of the present work	7

CHAPTER 2

THEORETICAL METHODOLOGY

2.1	Theoretical Methods	9
2.1.1	Quantum Mechanics	9

2.1.1	Density Functional Theory	9
2.1.2	The Kohn-Sham approach	9
2.1.3	Basis set effects	12
2.1.4	Slater and Gaussian type orbitals	12
2.1.5	Pople style basis sets	13
2.2	Geometry Optimization	13
2.3	Gaussian-Software Overview	14
2.4	GaussView Software Overview	15
2.5	Molecular Docking study	16

CHAPTER 3: RESULT AND DISCUSSION

THEORETICAL STUDY OF TEMOZOLOMIDE BY DENSITY FUNCTIONAL THEORY

3.1	Introduction:	18
3.2	Temozolomide	18
3.2.1	Potential Energy surface scan analysis	18
3.2.2	Optimization and properties in both media:	20
3.2.3	Geometrical parameters	21
3.2.4	Atomic charges and MEP	23
3.2.5	^1H and ^{13}C NMR analysis	25
3.2.6	UV-vis analysis	26
3.2.7	Natural Bond Orbital Analysis:	27

3.2.8	Frontier Molecular Orbital Analysis	29
3.2.9	Vibrational Assignment	31
3.3	Conclusion	37

CHAPTER 4: RESULT AND DISCUSSION

ELECTRONIC AND SPECTROSCOPIC DFT STUDY OF TEMOZOLOMIDE WITH BENZYL ISOTHIOCYANATE (BITC)

4.1	Introduction:	38
4.2	TMZ-BITC(1)	41
4.2.1	Optimization and properties in both media	41
4.2.2	Geometrical parameters	41
4.2.3	Atomic charges and MEP	44
4.2.4	UV-vis analysis	48
4.2.5	Frontier Molecular Orbitals analysis (FMO)	49
4.2.6	Natural bond orbital (NBO) analysis	51
4.2.7	Vibrational Assignment	53
4.3	TMZ-BITC(2)	60
4.3.1	Optimization and properties in both media:	60
4.3.2	Geometrical parameters	61
4.3.3	Atomic charges and MEP	63
4.3.4	UV-vis analysis.	67
4.3.5	Frontier Molecular Orbitals analysis (FMO)	69

4.3.6	Natural bond orbital (NBO) analysis	70
4.3.7	Vibrational Assignment	72
4.4	TMZ-BITC(3)	80
4.4.1	Optimization and properties in both media:	80
4.4.2	Geometrical parameters	81
4.4.3	Atomic charges and MEP	84
4.4.4	UV-vis analysis	87
4.4.5	Frontier Molecular Orbitals analysis (FMO)	89
4.4.6	Natural bond orbital (NBO) analysis	91
4.4.7	Vibrational Assignment	93
4.5	TMZ-BITC(4)102	
4.5.1	Optimization and properties in both media	102
4.5.2	Geometrical parameters	104
4.5.3	Atomic charges and MEP	106
4.5.4	UV-vis analysis	110
4.5.5	Frontier Molecular Orbitals analysis (FMO)	111
4.5.6	Natural bond orbital (NBO) analysis	113
4.5.7	Vibrational Assignment	115
4.6	Conclusion	124

CHAPTER 5: RESULT AND DISCUSSION

PHARMACOLOGICAL AND MOLECULAR DOCKING INVESTIGATIONS

5.1	Molecular Docking study	125
5.1.1	Ligand preparation:	125
5.1.2	Protein preparation:	125
5.1.3	Protein-ligand docking:	125
5.1.4	Analysis of interactions between ligands and protein	125
5.1	PASS biological activity prediction	130
5.2	InsilicoADMETprediction	132
5.3	Conclusion:	134

CHAPTER 6

6 SUMMARY AND CONCLUSION135

7 REFERENCES137

List of Publications

Conferences and Symposium

BIO-DATA

PARTICULARS OF THE CANDIDATE

LIST OF FIGURES

Figures	Page No.
Figure 1.1 : Temozolomide	3
Figure 1.2 : Decomposition of temozolomide in aqueous solution (Adopted from Newlands <i>et al.</i> , 1997)	4
Figure 3.1: Confirmation analysis of TMZ.	19
Figure 3.2: Optimized structure of TMZ at B3LYP/6-311++G(d,p) basis set. (a) gas phase (b) aqueous solution	19
Figure 3.3: Graph showing the trends for Mulliken and Natural Population Analysis (NPA) Atomic charges of TMZ in the gas phase (upper) and the aqueous phase (bottom).	24
Figure 3.4: Calculated electrostatic potential surfaces on the molecular surface of TMZ (0.0027 a.u.) in the gas phase using 6-311++G(d,p) basis set.	25
Figure 3.5: UV spectra of TMZ calculated at B3LYP/6-311++G(d,p) basis set	27
Figure 3.6: HOMO-LUMO diagram of TMZ	30
Figure 3.7: Comparative analysis between experimental and DFT FT-IR spectra of TMZ.	32
Figure 4.1: Optimized structure of TMZ-BITC(1) at B3LYP/6-311++G(d,p) basis set for gas phase (upper) and aqueous phase (bottom)	42
Figure 4.2: Graph showing the trends for Mulliken and Natural Population Analysis (NPA) Atomic charges of TMZ-BITC(1) in the gas phase (upper) and the aqueous solution (bottom).	46
Figure 4.3: Calculated electrostatic potential surfaces on the molecular surface of TMZ-BITC(1) in the gas phase, using 6-311++G(d,p) basis set.	47
Figure 4.4: UV spectra of TMZ-BITC(1) calculated at B3LYP/6-311++G(d,p) basis set.	49
Figure 4.5: HOMO-LUMO graphical reproduction of TMZ-BITC(1)	51
Figure 4.6: DFT FT-IR spectra of TMZ-BITC(1).	53
Figure 4.7: Optimized structure of TMZ-BITC(2) at B3LYP/6-311++G(d,p) basis set. (a) gas phase (b) aqueous solution	61
Figure 4.8: Graph showing the trends for Mulliken and Natural Population Analysis (NPA) Atomic charges of TMZ-BITC(2) in the gas phase (upper) and the aqueous solution (bottom).	64
Figure 4.9: Calculated electrostatic potential surfaces on the molecular surface of TMZ-BITC(2) in the gas phase, using 6-311++G(d,p) basis set.	66
Figure 4.10: UV spectra of TMZ-BITC(2) calculated at B3LYP/6-311++G(d,p) basis set	68
Figure 4.11: HOMO-LUMO graphical reproduction of TMZ-BITC(2)	69
Figure 4.12: DFT FT-IR spectra of TMZ-BITC(2).	73
Figure 4.13: Optimized structure of TMZ-BITC(3) at B3LYP/6-311++G(d,p) basis set for gas phase (upper) aqueous solution (bottom).	81

Figure 4.14: Calculated electrostatic potential surfaces on the molecular surface of TMZ-BITC(2) in the gas phase, using 6-311++G(d,p) basis set.	84
Figure 4.15: Graph showing the trends for Mulliken and Natural Population Analysis (NPA) Atomic charges of TMZ-BITC(3) in the gas phase (upper) and the aqueous solution (bottom).	85
Figure 4.16: UV spectra of TMZ-BITC(3) calculated at B3LYP/6-311++G(d,p).	89
Figure 4.17: HOMO-LUMO graphical reproduction of TMZ-BITC(3)	90
Figure 4.18: DFT FT-IR spectra of TMZ-BITC(3).	93
Figure 4.19: Optimized structure of TMZ-BITC(4) at B3LYP/6-311++G(d,p) basis set in gas phase (up) aqueous solution (bottom)	103
Figure 4.20: Calculated electrostatic potential surfaces on the molecular surface of TMZ-BITC(4) in the gas phase, using 6-311++G(d,p) basis set.	106
Figure 4.21: Graph showing the trends for Mulliken and Natural Population Analysis (NPA) Atomic charges of TMZ-BITC(4) in the gas phase (upper) and the aqueous solution (bottom).	108
Figure 4.22: UV spectra of TMZ-BITC(4) calculated at B3LYP/6-311++G(d,p).	111
Figure 4.23: HOMO-LUMO graphical reproduction of TMZ-BITC(4)	112
Figure 4.24: DFT FT-IR spectra of TMZ-BITC(4).	115
Figure 5.1: 3D Structure of target protein complex PDB ID: IQH4 from PDB Bank	127
Figure 5.2: 3D and 2D binding mode of compound TMZ in the active site cavity of IQH4 protein.	128
Figure 5.3: 3D and 2D binding mode of compound TMZ-BITC(1) in the active site cavity of IQH4 protein.	128
Figure 5.4: 3D and 2D binding mode of compound TMZ-BITC(2) in the active site cavity of IQH4 protein.	129
Figure 5.5: 3D and 2D binding mode of compound TMZ-BITC(3) in the active site cavity of IQH4 protein.	129
Figure 5.6: 3D and 2D binding mode of compound TMZ-BITC(4) in the active site cavity of IQH4 protein.	130

LIST OF TABLES

Tables	Page No.
Table 3.1: Calculated total energies (E), dipole moments (μ), and volumes (V) for compound TMZ in gas and aqueous phase phases by using B3LYP/6-311 ++ G(d,p) basis set.	20
Table 3.2: Selected geometrical parameters of TMZ using B3LYP/6-311++G(d,p) basis set.	21
Table 3.3: Mulliken, Natural Population Analysis (NPA) charges (in a.u.) and Molecular Electrostatic Potentials (MEP) of TMZ in the gas phase and aqueous solution calculated at B3LYP/6-311++G(d,p) level of theory.	23
Table 3.4: Experimental and theoretical chemical shifts of TMZ calculated in GIAO method using DMSO as solvents.	26
Table 3.5: Electronics properties of TMZ calculated using TD-DFT (B3LYP)/6-311++G(d,p)	27
Table 3.6. Second-order perturbation theory analysis of Fock matrix in NBO of TMZ.	29
Table 3.7. Frontier Molecular Orbitals energy parameters and global reactivity descriptors of TMZ	31
Table 3.8: Vibrational assignments of TMZ fundamental modes along with calculated IR and PED using the B3LYP method.	34
Table 4.1: Calculated total energies (E), dipole moments (μ), and volumes (V) for compound TMZ-BITC(1) in gas and aqueous phase phases by using B3LYP/6-311++ G(d,p) basis set.	41
Table 4.2: Selected geometrical parameters of TMZ-BITC(1) using B3LYP/6-311++G(d,p) basis set.	43
Table 4.3: Mulliken, Natural Population Analysis (NPA) charges (in a.u.) and Molecular Electrostatic Potentials (MEP) of TMZ-BITC(1) in the gas phase and aqueous solution calculated at B3LYP/6-311++G(d,p) level of theory.	45
Table 4.4: Experimental and theoretical chemical shifts of TMZ-BITC(1) calculated in GIAO method using DMSO as solvents.	48
Table 4.4: Electronics properties of TMZ-BITC(1) calculated using TD-DFT (B3LYP)/6-311++G(d,p).	49
Table 4.5: Frontier Molecular Orbitals energy parameters and global reactivity descriptors of TMZ-BITC(1).	50
Table 4.6: Second-order perturbation theory analysis of Fock matrix in NBO of TMZ-BITC(1).	52
Table 4.7: Vibrational assignments of TMZ-BITC(1) fundamental modes along with calculated IR and PED using the B3LYP method.	56
Table 4.8: Calculated total energies (E), dipole moments (μ), and volumes (V) for compound TMZ-BITC(2) in gas and aqueous phases using B3LYP/6-311++ G(d,p) basis set.	60

Table 4.9: Selected geometrical parameters of TMZ-BITC(2) using B3LYP/6-311++G(d,p) basis set.	62
Table 4.10: Mulliken, Natural Population Analysis (NPA) charges (in a.u.) and Molecular Electrostatic Potentials (MEP) of TMZ-BITC(2) in the gas phase and aqueous solution calculated at B3LYP/6-311++G(d,p) level of theory.	65
Table 4.12: Experimental and theoretical chemical shifts of TMZ-BITC(2) calculated in GIAO method using DMSO as solvents.	66
Table 4.11: Electronics properties of TMZ-BITC(2) calculated using TD-DFT (B3LYP)/6-311++G(d,p)	68
Table 4.12: Frontier Molecular Orbitals energy parameters and global reactivity descriptors of TMZ-BITC(2).	70
Table 4.13: Second-order perturbation theory analysis of Fock matrix in NBO of TMZ-BITC(2).	71
Table 4.14: Vibrational assignments of TMZ-BITC(2) fundamental modes along with calculated IR and PED using the B3LYP method.	75
Table 4.15: Calculated total energies (E), dipole moments (μ), and volumes (V) for compound TMZ-BITC(3) in gas and aqueous phase phases by using B3LYP/6-31++ G(d,p) basis set.	80
Table 4.16: Selected geometrical parameters of TMZ-BITC(3) using B3LYP/6-311++G(d,p) basis set.	82
Table 4.17: Mulliken, Natural Population Analysis (NPA) charges (in a.u.) and Molecular Electrostatic Potentials (MEP) of TMZ-BITC(3) in the gas phase and aqueous phase calculated at B3LYP/6-311++G(d,p) level of theory.	86
Table 4.20: Experimental and theoretical chemical shifts of TMZ-BITC(3) calculated in GIAO method using DMSO as solvents.	87
Table 4.18: Electronics properties of TMZ-BITC(3) calculated using TD-DFT (B3LYP)/6-311++G(d,p)	88
Table 4.19: Frontier Molecular Orbitals energy parameters and global reactivity descriptors of TMZ-BITC(3)	90
Table 4.20: Second-order perturbation theory analysis of Fock matrix in NBO of TMZ-BITC(3).	92
Table 4.21: Vibrational assignments of TMZ-BITC(3) fundamental modes along with calculated IR and PED using the B3LYP method.	96
Table 4.22: Calculated total energies (E), dipole moments (μ), and volumes (V) for compound TMZ-BITC(4) in gas and aqueous phase phases by using B3LYP/6-311++ G(d,p) basis set.	102
Table 4.23: Selected geometrical parameters of TMZ-BITC(4) using B3LYP/6-311++G(d,p) basis set.	104

Table 4.24: Mulliken, Natural Population Analysis (NPA) charges (in a.u.) and Molecular Electrostatic Potentials (MEP) of TMZ-BITC(4) in the gas phase and aqueous phase calculated at B3LYP/6-311++G(d,p) level of theory.	107
Table 4.28: Experimental and theoretical chemical shifts of TMZ-BITC(4) calculated in GIAO method using DMSO as solvents.	109
Table 4.25: Electronics properties of TMZ-BITC(4) calculated using TD-DFT (B3LYP)/6-311++G(d,p)	110
Table 4.26: Frontier Molecular Orbitals energy parameters and global reactivity descriptors of TMZ-BITC(4).	113
Table 4.27: Second-order perturbation theory analysis of Fock matrix in NBO of TMZ-BITC(4).	114
Table 4.28: Vibrational assignments of TMZ-BITC(4) fundamental modes along with calculated IR and PED using the B3LYP method.	118
Table 5.1: Binding energy and hydrogen bond distance parameter for TMZ and its derivatives on binding with IQH4 protein.	127
Table 5.2: In silico PASS prediction of studied compounds obtained through Pass online tool	131
Table 5.3: In silico ADMET prediction of Drug-likeness and Toxicity of TMZ and its BITC derivatives.	133

1 INTRODUCTION

1.1 Background

The most frequently diagnosed primary tumor in the central nervous system is glioma, further classified as astrocytoma, oligodendroglioma, or ependymoma, depending on histological and genetic features(Louis *et al.*, 2016). The annual incidence of malignant gliomas is about 5 cases per 100,000 person-years (Bolly *et al.*, 2021; Patel *et al.*, 2019). The most common of all malignant central nervous system (CNS) tumors is glioblastoma multiforme (GBM; 48.3%), which accounts for approximately 41.8% to 57.3% of gliomas(Ostrom *et al.*, 2019). Despite continuous innovation in glioma diagnosis and treatment concepts, with more precise surgery and the continuous emergence of drugs, the overall prognosis of patients with malignant glioma remains poor. The median overall survival times for low-grade glioma, anaplastic glioma, and GBM are 78.1, 37.6, and 14.4 months, respectively(Jiang *et al.*, 2021; Yang *et al.*, 2013). The patients still face high risks of recurrence and death after surgical treatment with a poor prognosis(Miwa *et al.*, 2019). Age is also a key factor associated with the incidence and survival of all cancers, and therefore it is also an important factor in the incidence and survival of gliomas(Lin *et al.*, 2020).

In order to further improve the survival rate of patients, radiotherapy is often selected as adjuvant therapy in clinical practice. However, radiotherapy cannot increase the tumor-free survival time of patients. Sole radiotherapy has a minimal effect since some patients still have a recurrence after radiotherapy(Diehl *et al.*, 2018; Furukawa *et al.*, 2018; Gjika *et al.*, 2020). Currently, the majority of GBM treatments are maximum safe resection with adjuvant chemoradiotherapy, which results in a moderate 14-month overall survival rate(Delgado-López & Corrales-García, 2016)

Temozolomide (TMZ) represents a new class of second-generation imidazotetrazine prodrugs that undergo spontaneous conversion under physiological conditions to the active alkylating agent monomethyl 5-triazine imidazole

carboxamide (MTIC) (M. F. Stevens *et al.*, 1987). TMZ(**Figure 1.1**) is a DNA alkylating agent that was first discovered to have anti-tumorigenic effects in the 1940s and became the first drug to be used in chemotherapeutics(Arora & Somasundaram, 2019). This prodrug TMZ or by the Generic name dacarbazine [Trade name: DTIC-Dome^(R) and other names are DIC, imidazole, and carboxamide] is able to cross the blood-brain barrier and can be administered orally(Moody & Wheelhouse, 2014a). Above pH 7, TMZ undergoes ring-opening decomposition to the active compound MTIC with water at the electropositive C4 atom of temozolomide, 5-(3-monomethyl-(triazen-1-yl)imidazole-4-carboxamide) which is then transformed to AIC, 5-aminoimidazole-4-carboxamide by-product (Tsang *et al.*, 1990). MTIC degrades to a highly reactive methyl diazonium cation, which transfers the methyl group to bind with the O-6 position of guanine for cell apoptosis(Arrowsmith *et al.*, 2002; Clark *et al.*, 1995; Darkes *et al.*, 2002). However, TMZ resistance has been a significant problem in malignant glioma, where the cytoprotective DNA repair protein, O6-alkylguanine-DNA alkyltransferase(AGT), transfers the methyl adducts at O6-guanine to a cysteine acceptor residue(Larkin *et al.*, 2007; Tolcher *et al.*, 2003). TMZ affects single strands of DNA at specific sites; it preferentially methylates DNA at the N7 position of guanine, O3 position of adenine and O6 position of guanine(Friedman *et al.*, 2000b).

One issue with using TMZ to treat GBM patients is that their tumors may evolve TMZ resistance due to alteration not only in their expression of DNA alkylating proteins and DNA repair enzymes but also in cell signaling pathways(S. Y. Lee, 2016). The direct repair of O6-MeG by the enzyme in the normal cells removes the methyl adduct, resulting in the restoration of guanine. During DNA replication, O6-MeG mispairs with thymine instead of cytosine in MGMT-deficient cells.This signals the DNA mismatch repair(MMR) pathway, which selectively identifies the mispaired thymine on the daughter strand and excises it, while the O6-MeG remains in the template strand(Karran & Hampson, 1996).

The combination of anticancer drugs with distinct mechanisms of action, selective drug release, and convection-enhanced delivery may represent a translational strategy for the treatment of TMZ-resistant gliomas(Wang *et al.*, 2021).

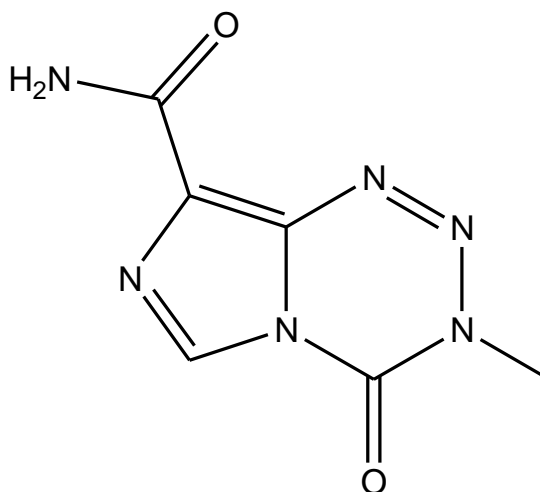


Figure 1.1 : Temozolomide

Gaussian16 package software was used for the computational work of the research work. Computations were carried out in the gas phase and in the solvent phase. Initial calculations of the stationary point geometry were carried out in the ground states, which were correlated with the excited states using the Hartree Fock (HF) and the Density Functional Theory (DFT). To obtain accurate results with inference to experimental results, Post Hartree Fock Methods were employed in the course of the investigation. The computational challenge lies in the selective choice of appropriate basis functions and the basis of the theoretical background, in line with the approach of the research chemical systems. This is to imbibe a realistic understanding of the structural modifications or group introductions of alkylating agents, TMZ to circumnavigate AGT/MGMT mediated resistance to TMZ and without nullifying the cytotoxicity of TMZ using certain quantum-chemical parameters such as HOMO-LUMO energies, the heat of formations and ionisation potentials as described by FIsayev in 2006[FIsayev et. al., (2006)].

Gaussian 16 package can serve as a powerful tool for exploring areas of chemical interest like structural reactivity, stabilities, structural effects and sensitivity upon substitutions, reaction mechanisms in the potential energy surfaces, and excitation energies. Computational methods also provide theoretical spectroscopic outputs, which may be compared with experimental results in substantiating the foundation of computational chemical research.

For new drug design and discovery projects, molecular docking methods are widely used in the scientific community to provide a fast and economic alternative to standardized experimental techniques[(F Sousa *et al.*, 2010; Yuriev *et al.*, 2015)]. The conceptual method is to predict the experimental binding modes and affinities of the ligand within the binding site of a particular targeted protein to find the correct binding poses in predicting accurate binding affinity(Heo *et al.*, 2014; Shin *et al.*, 2013)].

1.2 Chemistry of temozolomide bio-synthesis

When temozolomide is hydrolyzed, the first product is the methyl triazene-MTIC which ultimately transfers its methyl group to a nucleophile. The mechanism of the reaction of temozolomide in an aqueous solution is shown in **Figure 1.2**.

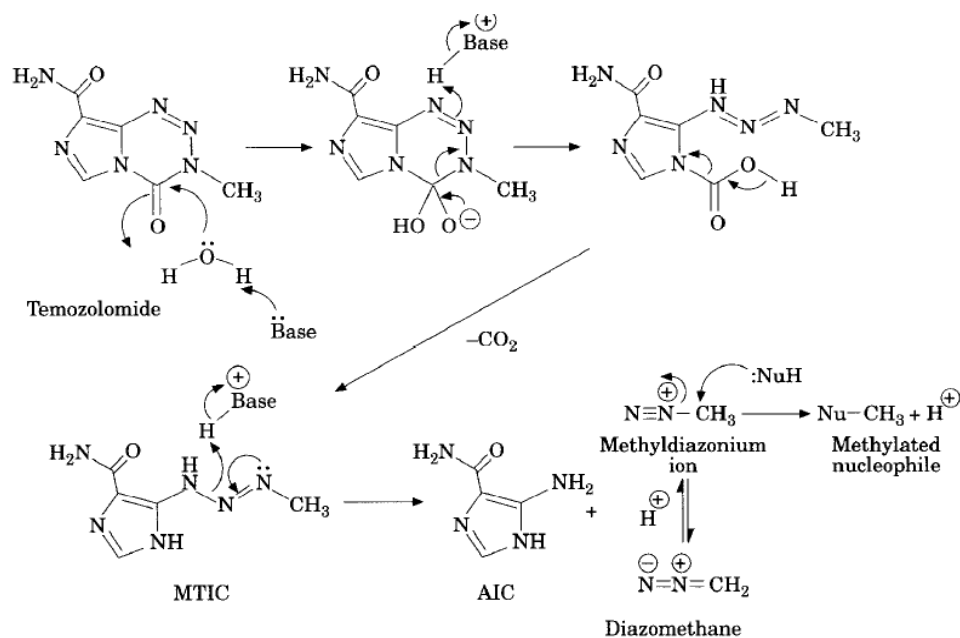


Figure 1.2 : Decomposition of temozolomide in aqueous solution (Adopted from Newlands *et al.*, 1997)

The rate-limiting step is the base-catalyzed addition of water to C-4 to form a tetrahedral intermediate, which collapses with a breakdown of the tetrazinone ring followed by spontaneous decarboxylation. The further reaction of MTIC requires acid catalysis and the fragmentation of the triazene forms the fugitive methyl diazonium ion. In deuterated buffer solutions, the methyl diazonium cation is in

equilibrium with diazomethane which has been identified by the appearance of H¹-H² couplings when the reaction was monitored by H¹-NMR(Denny *et al.*, 1994; Wheelhouse & Stevens, 1993).

The final step is the reaction of methyl diazonium with a nucleophile in solution, either with water or components of the buffer, whereas biological (and clinical) activity depends on the transfer of the methyl group to DNA. N-2 and N-3 are lost as a molecule of dinitrogen; the C-4 carbon-bearing an oxygen atom is converted to CO; N-1 and all the imidazole atoms are excreted as a molecule of 5-aminoimidazole- 4-carboxamide (AIC), a natural constituent of urine. Conversion of the carboxamide group of temozolomide to a carboxylic acid residue, monitored by using a drug labeled with ¹⁴C in the C-6 position, is a minor metabolic pathway(Tsang *et al.*, 1990). The temozolomide molecule can therefore be considered as a drug-delivery device exquisitely adapted to deliver a methylating fragment to DNA.

1.3 Resistance mechanisms

Temozolomide resistance is considered to be mediated by two distinct repair mechanisms; AGT and DNA mismatch repair proteins.

The methyl adduct is transferred to a cysteine residue on AGT in a single-step error-free reversal of damage reaction for O6-methylguanine. In vitro, the concentration of this enzyme in the cell is a key determinant of temozolomide cytotoxicity.(Graziani *et al.*, 1995; Wedge, Porteous, May, *et al.*, 1996). The enzyme's function in the cytotoxicity of chloroethylnitrosoureas attracted attention in AGT cellular concentrations in malignant glioma. Concentrations were higher in benign and chemoresistant central nervous system tumours such as meningiomas and neurinomas, but lower in chemosensitive tumours like oligodendrogliomas and anaplastic oligodendrogliomas(Wiestler *et al.*, 1984). In a study of 167 glioma and anaplastic astrocytoma samples, 26% exhibited no detectable AGT activity. Patients with glioblastomas and anaplastic astrocytomas having low amounts of AGT had considerably better survival than those having high concentrations of the enzyme. Low expression of AGT (detection in less than 20% of cells) was detected in 70% of tumours in a series of 38 patients with newly diagnosed glioblastoma and anaplastic

astrocytoma treated with temozolomide after surgery and before radiotherapy(Friedman *et al.*, 1998). Patients with glioma who had a methylated promoter, which inactivated AGT, had a considerably greater survival rate when administered carmustine chemotherapy than those who had a non-methylated AGT promoter.

Mismatch repair mutations in colon cancer cell lines render resistant to TMZ, and AGT depletion cannot overcome the resistance(Esteller *et al.*, 2000). A deficiency in MLH1, a critical mismatch repair protein, was found to be an important predictor of TMZ resistance in a panel of paediatric xenograft tumours(Middlemas *et al.*, 2000). A combination of low AGT concentrations and high mismatch repair protein concentrations could be predicted to identify the majority of TMZ responders. The nuclear enzyme poly-ADP-ribose polymerase is another cell target that can increase temozolomide's cytotoxicity. This enzyme detects DNA strand breaks and aids in their repair. 3-aminobenzamide, a poly-ADP-ribose polymerase inhibitor, increases the potency of TMZ *in vitro*(Wedge, Porteous, & Newlands, 1996).

1.4 Literature review

The discovery of TMZ is the symbiotic relationship between the laboratory sciences of chemistry and pharmacology(Newlands *et al.*, 1997a). The presence of arrays of nitrogen atoms, which confer unique chemical and biological properties, is a common feature of TMZ, spanning pyrazolo-1,2,4-triazines and aryl dimethyltriazenes in the early 1960s to TMZ of the mid-1990s (M. F. G. Stevens & Newlands, 1993). Between these two milestones, the antimelanoma drug dacarbazine entered clinical practice in the 1970s on the basis of its potent activity against a range of rodent tumours. However, DTIC requires metabolic activation in the liver to 5-(3-methyltriazene-1-yl)imidazole-4-carboxamide (MTIC)(Mizuno & Decker, 1976), and the modest performance of the drug in the clinic probably reflects the poor distribution of the active metabolite MTIC in man. In 1980, Robert Stone, a research student at Aston University sponsored by (the then) May & Baker Ltd, synthesized the first examples of a new ring-system imidazo[5, I-d]-1,2,3,5-tetrazine which, consistent with the molecular lineage of past products of the Aston group, possessed

a bicyclic ring-system with multiple nitrogen atoms (any more might have rendered the construct dangerously unstable)(M. F. Stevens *et al.*, 1984). The lead compound mitozolomide (formerly azolastone) entered the clinic with high hopes in 1983, and a Phase I trial was completed by 1985. Unfortunately, despite its curative activity in many rodent tumour models(Hickman *et al.*, 1985), mitozolomide showed only limited clinical activity and elicited unpredictable and severe myelo-suppression(Newlands *et al.*, 1985). At this stage, the program, now lacking an industrial sponsor, might have observed, but the Cancer Research Campaign Phase I/II Sub-committee showed sufficient confidence to consider the clinical testing of the N-methyl congener of mitozolomide with a demonstrably different toxicological profile. Whereas mitozolomide cross-linked DNA(Gibson *et al.*, 1984) , the methylating agent TMZ is a monofunctional agent which has good tissue distribution and was shown to be schedule-dependent in terms of its antitumour activity(M. F. Stevens *et al.*, 1987). Additionally, TMZ is a neat and robust molecule, stable at acid pH, allowing it to be absorbed intact after oral administration(Newlands *et al.*, 1992), and has excellent bio-distribution, including penetration into the central nervous system. The therapeutic effect of TMZ is dependent on the presence of DNA mismatch repair (MMR) proteins(Ramirez *et al.*, 2013). A study of molecular modelling studies of the inclusion complex of anticancer medication TMZ with Cucurbit[7]uril in vacuum and water using DFT and DFT-D functionals revealed a deep insertion of the imidazole ring of TMZ into the hydrophobic Cucurbit[7]uril cavity, where the amide group is bounded to portal ureido oxygen, and only a portion of the tetrazinone moiety and the methyl group protrude outside the cavity(Yahiaoui *et al.*, 2021).

1.5 Research aim and objectives of the present work

The current research work aims to study the electronic and spectroscopic study of TMZ and its BITC derivatives by implementing density functional theory (DFT) using B3LYP/6-311++G(d,p) level of theory. To study the spectral analysis of FT-IR by frequency calculation and UV-vis by time-dependent DFT calculations. In addition to global and local reactivity descriptors analysis, HOMO-LUMO energies,

the molecular electrostatic potential to study the stability of the titled molecule with prospective bioactive potency.

2 THEORETICAL METHODOLOGY

2.1 Theoretical Methods

The calculations of electronic structure approaches are based on quantum mechanics principles.

2.1.1 Quantum Mechanics

The starting point of quantum mechanics is the time-independent Schrödinger wave equation:

$$\left\{ -\frac{\hbar}{2m} \left(\frac{\partial^2}{\partial x^2} + \frac{\partial^2}{\partial y^2} + \frac{\partial^2}{\partial z^2} \right) + V \right\} \psi(r) = E\psi(r) \quad \text{Eqn (1)}$$

where m is the mass of an electron, V is the external field, \hbar is Planck's constant divided by 2π , E is the energy of the particle, ψ is a wave function which characterizes the motion of the particle, and $r = xi + yj + zk$ is the position vector

2.1.1 Density Functional Theory

Density functional theory has been the dominating method for the quantum mechanical modelling of periodic systems (Parr & Wang 1989, Jensen 1999). In recent years it has also been embraced by quantum chemists and is currently very commonly utilized for the modelling of energy surfaces in molecules. Density functional theory is an approach to the electronic structure of atoms and molecules.

2.1.2 The Kohn-Sham approach

In density functional theory (DFT), the total energy, including electron correlation effects (Hohenberg & Kohn, 1964; Kohn & Sham, 1965; Parr & Yang, 1989), is written in the form:

$$E[\rho(r)] = T[\rho(r)] + U[\rho(r)] + E_{xc}[\rho(r)] \quad \text{Eqn (2)}$$

Here, T is a kinetic energy term, U is the electrostatic interaction energy between all electrons and nuclei, and E_{xc} is the exchange-correlation energy of

the system. The total electron density ρ in **Eqn (2)** can be related to single-particle wave functions by

$$\rho(r) = \sum_{occ} |\psi(r)|^2 \quad \text{Eqn (3)}$$

Where the summation extends over all occupied electronic levels.

Density functional theory is based on the Hohenberg-Kohn theorem, which states that the combined energy of a system in its ground state is a function of its electronic density, $\rho(r)$, and that any density, $\rho'(r)$, other than the true density will always result in higher energy (Jensen, 2017; St-Amant, 1996; Ziegler, 1991). As a result, the Hohenberg-Kohn theorem introduces a new method for computing precise, variational *ab initio* electronic structure calculations. In standard *ab initio* methodology, Schrödinger's equation is given by:

$$H\psi = E\psi \quad \text{Eqn (4)}$$

Meanwhile, DFT needs to minimize the energy functional, $E[\rho]$. The benefit of this conceptual simplification cannot be emphasized. DFT helps to deal with a simple three-dimensional function, the overall electronic density, rather than a complex $3N$ dimensional wavefunction representing the behaviour of each electron in an N -electron system. Unfortunately, the exact nature of the energy functional is unknown; therefore, when a trial density, $\rho'(r)$, is provided as input, the overall energy of a system cannot be easily output. As a result, we'll have to resort to approximation DFT approaches, and because we won't have a wavefunction, we'll have to rely on one-electron Kohn-Sham molecular orbitals, which are very similar to molecular orbitals from the well-known Hartree-Fock (HF) method (Hehre & Radom, 1986; Szabo & Ostlund, 2012).

Early DFT applications were mostly limited to the physics community, focusing on systems where the HF approximation is a particularly poor starting point (Dahl & Avery, 2013). Because a single determinant technique is usually unsatisfactory in such instances, the large majority of the applications were on metallic systems. As DFT works with the density rather than the wavefunction, systems that would require a large number of electronic configurations to be

accurately characterized by traditional *ab initio* methods are neither harder nor more expensive to represent using DFT. The approximate energy functionals utilized in recent DFT applications include correlation effects, which are absent in the HF approximation. As a result, DFT approaches may theoretically address the entire periodic table with equal ease and precision.

Although the Hohenberg-Kohn theorem demonstrated that *ab initio* calculations could be performed directly using the density, it was the later work of Kohn and Sham(KS) that provided a practical method for performing DFT calculations. The unknown Hohenberg-Kohn functional, $E[\rho]$, is partitioned as in Eqn (2) in the KS technique. In this partitioning system, $U[\rho(r)]$ is just the classical electrostatic energy, the total of the electron-nucleus attractions and repulsions

$$U[\rho(r)] = \sum_A \int \frac{\{-Z_A \rho(r)\}}{|r - (R_A)|} dr \quad \text{Eqn (5)}$$

The next term, $T[\rho(r)]$, is defined as the kinetic energy of a system of noninteracting electrons with the same density, $\rho(r)$, as the real system of interacting electrons under investigation. This may appear to be a serious mistake. This is not the case since the last term, $E_{XC}[\rho(r)]$, is designed to include the difference between $T[\rho(r)]$ and the actual electronic kinetic energy of the system, in addition to the exchange and correlation (XC) contributions to the energy. According to Kohn and Sham, the sum of the square moduli of single occupied, orthonormal Kohn-Sham molecular orbitals $\rho(r)$ of an N-electron system (with N_α spin-up electrons and N_β spin-down electrons) is $\rho(r)$ which is given by

$$\rho(r) = \rho^\alpha(r) + \rho^\beta(r) = \sum_i^{N_\alpha} |\psi_i^\alpha(r)|^2 + \sum_i^{N_\beta} |\psi_i^\beta(r)|^2 \quad \text{Eqn (6)}$$

Now, $T[\rho(r)]$ can be defined as

$$T[\rho(r)] = \sum_{\rho=\alpha,\beta} \sum_i^{N_\rho} \int \psi_i^\rho(r) \frac{(-\nabla^2)}{2} \psi_i^\rho(r) dr \quad \text{Eqn (7)}$$

It's worth noting that $T[\rho(r)]$ isn't a real density functional because the KS orbitals are needed. Alternative variants of $T[\rho(r)]$ have been developed that rely just

on the electronic density and do not need KS orbitals. They are, however, far too inaccurate to be useful in chemistry. Finally, because the true ground state density, $\rho(r)$, minimizes the energy functional, the energy $E[\rho(r)]$ must be stable with regard to any arbitrary fluctuation in either of the spin densities, i.e.,

$$\frac{(\delta E[\rho(r)])}{\{\delta\rho^\alpha(r)\}} = \frac{(\delta E[\rho(r)])}{\{\delta\rho^\beta(r)\}} \quad \text{Eqn (8)}$$

This condition yields the one-electron KS equations,

$$\left\{ \frac{(-\nabla^2)}{2} - \left(\sum_A \frac{(Z_A)}{|r-(R_A)|} \right) + \int \frac{\rho'(r')}{|r-r'|} dr' + \frac{(\delta E_{xc}[\rho(r)])}{(\delta\rho^\sigma(r))} \right\} \psi_i^\sigma(r) = \epsilon_i \psi_i^\sigma(r) \quad \text{Eqn (9)}$$

As a result, a method for carrying out effective DFT computations emerges. The KS equations are generated and solved using an initial guess at the total spin densities, $\rho^\alpha(r)$ and $\rho^\beta(r)$, and the resulting set of KS orbitals, $\psi_i(r)$, is then used to produce new guesses at $\rho^\alpha(r)$ and $\rho^\beta(r)$. This method is continued until self-consistency is established, which means that the same densities and KS orbitals are recreated each time.

2.1.3 Basis set effects

A basis set is a mathematical representation of a system's orbitals that is utilized in theoretical calculations. By placing fewer limitations on the position of the electrons in space, larger basis sets approach the orbitals more closely. Electrons have a finite probability of being anywhere in space in a true quantum mechanical model. This limit relates to a limitless basis set expansion.

2.1.4 Slater and Gaussian type orbitals

There are two types of basis functions (also called Atomic Orbitals, AO, although in general, they are not solutions to an atomic Schrödinger equation) commonly used in electronic structure calculations: Slater Type Orbitals (STO) and Gaussian Type Orbitals (GTO)(Dunning Jr & Hay, 1976).

2.1.5 Pople style basis sets

6-311G: The core orbitals are a contraction of six PGTOs, and the valence is split into 3 functions, represented by three, one, and one PGTOs, respectively (Krishnan *et al.*, 1980). Each of the basis sets can have diffuse and/or polarization functions added to it (M. J. Frisch *et al.*, 1984). Diffuse functions, which are usually s- and p-functions, come before the G. They are represented by the letters '+' or '++', with the first '+' denoting one set of diffuse 's-' and 'p-' functions on heavy atoms and the second '+' denotes the addition of a diffuse 's-' function on hydrogen atoms. They make it possible for orbitals to cover a larger range of space. For systems where electrons are relatively far from the nucleus, such as molecules with a lone pair, anions, and other systems with a significant negative charge, systems in their excited states, systems with low ionization potentials, descriptions of absolute acidities, and so on, basis sets with diffusion functions are important. After 'G', there are different designations for heavy and hydrogen atoms, as well as polarization functions. Orbitals can alter size but not shape with split valence basis sets. Polarized basis sets overcome this issue by including orbitals with angular momentum in addition to the ground state for each atom's description. 6-31+G(d) and 6-311+G(d). They have a divided valence basis with a single d-type polarization function on heavy atoms and a single set of diffuse sp-functions on heavy atoms. 6-311++G(d,p) is the largest Pople basis set.

2.2 Geometry Optimization

Changes in the energy and other properties of a molecule are usually caused by structural changes inside the molecule (Kassal & Aspuru-Guzik, 2009). Its Potential Energy Surface (PES) describes how the energy of a molecular system changes when its structure changes. The mathematical relationship that connects molecule structure as well as energy, is known as PES. The local minimum is the lowest point on the PES that relates to a specific limited region. Global minimum, on the other hand, is the lowest energy point anywhere on the PES. The saddle point is defined as a point that is maximal in one direction and minimum in the other. The transition structure between two equilibrium structures is referred to as the saddle point. The minimum describes the molecular system's equilibrium structure, with

distinct minima corresponding to different conformations. After obtaining the energy and gradient in a certain number of cycles, optimization is completely done when it converges.

2.3 Gaussian-Software Overview

Gaussian is a computational chemistry software program developed by John Pople and his Carnegie-Mellon University research group in 1970 (M. J. Frisch *et al.*, 1984). Since then, it has been entirely updated. Gaussian 16 is the most recent version. The term comes from the word Gaussian function or orbital, which was chosen to enhance the computational capacity of existing software that employed the Slater type function or orbital. In statistics, Gaussian functions are commonly employed to characterize normal distributions. In this Quantum computation, it denotes the wave function of the ground state of a harmonic oscillator. The linear combination of such Gaussian functions for a molecular orbital is termed as Gaussian orbital. Physicists, chemists, chemical engineers, biochemists, and others utilize the Gaussian software package for study in established and new fields of molecular physics and chemistry. Starting from the basic rules of quantum mechanics, Gaussian predicts the energies, molecular structures, vibrational frequencies and other molecular properties resulting from these basic quantities. It may be used to investigate molecules and reactions in a variety of conditions, including both stable and short-lived intermediate molecules. Ab-initio methods, Semi-empirical methods, and Molecular mechanics are the three types of computational techniques. Since no electron behaviour is taken into account, molecular mechanics is regarded as the least reliable method for solving complex systems of molecules. Since quantum physics is used to account for some of the electron behaviour, semi-empirical approaches are more precise, but their reach is still constrained as they rely on extensive approximations and empirical parameters. Ab-initio techniques explain the electronic structure of a molecule very precisely using only quantum physics and use no assumptions from classical physics. The disadvantage of employing ab-initio methods is that they are incredibly time-consuming to compute. Hence they are confined to much smaller systems such as single molecules. Ab-initio approaches, on the other hand, provide a great deal of information on the electronic structure of a

molecule without enabling the molecule to be synthesized experimentally. The basic idea underlying ab-initio calculations is to solve Schrodinger's equation using a "basis set," which is a collection of mathematical functions.

The technical capabilities of the Gaussian software are listed below.

- The energy calculation was carried out by different methods such as Molecular mechanics calculations, Semi-empirical calculations, Self-consistent field calculations, Correlation energy calculations using Moller-plesset perturbation theory, and Correlation energy calculations using CI, CID, CISD techniques, and density functional theory.
- Analytic Computation of force constants, Polarizabilities, hyper Polarizabilities and dipole moment derivatives analytically for RHF, DFT, etc.
- Harmonic vibrational analysis and thermochemistry analysis using arbitrary isotopes, temperature and pressure.
- Analysis of normal modes in Internal coordinates.
- Determination of IR and Raman intensities for vibrational transitions.
- To determine Harmonic vibration–rotation coupling constants.
- To calculate Anharmonic vibration and vibration–rotation coupling constants.
- Mulliken population analysis, electrostatic potentials and electrostatic derived charges.
- Static and frequency-dependent Polarizabilities and hyper-Polarizabilities for HF and DFT.
- NMR shielding tensors using the SCF and DFT Methods.
- Calculation of spin-spin coupling constants at DFT and HF level
- Vibrational circular dichroism intensities.
- To calculate nuclear quadrupole constants, rotational constants and quartic centrifugal distortion terms.
- HOMO-LUMO analysis.

2.4 GaussView Software Overview

GaussView is a graphical user interface for preparing input for Gaussian and visualizing the output that Gaussian produces graphically(A. Frisch *et al.*, 2000). It

is not integrated with the computational module of Gaussian. GaussView has three key advantages for Gaussian users. First, GaussView's powerful visualization feature allows users to quickly draw in even very large molecules, rotate, translate, and zoom in-zoom out on them using simple movements and can also read PDB files, which are common molecular file formats. Second, GaussView makes it simple to set up various Gaussian calculations. It simplifies the preparation of complicated input for both regular and advanced methods, such as ONIOM, transition structure optimization, CASSCF calculations, periodic boundary conditions (PBC) calculations, and several others. Finally, GaussView is used to investigate Gaussian calculations using a number of graphical ways. GaussView 6 is the recent version which has been used in this study.

Gaussian results that can be viewed graphically include the following:

- Optimized molecular structures.
- Molecular orbitals.
- Electron density surfaces from any computed density.
- Electrostatic potential surfaces.
- Surfaces may also be viewed as contours.
- Atomic charges and dipole moments.
- Animation of the normal modes corresponding to vibrational frequencies.
- IR, Raman, NMR, UV and other spectra.
- Molecular stereochemistry information.
- Animation of Geometry optimizations, IRC reaction path following and Potential energy surface scans. Two variable scans can also be displayed as 3D plots.

2.5 Molecular Docking study

Molecular docking has become an increasingly important method for both drug design and discovery, broadening the perspective on many related experimental studies. In general molecular docking could be interpreted as computational estimation (their conformations and orientations) of protein and ligand complexes (Gilbert, 2004, Anderson, 2003). In this work, Autodock 4.2.6 software (free software) is used, which is available under the Apache License and is currently

maintained by The Scripps Research Institute(Morris *et al.*, 2009). AutoDock is a simulation software for molecular modelling, which is one of the most cited docking software in the research community. The conceptual method is to find the correct binding poses and to accurately predict the binding affinity between the ligand and the targeted protein (Heo *et al.*, 2014; Shin *et al.*, 2013).

3 THEORETICAL STUDY OF TEMOZOLOMIDE BY DENSITY FUNCTIONAL THEORY

3.1 Introduction:

Temozolomide(TMZ) is an imidazotetrazine alkylating prodrug used to treat glioma blastoma of the second generation. TMZ contains an imidazole ring fused with a 1,2,3-tetrazine ring, a carboxamide group attached with an imidazole ring, and a methyl group in the C4 position of the tetrazine ring. It can enter the cerebrospinal fluid and does not require hepatic metabolism for activation (Friedman *et al.*, 2000a; Newlands *et al.*, 1997b). However, TMZ resistance has been a significant problem in malignant glioma, where the cytoprotective DNA repair protein, O6-alkylguanine-DNA alkyltransferase (AGT), transfers the methyl adducts at O6-guanine to a cysteine acceptor residue (Larkin *et al.*, 2007; Tolcher *et al.*, 2003).

This chapter focused on the detailed study of the electronic and spectroscopic properties of the title molecule, TMZ in the gas phase and the aqueous solution. At first, a conformational PES scan was performed at the DFT/B3LYP/6-311++G(d,p) level of theory. The stable conformational choice of the molecule was optimized, and the properties were derived using the same level of theory. Frequency calculation in the gas phase and TD-DFT in the aqueous phase for UV spectral investigation was performed using the same basis set. HOMO-LUMO analysis was carried out to elucidate information regarding charge transfer within the molecule. Vibrational spectral analysis was performed using the Veda program based on calculated potential energy distribution (PED). Finally, the expected intramolecular interactions through hyperconjugation were inspected using the Natural bonding orbital (NBO) analysis to indicate the originating stabilizations.

3.2 Temozolomide

3.2.1 Potential Energy surface scan analysis

The stationary point on the potential energy surface is determined by geometry optimizations in redundant internal coordinates, subject to the change of

dihedral angle of the minimum energy conformer performed at B3LYP/6-311++G(d,p) level as shown in **Figure 3.1**.

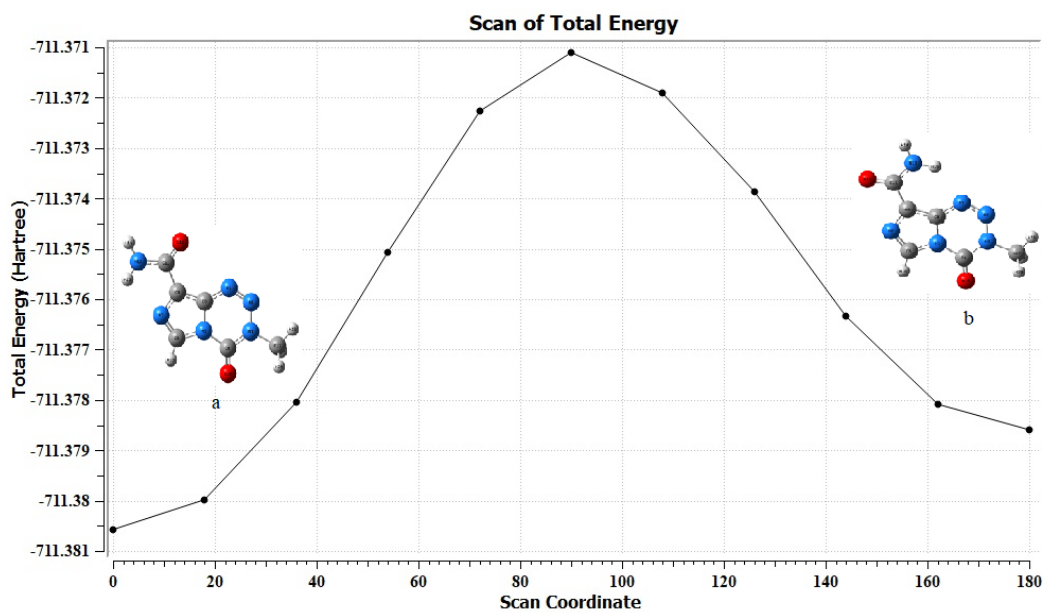


Figure 3.1: Confirmation analysis of TMZ.

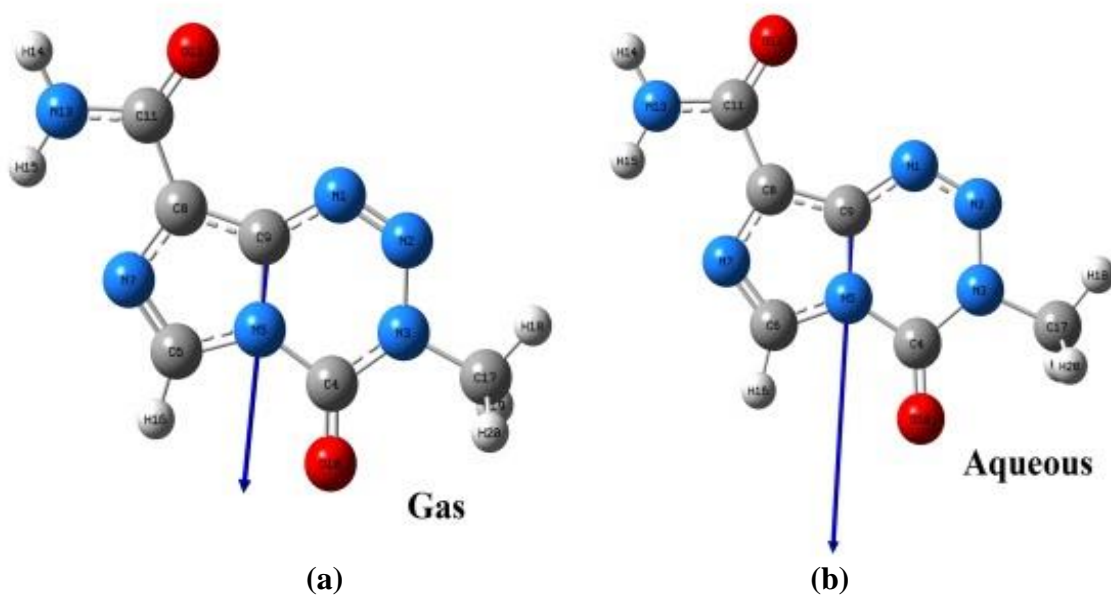


Figure 3.2: Optimized structure of TMZ at B3LYP/6-311++G(d,p) basis set. (a) gas phase (b) aqueous solution

Scanning was started from 0° to 180° by taking 10 intervals with a total of 18 steps. After optimization, the conformer (b) shows high energy at 180° when the carboxamide group rotates to 180° with a minimum energy of -711.38 Hartrees. The intramolecular hydrogen bond to N1 from carboxamide increased the energy by 5.25 kJ mol⁻¹. The conformer (a) with a minimum energy of -711.38 Hartrees is considered the global minima, further re-optimized using the B3LYP/6-311++G(d,p) basis set.

3.2.2 Optimization and properties in both media:

TMZ was optimized at the DFT/B3LYP/6-311++G(d,p) basis set in both the gas and the aqueous solution basis set to assure the stability and responsiveness of the investigated structure, as depicted in **Figure 3.2**. Furthermore, frequency calculations were performed at the same level of theory to ensure that the optimized structure corresponds to true energetic minima. The absence of imaginary frequencies confirms the absolute correspondence of the optimized geometry to its correct energetic minima on the potential energy surface. Calculated results of optimized TMZ in the gas phase and aqueous solvent are given in **Table 3.1**. The difference between the optimized value in the aqueous phase and the corresponding gas phase (-711.26 + 711.24 = 0.02 Hartrees = 53.82 kJ/mol) was used to calculate the relative energy. It can be seen that the calculated total energies (E) in both phases, as well as the corrected ZPVE energy (E_{ZPVE}), were primarily negative. The differences in dipole moments (μ) from 3.50 D in the gas phase to 5.10 D in the aqueous phase imply that an ionic bond is more prominent in the predicted solution with increased polarity.

Table 3.1: Calculated total energies (E), dipole moments (μ), and volumes (V) for compound TMZ in gas and aqueous phase phases by using B3LYP/6-311++G(d,p) basis set.

Medium	E (Hartrees)	E _{ZPVE} (Hartrees)	μ (D)	V(A ³)
Gas phase	-711.38	-711.24	3.50	178.2
Aqueous phase	-711.40	-711.26	5.10	178.3

3.2.3 Geometrical parameters

The optimized geometry of the molecule under investigation is considered to possess C_1 point group symmetry. The CIF of the title structure was downloaded from Cambridge Crystallographic Data Centre (CCDC) with the CCDC number 665062 (Babu et al., 2008). The experimental geometrical parameters were obtained from this CIF file. The calculated geometrical parameters are presented in **Table 3.2**. The bond length between C of methyl and N of tetrazine ring is found to be 1.463 Å. The structure has two C=O bonds, out of which carboxamide C=O bond length is 1.218 Å and tetrazine C=O bond length is 1.207 Å. The C-N bond length of 1.362 Å in carboxamide indicates a partial double bond character caused by amino lone-pair. The angle of $N_2-N_3-C_4=126.65^\circ$ in the tetrazine ring indicates an irregular hexagon structure due to lone pair of electrons in nitrogen atoms. Both the tetrazine and imidazole rings are planar ($N_2-N_1-C_9-N_5=0.0^\circ$; $N_2-N_3-C_4-N_5=0.03^\circ$; $N_5-C_6-N_7-C_8=0.0^\circ$). According to the optimization results, Carboxamide is co-planar to the imidazole and tetrazine ring structure ($O_{12}-C_{11}-N_{13}-H_{14}=0.02^\circ$; $N_7-C_8-C_{11}-O_{12}=0.0^\circ$).

Table 3.2: Selected geometrical parameters of TMZ using B3LYP/6-311++G(d,p) basis set.

Bond lengths(Å)			
Parameters	Gas	Aqueous	Exp
N1-N2	1.26	1.27	1.27
N1-C9	1.37	1.36	1.37
N2-N3	1.40	1.38	1.39
N3-C17	1.46	1.47	1.48
C4-O10	1.21	1.21	1.21
N5-C6	1.37	1.37	1.36
C4-N5	1.40	1.40	1.40
N3-C4	1.38	1.38	1.37
N5-C9	1.40	1.40	1.38
C6-N7	1.31	1.31	1.32
C6-H16	1.08	1.08	0.93
N7-C8	1.37	1.37	1.38
C8-C11	1.49	1.49	1.50

C11-O12	1.22	1.23	1.23
C11-N13	1.36	1.35	1.32
C8-C9	1.39	1.39	1.36
C17-H18	1.09	1.09	0.90
C17-H19	1.09	1.09	0.96
N13-H14	1.01	1.01	0.96
RMSD	0.07	0.06	
Bond angles(°)			
Parameters	Gas	Aqueous	Exp
N2-N1-C9	119.77	119.57	118.47
N1-N2-N3	119.96	120.36	120.45
N2-N3-C4	126.65	126.33	126.41
C4-N3-C17	118.68	118.62	119.56
N3-C4-O10	125.50	125.10	125.53
C4-N5-C9	122.24	122.01	121.94
C6-N5-C9	107.39	107.47	107.18
N5-C6-N7	110.68	110.58	111.66
N5-C6-H16	122.23	122.47	124.14
N7-C8-C9	109.33	109.22	110.72
N7-C8-C11	121.83	121.89	123.51
C8-C11-O12	122.58	122.18	118.49
O12-C11-N13	124.27	123.84	124.32
C11-N13-H14	118.52	119.52	114.65
C11-N13-H15	120.79	120.82	132.66
C6-N7-C8	107.57	107.60	105.25
RMSD	3.45	3.49	
Dihedral angles(ϕ)			
Parameters	Gas	Aqueous	Exp
N2-N1-C9-N5	0.00	0.0	2.71
N1-N2-N3-C4	-0.03	0.0	-1.94
N1-N2-N3-C17	180.0	180.0	176.48
N2-N3-C4-N5	0.03	0.0	0.85
O10-C4-N5-C6	-0.01	0.0	-4.10
C9-N5-C6-H16	180.00	180	179.71
N5-C6-N7-C8	0.00	0.0	0.70
N7-C8-C9-N1	-180.00	180.0	-179.72
N7-C8-C11-O12	180.0	180.0	-175.5
O12-C11-N13-H14	0.03	0.0	1.87
RMSD	112.44	159.94	

3.2.4 Atomic charges and MEP

The atomic and molecular electrostatic potentials (MEP) charges of the optimized structures of TMZ for the gas and aqueous phase are summarized in **Table 3.3**. The high negative value for NPA atomic charges on N13 demonstrates intramolecular hydrogen bonding with the amine group in both phases, affecting the molecule's stability. The O12 atoms of C=O in carboxamide have a higher negative value than the O10 atoms of the tetrazine ring in both phases. Among the carbon atoms, C9 shows different charges in both phases; NPA charges at C9 show positive while Mulliken charges show negative values. The graph shows the relative trends for Mulliken and Natural Population Analysis (NPA) atomic charges of TMZ in the gas and aqueous phase (**Figure 3.3**).

Table 3.3: Mulliken, Natural Population Analysis (NPA) charges (in a.u.) and Molecular Electrostatic Potentials (MEP) of TMZ in the gas phase and aqueous solution calculated at B3LYP/6-311++G(d,p) level of theory.

Atoms	Gas Phase			Aqueous Phase		
	Mulliken	NPA	MEP	Mulliken	NPA	MEP
N1	-0.45	-0.17	-18.33	-0.48	-0.21	-18.34
N2	0.48	0.01	-18.29	0.40	0.01	-18.29
N3	-0.12	-0.31	-18.28	-0.07	-0.29	-18.26
N5	-0.21	-0.45	-18.28	-0.17	-0.44	-18.27
N7	-0.11	-0.47	-18.37	-0.15	-0.48	-18.37
N13	-0.41	-0.80	-18.37	-0.43	-0.77	-18.36
O10	-0.27	-0.58	-22.35	-0.32	-0.60	-22.35
O12	-0.35	-0.60	-22.40	-0.46	-0.68	-22.44
C4	0.26	0.82	-14.59	0.31	0.84	-14.57
C6	0.36	0.25	-14.67	0.36	0.27	-14.66
C8	0.32	0.06	-14.71	0.36	0.05	-14.71
C9	-0.76	0.28	-14.67	-0.74	0.30	-14.67
C11	0.06	0.63	-14.66	0.10	0.64	-14.67
C17	-0.25	-0.35	-14.71	-0.26	-0.36	-14.70

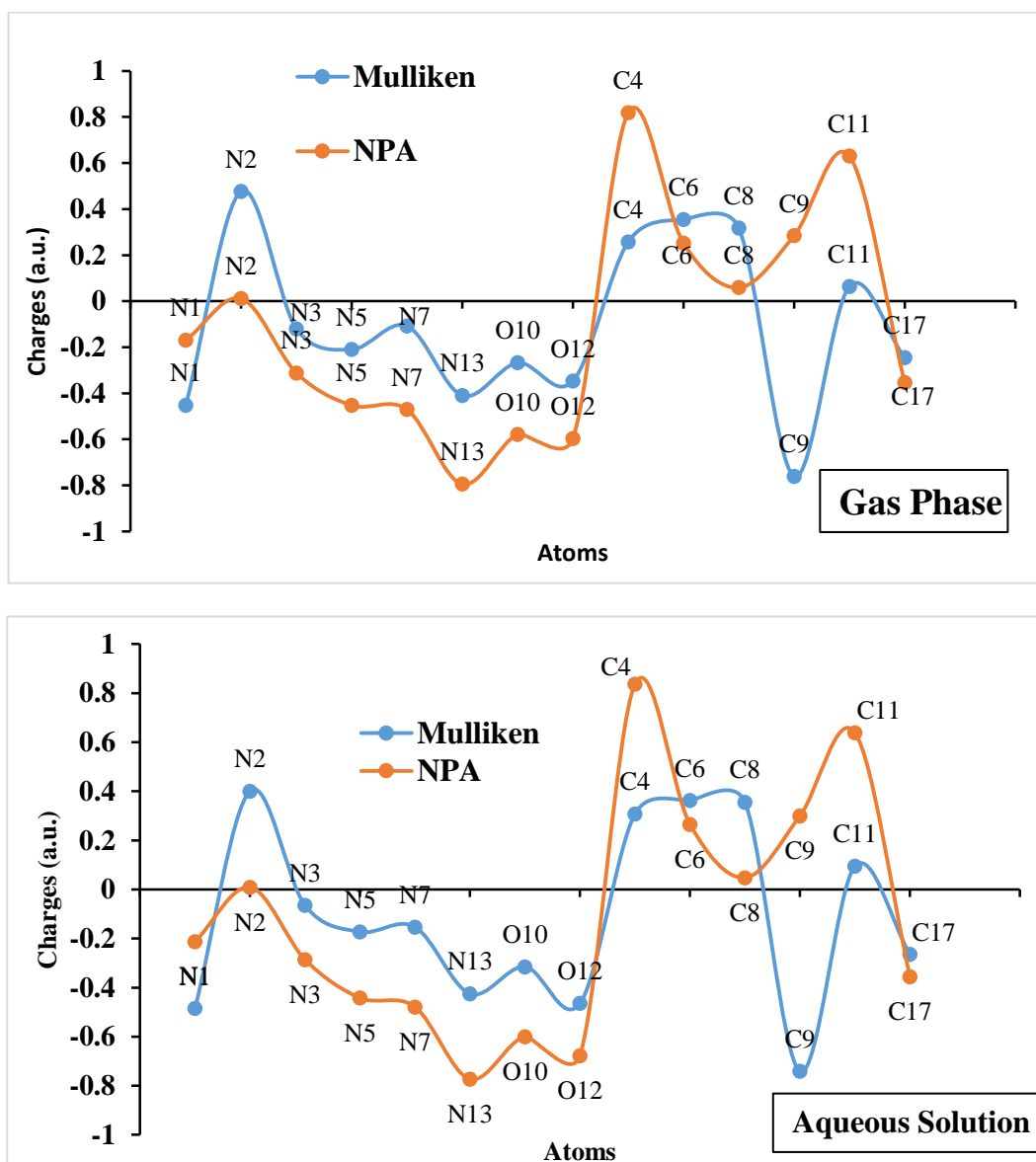


Figure 3.3: Graph showing the trends for Mulliken and Natural Population Analysis (NPA) Atomic charges of TMZ in the gas phase (upper) and the aqueous phase (bottom).

The molecular electrostatic potentials (MEP) charges are also presented in **Table 3.3**. The same trends of values are observed in both media, and the relative expected tendency is observed as MEP O atoms > MEP N atoms. MEP on O12 is greater than O10, while MEP on N7 presents higher negative values in both media than the other Nitrogen atoms. Since the MEP surface mapping helps in analyzing reaction sites with potential electrophiles and nucleophiles, the calculated

electrostatic potential surfaces on the molecular surface of TMZ in the gas phase are displayed in **Figure 3.4**. The red colour indicates the nucleophilic region (higher electron density) on the molecule's surface, while the electrophilic region is indicated by the blue colour (lower electron density). The intense red color is located on the atom O12, which has higher negative MEP values. On the other hand, the blue color region is observed on C4, C6, C17, and N13 atoms, revealing the electrophilic sites. The analysis of MEP atomic charges with two adjacent N atoms, C4 is the most electrophilic site of the molecule.

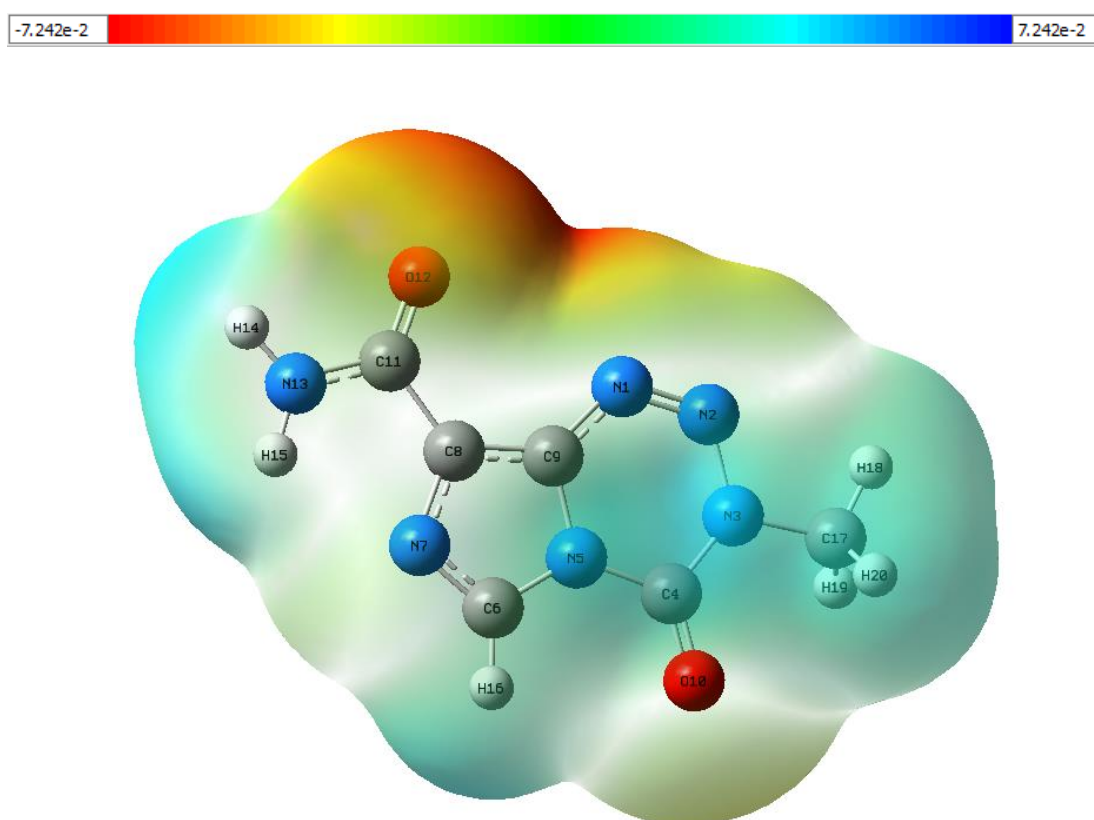


Figure 3.4: Calculated electrostatic potential surfaces on the molecular surface of TMZ (0.0027 a.u.) in the gas phase using 6-311++G(d,p) basis set.

3.2.5 ^1H and ^{13}C NMR analysis

The ^1H and ^{13}C NMR calculations were performed by GIAO (Gauge-Independent Atomic Orbital) method at the B3LYP/6-311++G(d,p) basis set. **Table 3.4** display the predicted chemical shifts in comparison with the experimental data

from ref (Łaszczyk *et al.*, 2013). The ^1H NMR analysis shows that the proton present in the imidazole ring H16 with 8.34 ppm shows the highest deshielding value. H15 with 7.29 ppm for NH_2 shows a greater deshielding chemical shift than H14 (5.14 ppm) due to the hydrogen bonding with N7. C11 shows a chemical shift of 164.96 ppm due to two adjacent electronegative atoms, oxygen and nitrogen. The theoretical and experimental chemical shifts show comparable values to each other.

Table 3.4: Experimental and theoretical chemical shifts of TMZ calculated in GIAO method using DMSO as solvents.

^1H NMR			^{13}C NMR		
Atom	Calculated (ppm)	Experimental (ppm)	Atom	Calculated (ppm)	Experimental (ppm)
H16	8.34	8.81	C11	164.96	161.51
H15	7.29	7.79	C4	143.48	139.18
H14	5.14	7.69	C9	140.51	134.58
H18	4.28	3.87	C8	137.54	130.50
H19	3.86	3.87	C6	132.07	128.36
H20	3.86	3.87	C17	38.67	36.13
RMSD	1.091		RMSD	4.749	

3.2.6 UV-vis analysis

The Wavelengths(λ) and the excitation energies(E) are both expressed in nm, and oscillator strength(f) of TMZ evaluated by the TD-DFT method are shown in **Table 3.5**, and **Figure 3.5**, displays the plot of the ultraviolet spectra. A strong theoretical absorption peak is found at 315.30 nm with an oscillator strength of 0.3312 and excitation energy of 3.9323 eV. This peak is the major contribution of the excitation from HOMO to LUMO with 94% contribution. The peak observed at 295.49 nm with oscillator strength of 0.0039, and excitation energy of 4.1958 eV has the major contribution of 89% from HOMO-3 to LUMO transition, and the peak observed at 319.62 nm with small oscillator strength of 0.0010 and excitation energy of 3.8791 eV have the major contribution from HOMO-1 to LUMO (89%).

Table 3.5: Electronics properties of TMZ calculated using TD-DFT (B3LYP)/6-311++G(d,p)

Wavelength λ (nm)	Energy eV	Oscillator strength f	Symmetry	Major contributions
319.62	3.8791	0.0010	Singlet-A	H-1→L (89%); H-3→L (9%)
315.30	3.9323	0.3312	Singlet-A	H→L (94%); H→L+1 (4%)
295.49	4.1958	0.0039	Singlet-A	H-3→L (89%); H-1→L (9%)

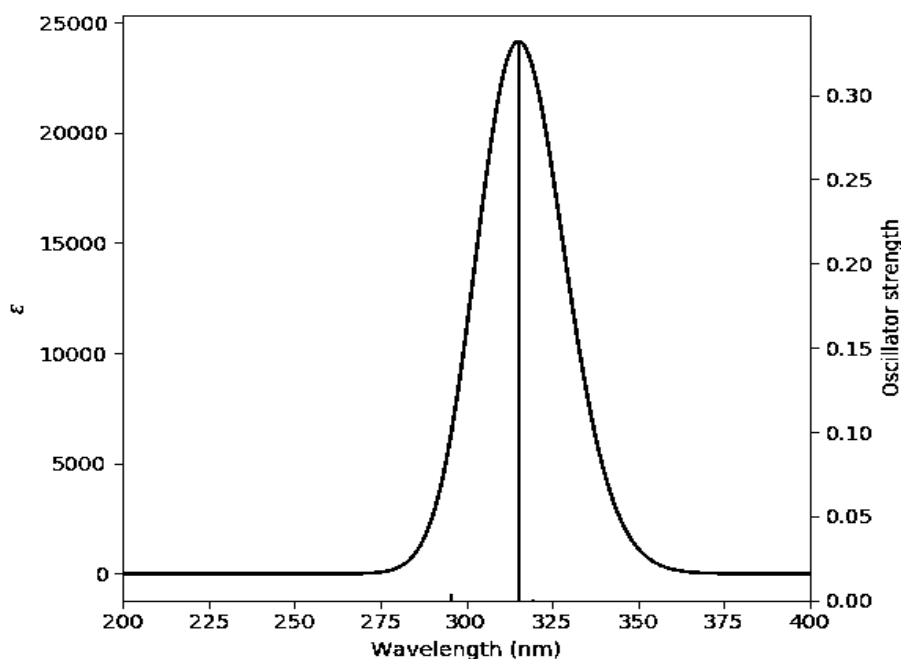


Figure 3.5: UV spectra of TMZ calculated at B3LYP/6-311++G(d,p) basis set

3.2.7 Natural Bond Orbital Analysis:

The natural bond orbital analysis is a useful technique for understanding intramolecular and intermolecular bondings and their interactions with charge transfer between bonds. It also serves as a convenient foundation for studying charge transfer or conjugative interaction in a molecular system (Cortes *et al.*, 2019; Reed *et al.*, 1988). The approximation of the second-order perturbation theory for important energetics arising out of all possible interactions between filled donor and empty acceptor NBOs is envisaged. The donor (i) and acceptor (j) NBO, the stabilization

energy $E(2)$ linked with electron delocalization between donor and acceptor is given below in the equation;

$$E_{ij}^2 = -q_i \frac{(F_{ij})^2}{E_j - E_i}$$

Where q_i is the orbital occupancy, E_j and E_i are orbital energies, and F_{ij} is the off-diagonal NBO Fock matrix element. When the values $E(2)$ is higher, the interaction of electron donors and electron acceptors becomes more intensive, i.e., a more donating tendency from electron donors to acceptors is observed with a maximum amount of conjugation on the complete molecular system. The stabilizing donor-acceptor interaction rises due to delocalization of electron density between lone pair or bonding (occupied Lewis-type) and Rydberg or antibonding (unoccupied non-Lewis type) NBO orbitals.

NBO analyses performed on TMZ are presented in **Table 3.6**. The lone pair of electrons present in the nitrogen atoms, N1, N2 and N7 delocalized to N2-N3, N5-C9, N1-C9, N3-C4, N5-C6, C8-C9 σ^* antibonding orbitals, and lone pair of oxygen atoms O10 and O12 to N3-C4, C4-N5, C8-C11, C11-N13 σ^* antibonding orbitals. The lone pair of electrons from N3, N5 and N13 is delocalized to N1-N2, C4-O10, C6-N7, C8-C9, and C11-O12 π^* antibonding orbitals. The delocalization energy for lone pair of electrons to π^* antibonding orbitals is higher than the delocalization energy for lone pair of electrons to σ^* antibonding orbitals. The delocalization of π bonding orbitals from N1-N2, C6-C7 and C8-C9 to π^* antibonding orbitals of C8-C9, N1-N2, C6-C7 and C11-O12 shows the intramolecular hyper-conjugative interaction in the molecule. The π^* antibonding orbitals of N1-N2, C6-C7 and C8-C9 of the NBO conjugated with C8-C9, C8-C9 and C11-O12 π^* antibonding orbitals, resulting in the stabilization energy of 46.37, 78.83 and 90.6 respectively. Overall, the NBO analysis showed that charge transfer is mainly due to the lone pairs of electrons of N and O atoms, which leads to intramolecular charge transfer (ICT) in order to stabilize the system.

Table 3.6. Second-order perturbation theory analysis of Fock matrix in NBO of TMZ.

Donor (i)	Acceptor (j)	E2 kcal/mol	E(j)-E(i) a.u.	F(i,j) a.u.
π (N1-N2)	π^* (C8-C9)	14.19	0.40	0.072
π (C6-N7)	π^* (C8-C9)	21.33	0.34	0.080
π (C8-C9)	π^* (N1-N2)	23.60	0.24	0.067
	π^* (C6-N7)	17.98	0.27	0.063
	π^* (C11-O12)	14.81	0.32	0.062
LP(N1)	σ^* (N2-N3)	17.55	0.67	0.098
	σ^* (N5-C9)	11.64	0.77	0.086
LP(N2)	σ^* (N1-C9)	9.77	0.90	0.084
	σ^* (N3-C4)	9.34	0.85	0.080
LP(N7)	σ^* (N5-C6)	6.96	0.81	0.068
	σ^* (C8-C9)	5.48	0.94	0.065
LP(2)(O10)	σ^* (N3-C4)	26.47	0.67	0.121
	σ^* (C4-N5)	28.52	0.64	0.123
LP(2)(O12)	σ^* (C8-C11)	20.25	0.65	0.104
	σ^* (C11-N13)	25.12	0.70	0.121
LP(1)(N3)	π^* (N1-N2)	38.89	0.25	0.090
	π^* (C4-O10)	58.54	0.28	0.115
LP(5)(N5)	π^* (C4-O10)	46.80	0.28	0.106
	π^* (C6-N7)	41.53	0.29	0.100
	π^* (C8-C9)	29.78	0.31	0.087
LP(1)(N13)	π^* (C11-O12)	60.81	0.28	0.119
π^* (N1-N2)	π^* (C8-C9)	46.37	0.05	0.076
π^* (C6-N7)	π^* (C8-C9)	78.83	0.02	0.062
π^* (C8-C9)	π^* (C11-O12)	90.60	0.03	0.077

Note: where E(2) = Energy of hyper conjunctive interactions; E(j)-E(i) = Energy difference between the donor (i) and acceptor (j) NBO orbitals and F(i,j) = Fock matrix element between i and j NBO orbital.

3.2.8 Frontier Molecular Orbital Analysis

HOMO, the outer occupied orbital can donate electrons, and the LUMO, the unoccupied orbital can accept electrons. HOMO-LUMO and HOMO-LUMO energy gap establish the ionization potentials, electron affinity, and stability of the molecule, respectively. The computation results indicate that the molecule has 350 molecular

orbitals, where 50 are occupied, and the remaining are unoccupied molecular orbitals. Molecular orbitals 51 and 50 were identified as LUMO and HOMO molecular orbitals, respectively. The HOMO and LUMO orbitals with energy values are shown in **Table 3.7**. LUMO is localized by π^* bonding type orbitals on carboxamide, imidazole, and tetrazine ring (**Figure 3.6**). HOMO is localized by π bonding type orbitals on imidazole, tetrazine ring, methyl group, nitrogen, and the oxygen atom of the carboxamide group. The LUMO and HOMO energies obtained are at -2.822 eV and -7.270 eV for the gas phase and -2.820 eV and -7.166 eV for the aqueous solution, respectively. The HOMO-LUMO energy gap (ΔE) in gas phase is 4.448 eV, and for the aqueous solution, it is 4.346 eV. Comparing the energy gap of TMZ in both media, a slight decrease in the energy gap is observed in the aqueous solution. This energy gap confirms the stability and prospective bioactivity of TMZ(Murugavel *et al.*, 2019).

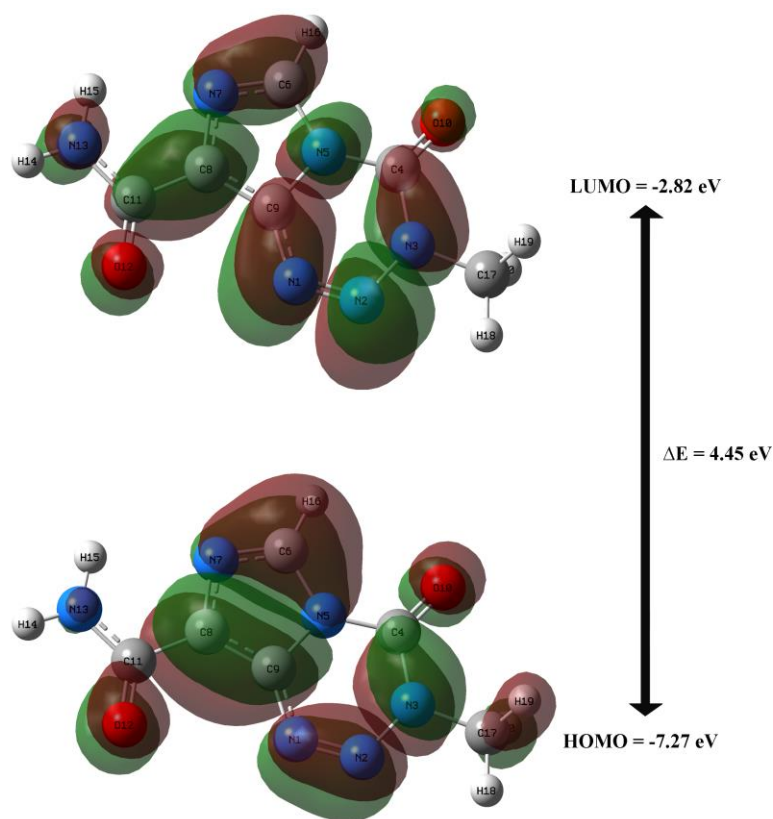


Figure 3.6: HOMO-LUMO diagram of TMZ

Table 3.7. Frontier Molecular Orbitals energy parameters and global reactivity descriptors of TMZ

FMOs	Gas	Aqueous
HOMO energy	-7.27	-7.17
LUMO energy	-2.82	-2.82
Energy gap (ΔE)	4.45	4.35
Ionization potential (I)	7.27	7.17
Electron affinity (A)	2.82	2.82
Hardness (η)	2.22	2.17
Chemical potential (μ)	-5.05	-4.99
Electronegativity (χ)	5.05	4.99
Electrophilicity (ω)	5.72	5.74

Other quantum chemical calculation which further account for global reactivity of molecules was invoked by considering the Koopmans approach (Glendening & Weinhold, 1998; Koopman, 1934). According to the approximation, the ionization potential and the electron affinity are approximately equal to the negative of the HOMO and LUMO energies respectively. The Ionization potential ($I = -E_{\text{Homo}}$), Electron affinity ($A = -E_{\text{Lumo}}$), Hardness ($\eta = (I - A) / 2$), Chemical potential ($\mu = -\chi$ (Electronegativity) = $-(I + A) / 2$) and Electrophilicity ($\omega = \mu^2 / 2\eta$) are calculated according to Koopmans' theorem (Vennila *et al.*, 2016). The tabulated FMO energy parameters and global reactivity descriptors of TMZ in both media are shown in **Table 3.7**. More so, the electron affinity and electronegativity values of TMZ shows a moderate acceptor properties as well as a high ability to pull electron density to itself. This could be attributed to the good number of N-atoms in the molecular structure with lone pairs of electrons donated for reactions. The high ionization potential of the molecule in both media indicates high reactivity of atoms and the molecule.

3.2.9 Vibrational Assignment

The TMZ molecule with 20 atoms produces 54 normal modes of vibrations from the $3N-6$ relation, consisting of 19 stretching, 18 bending, and 17 torsional

vibration modes as tabulated in **Table 3.8**. There are 12 modes related to C-H bonds out of 54 normal modes. The 54 normal vibrational modes are assigned based on the detailed movement of individual atoms. The computed wavenumbers obtained are usually higher than the observed wavenumbers due to the combination of electron similarity effects and DFT basis set deficiencies. As a result, scaling factors are used to fit the experimental values, with a scaling factor of 0.958 for values greater than 1800 cm^{-1} and a scaling factor of 0.983 for values less than 1800 cm^{-1} (Rauhut & Pulay, 1995). The calculated and experimental reference (Łaszczyńska *et al.*, 2013) of IR spectra are shown in **Figure 3.7**.

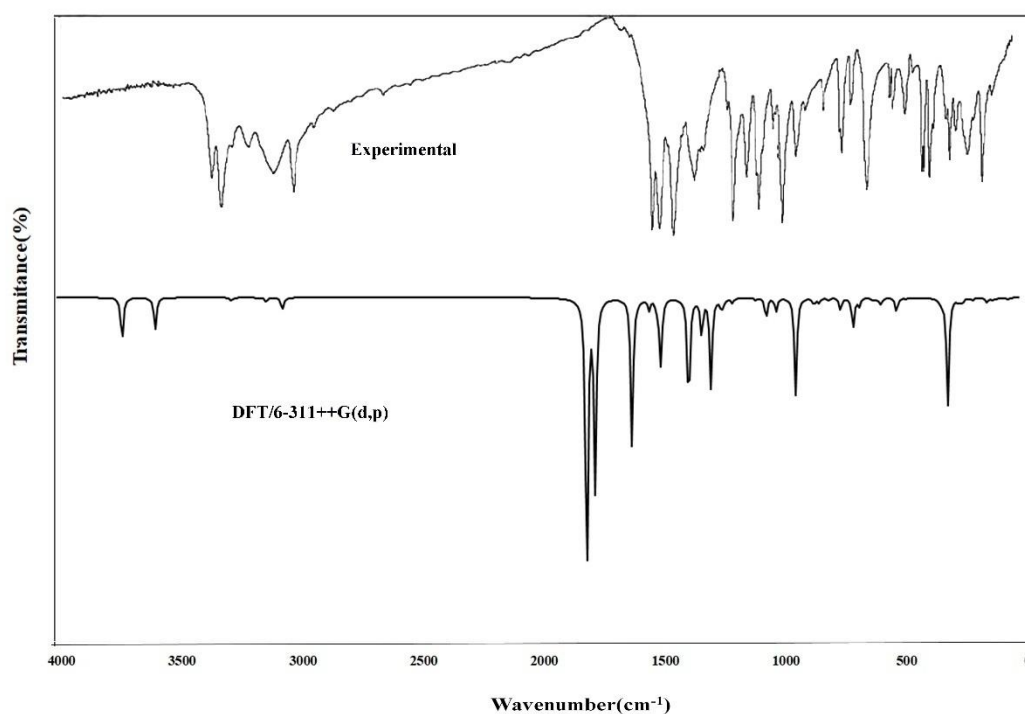


Figure 3.7: Comparative analysis between experimental and DFT FT-IR spectra of TMZ.

Assignments:

4000-3000 cm^{-1} regions:

Stretching vibration of N-H of amine is usually observed in the region 3500-3220 cm^{-1} . The asymmetric and symmetric stretching of the amine group present in carboxamide is found at 3566.47 cm^{-1} and 3434.64 cm^{-1} , respectively, which is close

to the corresponding experimental stretching vibrations of 3421 cm^{-1} and 3388 cm^{-1} . The C-H stretching vibration usually show IR band in the region $3100\text{-}3000\text{ cm}^{-1}$. The experimental C-H stretching vibration of imidazole is found at 3037 cm^{-1} , and calculated wavenumbers is found at 3132.10 cm^{-1} with a PED of 99%.

3000-1000 cm^{-1} regions:

TMZ sole methyl group C-H stretching vibrations occur in the region $3000\text{-}2840\text{ cm}^{-1}$. Our analysis found calculated C-H asymmetric stretching modes of the methyl group at 3035.66 and 2993.07 cm^{-1} and the symmetric stretching at 2929.62 cm^{-1} . Deformed methyl group vibrations are generally found in between 1450 and 1400 cm^{-1} , conforming to the asymmetric deformation bending at 1455.77 cm^{-1} and symmetric bending at 1455.77 cm^{-1} of the computed TMZ methyl group. There are two carbonyl groups present in the molecule, and one is on the carboxamide group and the other on the tetrazine ring. The calculated stretching frequency for C=O on carboxamide is found at 1764.08 cm^{-1} , while another C=O stretching vibration is found at 1729.76 cm^{-1} corresponding to the experimental wavenumbers 1758 cm^{-1} and 1732 cm^{-1} , respectively. The N1-N2 stretching vibration was calculated at 1510.47 cm^{-1} , and the experimental was found at 1577 cm^{-1} . In-plane and out of plane bending vibrations of C-H in the carboxamide group are found at 1463.62 and 816.32 cm^{-1} , respectively.

1000-0 cm^{-1} regions:

The twisting of methyl group vibration is calculated at 95.32 cm^{-1} . The presence of an adjacent amine group increases the stretching of C=O of carboxamide. In the present study, the bands ascribed at 837.11 , 687.53 , 677.81 , 594.52 , 564.63 , 501.12 , 460.35 cm^{-1} , and 684.65 , 531.99 , 294.51 cm^{-1} have been assigned to the ring for in-plane and out of plane bending modes, respectively.

Table 3.8: Vibrational assignments of TMZ fundamental modes along with calculated IR and PED using the B3LYP method.

Mode	Exp.	Calculated (cm ⁻¹)	Scaled (cm ⁻¹)	Intensity (kM/mol)	Characterization of normal modes with PED (%)
54	3421	3722.86	3566.47	84.90	ν_a NH2 (99)
53	3388	3585.25	3434.64	60.28	ν_s NH2 (99)
52	3037	3269.43	3132.10	6.40	ν C6-H16 (99)
51		3168.78	3035.66	0.25	ν_a CH3 (82)
50		3124.32	2993.07	8.38	ν_a CH3 (100)
49		3058.08	2929.62	23.31	ν_s CH3 (82)
48	1758	1794.60	1764.08	558.95	ν O10-C4 (86)
47	1732	1759.68	1729.76	346.16	ν O12-C11 (80)
46		1607.22	1579.88	275.40	β NH2 (57)
45		1580.65	1553.77	4.77	ν C9-C8 (44) β NH2 (57)
44	1577	1536.60	1510.47	20.43	ν N2-N1 (58)
43		1506.12	1480.50	15.38	δ_a CH3 (69)
42		1488.94	1463.62	121.94	β C6-H16 (28)
41	1452	1480.96	1455.77	12.25	δ_a CH3 (72)
40		1447.45	1422.84	0.35	δ_s CH3 (72)
39	1402	1409.62	1385.65	2.10	ν N5-C6 (38)
38		1372.08	1348.74	217.25	ν N1-C9 (24) ν N13-11 (11) ν C11-C8 (11)
37		1339.10	1316.32	1.77	ν N5-C6 (19) β N5C6N7 (16) β C8N7C6 (15)
36		1317.71	1295.30	70.07	ν N3-C4 (26) ν N3-C17 (24) β C4N3N2 (10)
35		1279.57	1257.80	164.62	ν N7-C8 (32) β N5C6N7 (14)

34		1235.82	1214.80	21.35	γ CH3 (11)
33		1226.78	1205.91	6.80	β C6- H16 (26)
32		1191.14	1170.88	9.78	β C6-H16 (20)
31		1149.50	1129.95	0.21	γ CH3 (30)
30		1093.67	1075.08	3.68	β NH2 (57)
29		1050.77	1032.90	38.69	ψ N3-C4 (11) ψ N3-C17 (14) β C8N7C6 (21)
28		1009.52	992.35	24.65	ψ N13-C11 (10) ψ N3-C4 (19) β N2-N1-C9 (16)
27		927.95	912.17	179.52	ψ N3-N2 (28) β O10C4N3 (13) β N3N2N1 (11)
26		851.59	837.11	12.15	β R (21)
25		830.97	816.82	8.04	τ H16-C6 (83)
24		792.38	778.90	4.36	τ C9C8N7C6(11) γ O12N13C8C11(59) γ C11C9N7C8 (19)
23		742.40	729.78	22.01	γ O10-C4 (84)
22		699.42	687.53	0.73	β R (15)
21		696.50	684.65	1.28	τ R (20)
20		689.52	677.81	55.75	β R (20)
19		664.60	653.29	15.34	γ H16C6N7C8 (11) γ C8N7C6N5 (51)
18		604.81	594.52	5.50	β R (15)
17		588.99	579.01	3.79	τ H14N13C11C8 (71)
16		574.39	564.63	11.02	β R (25)
15		541.19	531.99	0.11	τ R (36)
14		509.79	501.12	26.05	β R (31)
13		468.31	460.35	2.03	β R (17)
12		330.47	324.85	6.30	β N13-C11-C8 (36)
11		319.34	313.91	6.89	β O10C4 (34) - β C17N3 (27)
10		299.59	294.51	0.95	β N1C9C8 (14) β N13C11C8 (11) β C17N3N2 (36) τ R(18)

9		296.89	291.84	200.56	τ H14N13C11C8 (81)
8		251.66	247.37	7.96	τ C17C4N2N3 (39)
7		235.98	231.98	9.36	β R (48)
6		194.02	190.66	4.69	τ C17C4N2N3 (34)
5		135.42	133.12	8.29	β N1C9C8 (14) β N13C11C8 (12) β C11C8N7 (61)
4		111.25	109.37	4.78	τ N5C4N3N2 (28)
3		96.71	95.32	1.30	τ w CH3 (33)
2		67.59	66.44	0.08	τ N2N1C9N5 (43) γ C11C8 (21)
1		45.81	45.01	3.39	τ N13C11C8C9 (83)

Symbol for stretching here: stretching (a = antisymmetric; s = symmetric); β = deformation in the plane; γ = deformation out of the plane; τ = torsion; β R = deformation ring; τ R= torsion ring; τ w= twisting; δ = deformation; and R = Ring

3.3 Conclusion

The TMZ Potential Energy Surface revealed that the resultant calculated structure is more stable when the NH₂ group is opposite the tetrazine ring. The relative energy between the optimized structure in the aqueous and gas phase is found at 53.85 kJ/mol, which is appreciably important for TMZ stability. The complete vibrational studies of the titled molecule agree well with the experimental vibrational frequencies. The theoretical and experimental chemical shifts show comparable values to each other. The UV spectrum in the aqueous phase calculated with Time-dependent DFT revealed a significant peak at 315.30 nm, which corresponds to the n→π* transition. The intramolecular hydrogen bonding is confirmed by the behaviour of the three charges discussed for both media. NBO analysis showed the intramolecular charge transfer within the molecule was primarily from the lone pairs of the electron in N-atom and O-atom. Furthermore, global reactivity descriptors of TMZ in both media were determined using FMO and HOMO-LUMO analysis, indicating the molecule's bioactivity and stability.

CHAPTER 4: RESULTS AND DISCUSSION

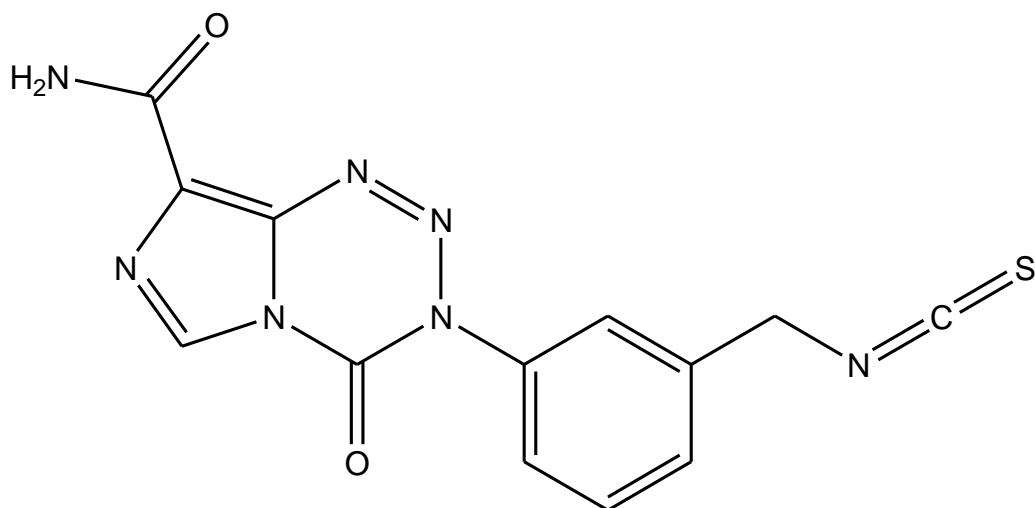
4 ELECTRONIC AND SPECTROSCOPIC DFT STUDY OF TEMOZOLOMIDE WITH BENZYL ISOTHIOCYANATE (BITC)

4.1 Introduction:

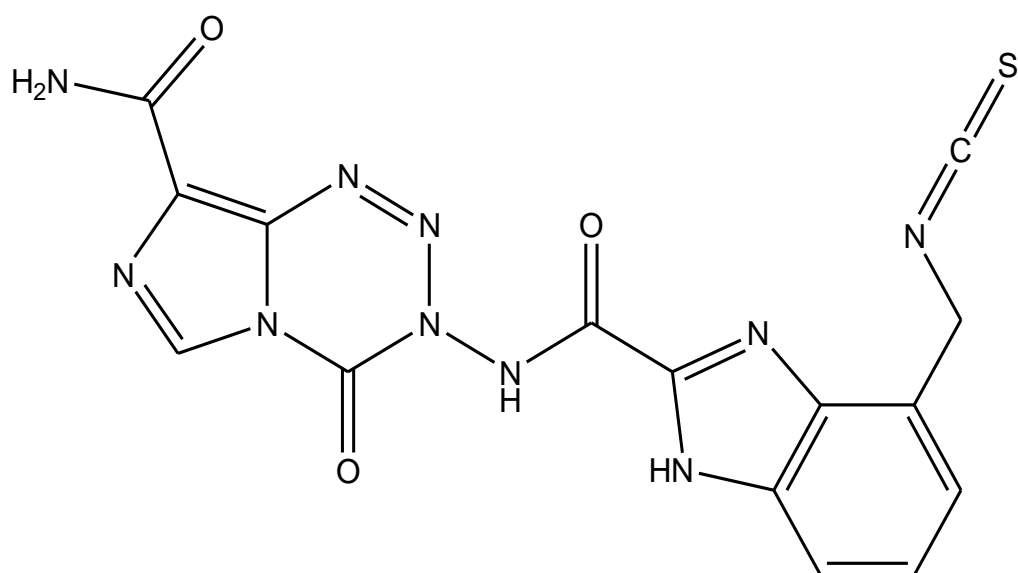
O6-alkylguanine-DNA alkyl transferase (AGT or MGMT for methyl) is considered to be mutagenic and cytotoxic, which transfer the methyl groups to internal cysteine residue in irreversible manner, thus suppressing repair activity or necessitating de novo synthesis to restore repair activity. Therefore, researchers suggest that to stop the repair activity of MGMT, the methyl group can be replaced by bulky alkyl group. In this study, the methyl group is replaced by benzyl isothiocyanate (BITC) derivatives (Moody & Wheelhouse, 2014).

Isothiocyanates compounds exhibit antitumor activity. Isothiocyanates are abundant in cruciferous vegetables such as broccoli, watercress, Brussels sprouts, cabbage, Japanese radish and cauliflower, which significantly contribute chemopreventive activity. Some isothiocyanates derived from cruciferous vegetables, such as sulforaphane (SFN), phenethyl isothiocyanate (PEITC), and benzyl isothiocyanate (BITC), are highly effective in preventing or reducing the risk of cancer induced by carcinogens in animal models. They also inhibit the growth of various types of cancer cells (J. W. Lee & Cho, 2008; Trachootham *et al.*, 2008).

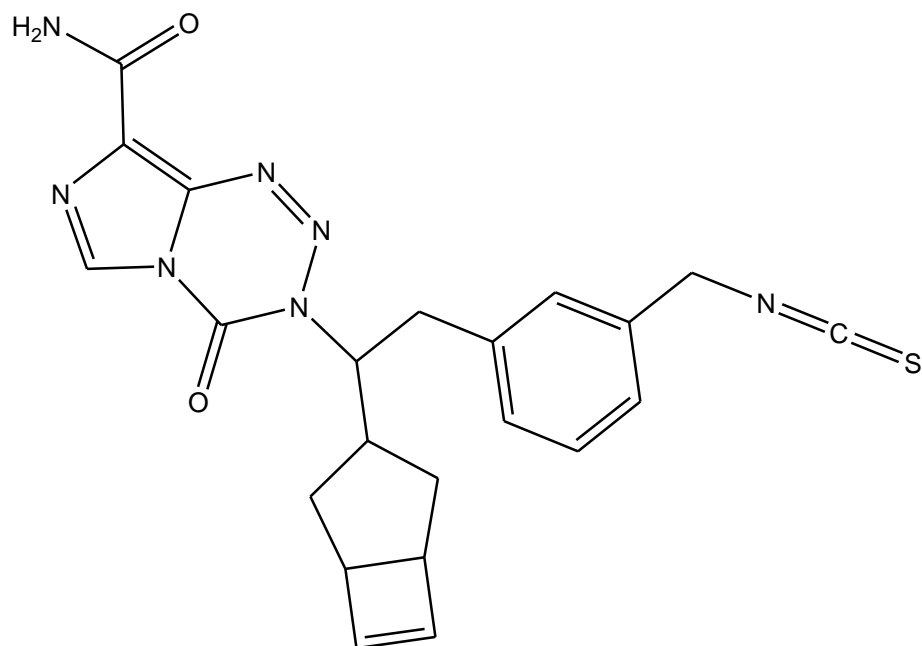
The cruciferous vegetable isothiocyanate derivatives and BITC are able to inhibit the growth of A549 cells by inducing apoptosis at low concentrations and necrosis at high concentrations (Kuang & Chen, 2004). The ability of isothiocyanate to inhibit tumorigenesis depended on the structure of the isothiocyanates, the animal species, target tissues, and the specific carcinogen employed. They target multiple pathways including apoptosis, the MAPK pathway, oxidative stress, and the cell cycle machinery. Apoptosis induced by various isothiocyanates has been extensively studied in cancer cell lines derived from various tissues (Wu *et al.*, 2009). In this study, four potential BITC derivatives with TMZ has been studied theoretically. The four TMZ-BITC derivatives studied are discussed below:



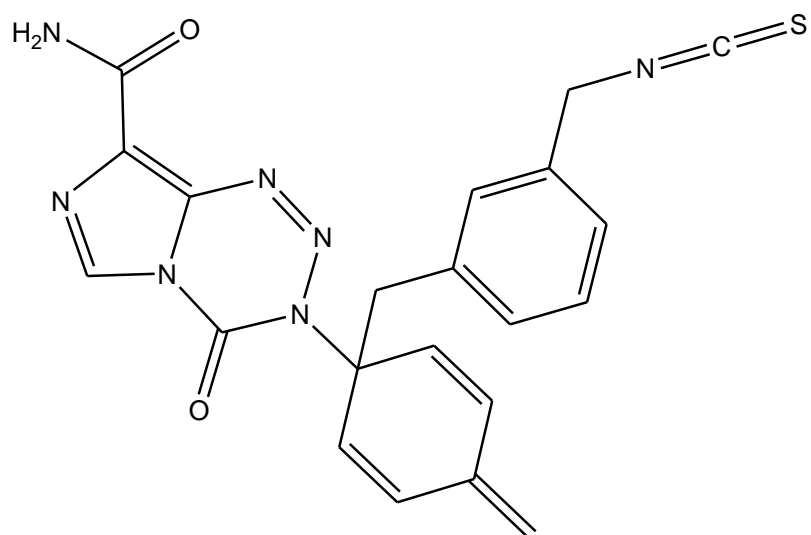
TMZ-BITC(1); 3,4-dihydro-3-(3-(isothiocyanatomethyl)phenyl)-4-oxoimidazo[5,1-d][1,2,3,5]tetrazine-8-carboxamide



TMZ-BITC(2) ; IUPAC name: 3-(4-(isothiocyanatomethyl)-1H-benzo[d]imidazole-2-carboxamido)-3,4-dihydro-4-oxoimidazo[5,1-d][1,2,3,5]tetrazine-8-carboxamide



TMZ-BITC(3) ; IUPAC name: 3-(1-(bicyclo[3.2.0]hept-6-en-3-yl)-2-(3-(isothiocyanatomethyl)phenyl)ethyl)-3,4-dihydro-4-oxoimidazo[5,1-d][1,2,3,5]tetrazine-8-carboxamide



TMZ-BITC(4) ; IUPAC name: 3-(1-(3-(isothiocyanatomethyl)benzyl)-4-methylenecyclohexa-2,5-dienyl)-3,4-dihydro-4-oxoimidazo[5,1-d][1,2,3,5]tetrazine-8-carboxamide

4.2 TMZ-BITC(1)

4.2.1 Optimization and properties in both media

TMZ-BITC(1) was optimized at DFT/B3LYP/6-311++G(d,p) level of theory in both the gas and the aqueous phases as depicted in **Table 4.1**. Furthermore, frequency calculations were performed at the same level of theory to ensure that the optimized structure corresponds to true energetic minima. Calculated results of optimizations of TMZ-BITC(1) in the gas phase and aqueous solution can be seen in **Figure 4.1**. The difference between the value optimized in the aqueous solution and the corresponding gas phase ($-1433.21 + 1433.19 = 0.025$ Hartrees = 66.69 kJ/mol) was used to calculate the relative energy. It can be seen that the calculated total energies (E) in both phases, as well as the corrected ZPVE energy (EZPVE) were primarily negative.

Table 4.1: Calculated total energies (E), dipole moments (μ), and volumes (V) for compound TMZ-BITC(1) in gas and aqueous phase phases by using B3LYP/6-311++G(d,p) basis set.

Medium	E (Hartrees)	E _{ZPVE} (Hartrees)	μ (D)	V(A ³)
Gas phase	-1432.97	-1433.19	3.79	305.3
Aqueous phase	-1432.99	-1433.21	3.77	308.8

4.2.2 Geometrical parameters

The optimized structure of TMZ-BITC(1) possess C_1 point group symmetry. The optimized geometrical parameters of TMZ-BITC(1) in both the gas phase and the aqueous solution are presented in **Table 4.2**. In the Tetrazine ring, the N-N and N=N bond length is found to be respectively 1.26 Å and 1.42 Å in gas phase and 1.26 Å and 1.4 Å in the aqueous solution. The C-N bond length in the molecule is calculated at 1.37 to 1.39 Å, which is similar with the aqueous solution. The C-N bond length linked with the BITC group is found to be 1.44 Å (N3-C17) in both phases. The C-N bond length in the isothiocyanate is 1.19 Å in gas phase and 1.18 Å in aqueous

solution. The two C=O bond lengths are 1.20 Å (1.21 Å in aqueous solution) and 1.22 Å (1.23 Å in aqueous solution) respectively in the gas phase. The C-C bond lengths in the benzyl ring are in the range of 1.39 Å to 1.4 Å in both phases. The C=S bond of Isocyanate group bond length is found to be 1.59 Å in gas phase and 1.61 Å in aqueous solution. The bond angle for N-N-N in the tetrazine ring is 120.05° in both phases. The C-C-C bond angles in the benzyl ring are in the range of 119.03° to 120.01°, which depicts the hexagonal shape of the benzene ring. The dihedral angles found for the TMZ and benzyl group shows planarity in the rings.

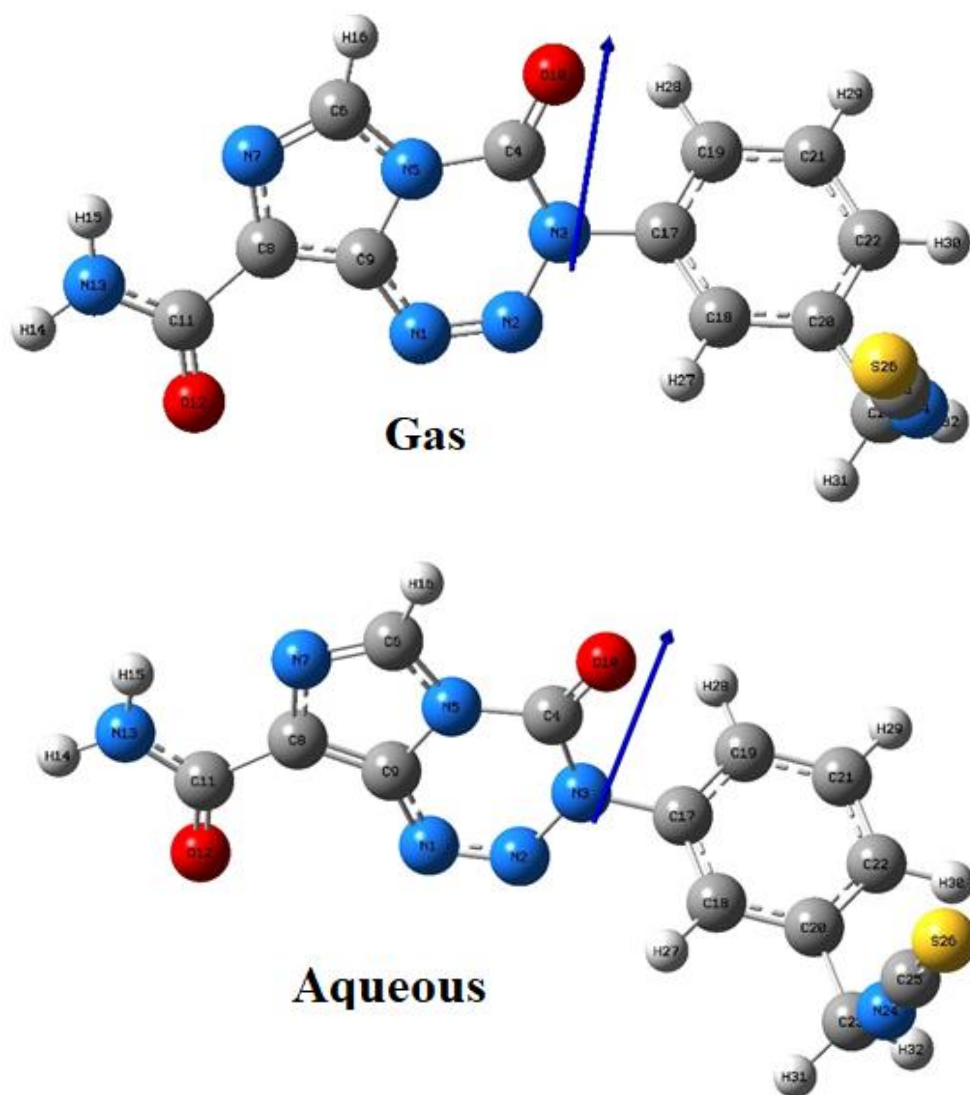


Figure 4.1: Optimized structure of TMZ-BITC(1) at B3LYP/6-311++G(d,p) basis set for gas phase (upper) and aqueous phase (bottom)

Table 4.2: Selected geometrical parameters of TMZ-BITC(1) using B3LYP/6-311++G(d,p) basis set.

Bond lengths(Å)		
Parameters	Gas	Aqueous
N1-N2	1.26	1.26
N1-C9	1.36	1.36
N2-N3	1.42	1.40
N3-C4	1.39	1.39
N3-C17	1.44	1.44
C4-O10	1.20	1.21
N5-C6	1.37	1.37
C8-C9	1.39	1.39
C11-O12	1.22	1.23
C17-C19	1.39	1.39
C20-C22	1.40	1.40
C21-C22	1.39	1.39
C23-H31	1.10	1.09
C23-H32	1.09	1.09
N24-C25	1.19	1.18
C25-S26	1.59	1.61
Bond angles(°)		
Parameters	Gas	Aqueous
N2-N1-C9	120.13	119.85
N1-N2-N3	120.05	120.08
N2-N3-C17	113.19	113.88
N3-C4-N5	110.13	110.42
N3-C4-O10	126.78	125.94
N5-C6-N7	110.73	110.63
N7-C8-C9	109.27	109.23
C17-C18-C20	119.95	119.52
C17-C19-C21	119.03	118.89
C18-C20-C23	119.98	120.01
C20-C23-N24	112.74	112.01
Dihedral angles(ϕ)		
Parameters	Gas	Aqueous
C9-N1-N2-N3	0.28	0.32
N2-N1-C9-N5	-0.15	-0.46
N2-N1-C9-C8	-179.90	179.78

N1-N2-N3-C4	0.49	0.99
N2-N3-C4-N5	-1.24	-1.90
C17-N3-C4-N5	-177.80	-179.09
C4-N5-C9-N1	-0.76	-0.67
C6-N7-C8-C9	0.01	-0.03
N7-C8-C11-N13	-0.17	-0.15
C19-C17-C18-C20	-0.17	-0.11
C18-C17-C19-C21	-0.30	-0.22
C17-C19-C21-C22	0.50	0.39
C23-C20-C22-C21	-179.10	-179.39

4.2.3 Atomic charges and MEP

The atomic charges and molecular electrostatic potentials (MEP) charges of the optimized structures of TMZ-BITC(1) for the gas phase and the aqueous solution are summarized in **Table 4.3**. The Mulliken charges on N-atoms shows that N3 is the most positive and N13 is the most negative in gas phase. While NPA atomic charges shows that all the N-atoms are negative except for N2 in both phases. Both Mulliken and NPA shows that the two O-atoms are negative. The trend for Mulliken and NPA charges in C-atoms differs. Certain C-atoms encompassing C8, C9, C11, C17, C18 and C20 shows positive in Mulliken atomic charge, while it is negative in NPA atomic charges. C4 is the most positive charge in NPA, and C20 is the most positive charge in the Mulliken charges. In aqueous solution, N-atom and C-atom shows huge differences of values between NPA and MEP atomic charges as compared to the gas phase.

The molecular electrostatic potential (MEP) charges presented in **Table 4.3** show trends of relative expected tendency as MEP O-atoms > MEP N-atoms. The MEP of TMZ-BITC(1) molecule shows the negative potential region around oxygen atom of O12 (carboxamide group) and the most positive region is localized on H13 of the amine group (N24 and N17), indicating a nucleophilic region and a possible site for electrophilic attack, respectively.

Table 4.3: Mulliken, Natural Population Analysis (NPA) charges (in a.u.) and Molecular Electrostatic Potentials (MEP) of TMZ-BITC(1) in the gas phase and aqueous solution calculated at B3LYP/6-311++G(d,p) level of theory.

Atoms	Gas Phase			Aqueous Phase		
	Mulliken	NPA	MEP	Mulliken	NPA	MEP
N1	-0.01	-0.16	-18.32	-0.15	-0.20	-18.33
N2	0.10	0.01	-18.29	0.11	0.01	-18.29
N3	0.18	-0.33	-18.27	0.30	-0.32	-18.26
C4	0.12	0.83	-14.58	0.12	0.85	-14.57
N5	-0.19	-0.45	-18.28	-0.13	-0.44	-18.26
C6	0.38	0.26	-14.67	0.66	0.27	-14.66
N7	-0.08	-0.47	-18.37	-0.12	-0.48	-18.36
C8	-0.10	0.07	-14.70	-0.14	0.06	-14.71
C9	-0.08	0.28	-14.66	0.05	0.30	-14.66
O10	-0.24	-0.57	-22.35	-0.28	-0.59	-22.35
C11	-0.08	0.63	-14.65	-0.05	0.64	-14.66
O12	-0.34	-0.60	-22.40	-0.45	-0.67	-22.43
N13	-0.42	-0.79	-18.36	0.24	-0.77	-18.36
C17	-0.88	0.15	-14.69	-0.56	0.14	-14.69
C18	0.00	-0.18	-14.74	-0.27	-0.18	-14.73
C19	-0.02	-0.18	-14.74	0.34	-0.18	-14.73
C20	0.90	-0.04	-14.73	0.82	-0.04	-14.72
C21	-0.16	-0.18	-14.74	0.08	-0.19	-14.74
C22	-0.46	-0.18	-14.74	-0.25	-0.17	-14.73
C23	-0.56	-0.19	-14.68	-0.12	-0.20	-14.66
N24	0.12	-0.45	-18.36	0.20	-0.40	-18.33
C25	0.10	0.23	-14.68	0.06	0.25	-14.68
S26	-0.33	-0.02	-59.25	-0.45	-0.14	-59.27

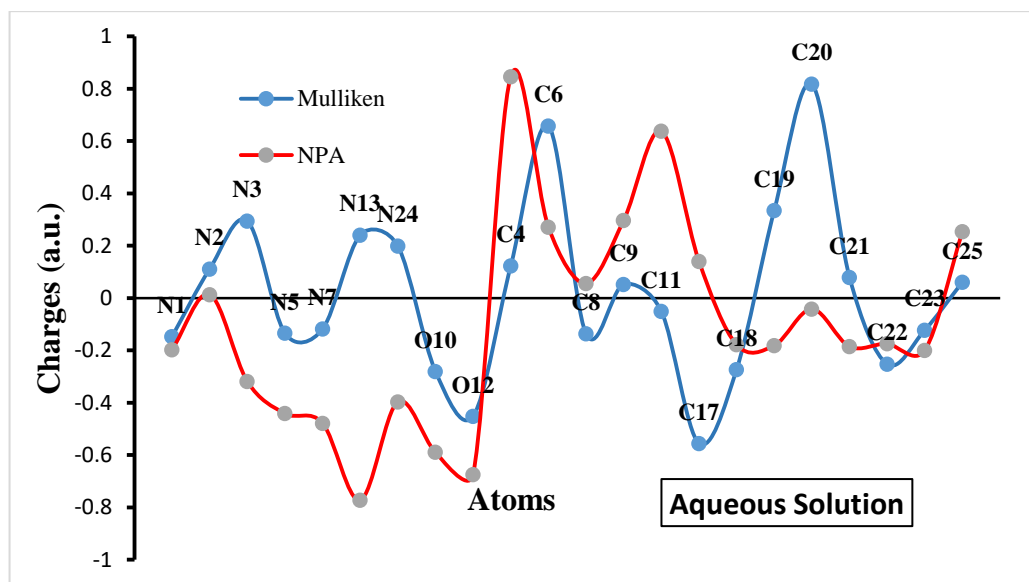
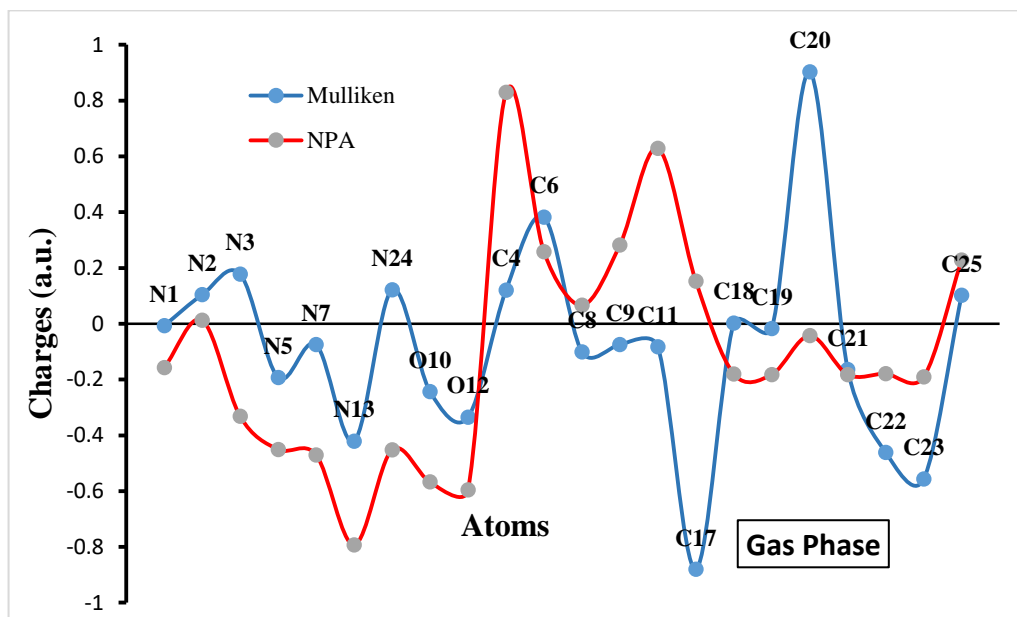


Figure 4.2: Graph showing the trends for Mulliken and Natural Population Analysis (NPA) Atomic charges of TMZ-BITC(1) in the gas phase (upper) and the aqueous solution (bottom).

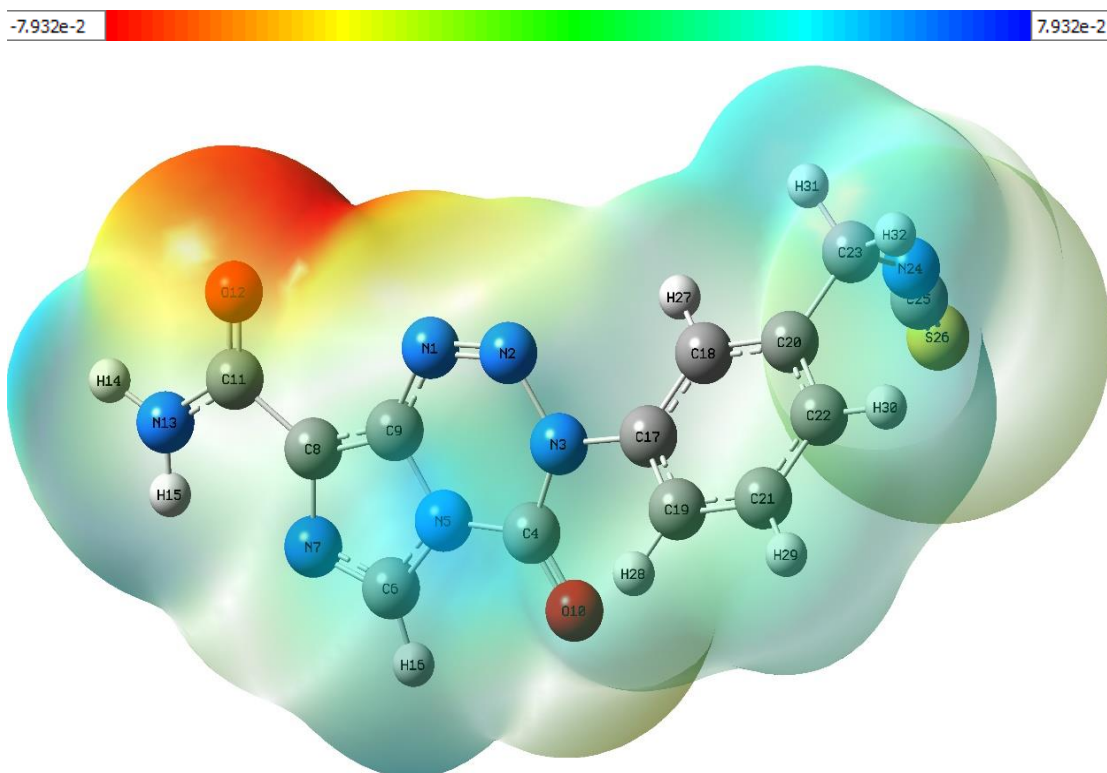


Figure 4.3: Calculated electrostatic potential surfaces on the molecular surface of TMZ-BITC(1) in the gas phase, using 6-311++G(d,p) basis set.

4.2.4 ^1H and ^{13}C NMR analysis

The ^1H and ^{13}C NMR calculations were performed by GIAO (Gauge-Independent Atomic Orbital) method at the B3LYP/6-311++G(d,p) basis set in DMSO solvent. The calculated chemical shift of TMZ-BITC(1) is shown in **Table 4.4**. The ^1H NMR of TMZ-BITC(1) in DMSO shows a chemical shift at 8.47 ppm (deshield) for H16 of imidazole ring. The two protons of NH_2 show chemical shifts at 7.32 ppm (H14) and 5.20 ppm (H15). The ^{13}C NMR calculations of the title show a chemical shift of 164.59 ppm (C11) of carboxamide group. The lowest chemical shift of 51.34 ppm is found for C23 (CH_2). The chemical shifts of aromatic carbons are calculated in the range of 130.87-144.42 ppm.

Table 4.4: Calculated chemical shifts of TMZ-BITC(1) in GIAO method using DMSO as solvents.

¹ H NMR		¹³ C NMR	
Atom	Calculated(ppm)	Atom	Calculated(ppm)
16-H	8.47	11-C	164.59
28-H	8.09	25-C	146.22
27-H	8.05	17-C	144.42
29-H	7.87	20-C	144.41
30-H	7.79	4-C	143.44
15-H	7.32	9-C	139.51
14-H	5.20	8-C	138.57
31-H	4.99	22-C	135.79
32-H	4.05	21-C	134.10
		6-C	134.04
		18-C	132.27
		19-C	130.87
		23-C	51.34

4.2.5 UV-vis analysis

The Wavelengths (λ) and the excitation energies (E) are both expressed in nm, and oscillator strength (f) of TMZ-BITC(1) evaluated by the TD-DFT method are shown in **Table 4.5** with **Figure 4.4** displaying the plot of the ultraviolet spectra. A strong theoretical absorption peak is found at 332.73 nm with oscillator strength of 0.14 and excitation energy of 3.73 eV. This peak is the major contribution of the excitation from HOMO-1 to LUMO, contributing 32%. The peak observed at 327.84 nm with oscillator strength of 0.02 and excitation energy of 3.78 eV has the major contribution with 47 % of HOMO to LUMO transition. The peak observed at 323.88 nm with oscillator strength of 0.03 and excitation energy of 3.83 eV has the major contribution from HOMO-1 to LUMO (37%).

Table 4.5: Electronics properties of TMZ-BITC(1) calculated using TD-DFT (B3LYP)/6-311++G(d,p).

Wavelength λ (nm)	Energy eV	Oscillator strength f	Symmetry	Major contributions
332.73	3.73	0.14	Singlet-A	H→L (32%), H-2→L (25%)
327.84	3.78	0.02	Singlet-A	H→L (47%), H-1→L (44%)
323.88	3.83	0.03	Singlet-A	H-1→L (37%), H-4→L (14%), H-2→L (15%), H→L (16%)

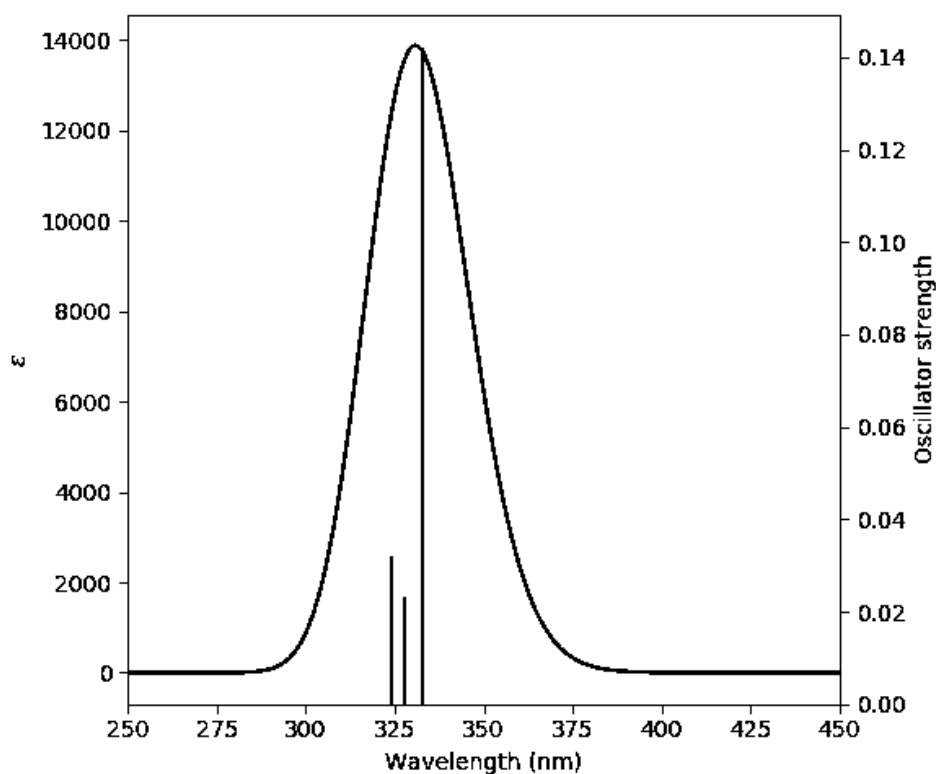


Figure 4.4: UV spectra of TMZ-BITC(1) calculated at B3LYP/6-311++G(d,p) basis set.

4.2.6 Frontier Molecular Orbitals analysis (FMO)

The computation results indicate that the molecule has 575 molecular orbitals, where 84 are occupied and the remaining are unoccupied molecular orbitals. Molecular orbitals 85 and 84 were identified as LUMO and HOMO molecular

orbitals, respectively. The HOMO and LUMO orbitals with energy values are shown in **Table 4.6**. HOMO is localized by π bonding type orbitals on TMZ and LUMO is localized by π^* bonding type orbitals on BITC molecule (**Figure 4.5**).

The LUMO and HOMO energies obtained are at -2.99 eV and 6.97 eV for the gas phase and -2.92 eV and -7.07 eV for the aqueous solution, respectively. The HOMO-LUMO energy gap (ΔE) in the gas phase is 3.98 eV and 4.14 eV for the aqueous phase. A slight increase in the energy gap is observed in the aqueous phase to that of the gas phase. This energy gap confirms the stability and prospective bioactivity of molecule. The tabulated FMO energy parameters and global reactivity descriptors of TMZ in both media are shown in **Table 4.6**. The electron affinity and electronegativity values of molecule shows a moderate acceptor properties as well as a high ability to pull electron density to itself. This could be attributed to the good number of N-atoms in the molecular structure with lone pairs of electrons donated for reactions. The high ionization potential of the molecule in both media indicates high reactivity of atoms and the molecule.

Table 4.6: Frontier Molecular Orbitals energy parameters and global reactivity descriptors of TMZ-BITC(1).

FMOs	Gas	PCM
HOMO energy	-6.97	-7.07
LUMO energy	-2.99	-2.92
Energy gap (ΔE)	3.98	4.14
Ionization potential (I)	6.97	7.07
Electron affinity (A)	2.99	2.92
Hardness (η)	1.99	2.07
Chemical potential (μ)	-4.98	-5.00
Electronegativity (χ)	4.98	5.00
Electrophilicity (ω)	6.24	6.02

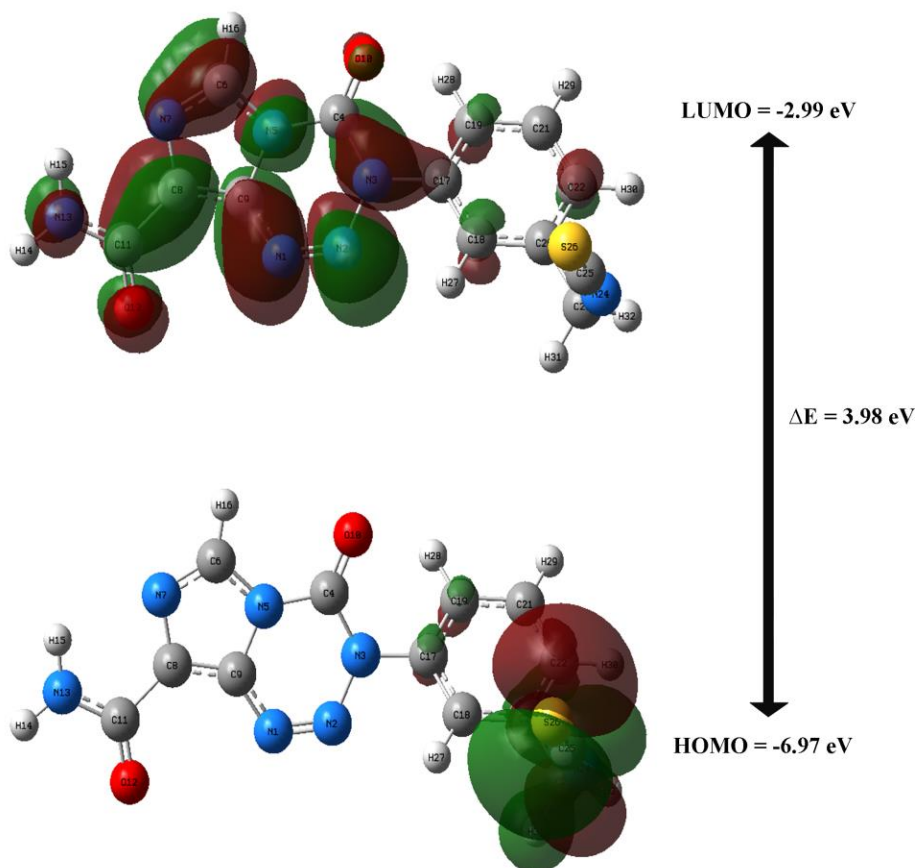


Figure 4.5: HOMO-LUMO graphical reproduction of TMZ-BITC(1)

4.2.7 Natural bond orbital (NBO) analysis

The interactions occurring between localized Lewis orbitals and vacant non-Lewis orbitals are listed in **Table 4.7**. The results of the natural bondorbital analysis showed that the strongest intramolecular hyperconjugative interaction in the $\pi \rightarrow \pi^*$ occurs via overlapping between $\pi(\text{C8-N9})$ bonding orbital participating as donor and the $\pi^*(\text{N1-N2})$ as an acceptor antibonding orbital, which ensues a stabilization energy of 23.62 kJ/mol. The other significant $\pi \rightarrow \pi^*$ interactions also occurs in the benzyl ring. Of all the interaction, those involving lone-pair LP(1) of nitrogen, LP(1) and LP(2) of oxygen towards the π^* are mostly higher than the other types of interaction. The lone-pair LP(1) N13 shows highest stabilizing energy of 69.65 kJ/mol with antibonding $\pi^*(\text{C11-O12})$. The LP(2) O10 also shows highest stabilizing energy of 28.12 kJ/mol with $\sigma^*(\text{C4-N5})$ among the LP to σ^* interactions. The appreciable highest interaction energies $\pi \rightarrow \pi^*$ orbital overlap intramolecular

interactions in the system occurs in the rings, $\pi(\text{C6-C7}) \rightarrow \pi^*(\text{C8-C9})$ with stabilizing energy of 92.39 kJ/mol and $\pi^*(\text{N1-N2}) \rightarrow \pi^*(\text{C8-C9})$ with stabilizing energy of 42.96 kJ/mol.

Table 4.7: Second-order perturbation theory analysis of Fock matrix in NBO of TMZ-BITC(1).

Donor (i)	Acceptor (j)	E2 kJ/mol	E(j)-E(i) a.u.	F(i,j) a.u.
$\pi(\text{N1-N2})$	$\pi^*(\text{C8-C9})$	14.24	0.40	0.07
$\pi(\text{C6-N7})$	$\pi^*(\text{C8-C9})$	21.40	0.33	0.08
$\pi(\text{C8-C9})$	$\pi^*(\text{N1-N2})$	23.62	0.23	0.07
	$\pi^*(\text{C6-N7})$	17.41	0.28	0.06
	$\pi^*(\text{C11-O12})$	16.52	0.30	0.06
$\pi(\text{C17-C19})$	$\pi^*(\text{C18-C20})$	21.32	0.30	0.07
	$\pi^*(\text{C21-C22})$	17.85	0.30	0.07
$\pi(\text{C18-C20})$	$\pi^*(\text{C17-C19})$	20.77	0.28	0.07
	$\pi^*(\text{C21-C22})$	20.37	0.29	0.07
$\pi(\text{C21-C22})$	$\pi^*(\text{C17-C19})$	22.81	0.27	0.07
	$\pi^*(\text{C18-C20})$	20.84	0.28	0.07
LP(1) N1	$\sigma^*(\text{N2-N3})$	17.54	0.68	0.10
LP(1) N3	$\pi^*(\text{N1-N2})$	40.33	0.24	0.09
	$\pi^*(\text{C4-O10})$	55.68	0.28	0.11
LP(1) N5	$\pi^*(\text{C4-O10})$	46.90	0.28	0.11
	$\pi^*(\text{C6-N7})$	41.40	0.29	0.10
	$\pi^*(\text{C8-C9})$	30.99	0.30	0.09
LP(2) O10	$\sigma^*(\text{N3-C4})$	27.44	0.66	0.12
	$\sigma^*(\text{C4-N5})$	28.12	0.64	0.12
LP(2) O12	$\sigma^*(\text{C8-C11})$	18.44	0.67	0.10
	$\sigma^*(\text{C11-N13})$	22.82	0.73	0.12
LP(1) N13	$\pi^*(\text{C11-O12})$	69.65	0.27	0.12
	$\sigma^*(\text{N24-C25})$	18.04	1.54	0.15
	$\pi^*(\text{N24-C25})$	61.59	0.25	0.11
$\pi^*(\text{N1-N2})$	$\pi^*(\text{C8-C9})$	42.96	0.06	0.08
$\sigma^*(\text{N3-C4})$	$\sigma^*(\text{N5-C9})$	16.91	0.01	0.05
$\pi^*(\text{C6-N7})$	$\pi^*(\text{C8-C9})$	92.39	0.02	0.06

Note: where E(2) = Energy of hyper conjunctive interactions; E(j)-E(i) = Energy difference between the donor (i) and acceptor (j) NBO orbitals and F(i,j) = Fock matrix element between i and j NBO orbital.

4.2.8 Vibrational Assignment

The TMZ-BITC(1) molecule with 32 atoms produces 90 normal modes of vibrations from the $3N-6$ relation, consisting of 31 stretching, 30 bending, and 29 torsional modes as tabulated in **Table 4.8**. There are 31 modes related to C-H bonds out of 90 normal modes. The 90 normal vibrational modes are assigned based on the detailed movement of individual atoms. The computed wavenumbers obtained are usually higher than the observed wavenumbers due to the combination of electron similarity effects and DFT basis set deficiencies. As a result, scaling factors are used to fit the experimental values, with a scaling factor of 0.958 for values greater than 1800 cm^{-1} and a scaling factor of 0.983 for values less than 1800 cm^{-1} . Only Potential energy distribution contributions (PED) $\geq 10\%$ were considered in the assignments of vibration modes. The calculated wavenumbers and assignments for TMZ-BITC(1) in gas phase by using the B3LYP/6-311++G(d,p) method are shown in **Figure 4.6**. After that, a brief discussion of assignments by regions is presented at continuation.

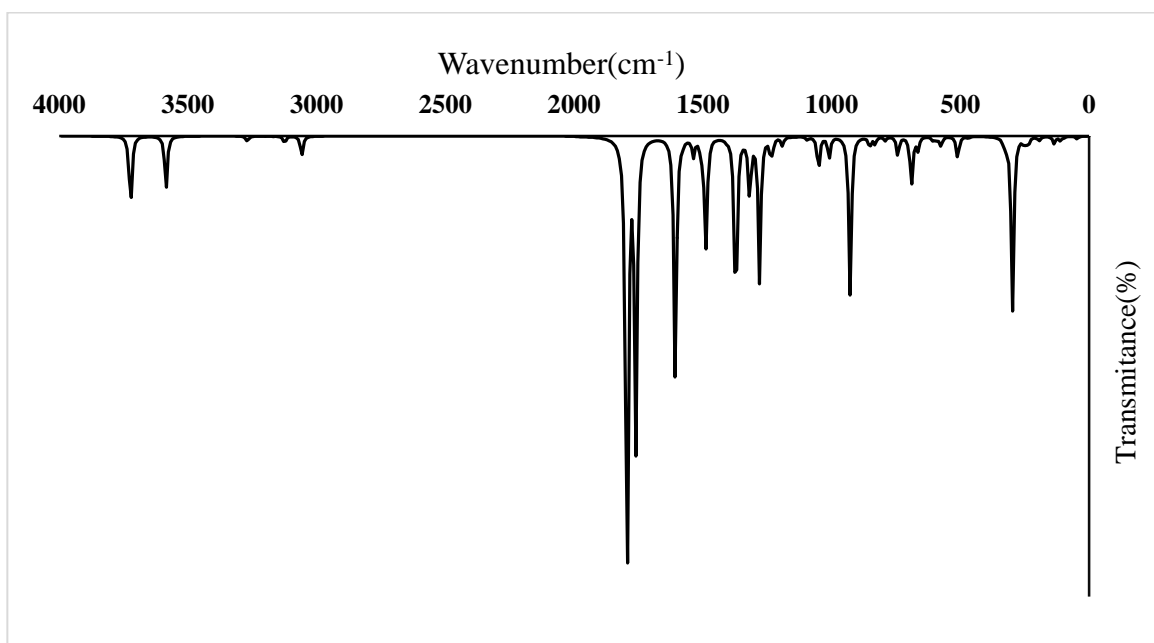


Figure 4.6: DFT FT-IR spectra of TMZ-BITC(1).

Assignments bands:

4000–2000 cm⁻¹ region:

In this region, the stretching modes of N–H, C–H, N=C and CH₃ groups present in TMZ-BITC(1) are expected. The bands characteristics of NH groups are generally observed around 3500–3300 cm⁻¹. This absorption is strongly influenced by the chemical environment, in particular when NH groups are involved in the intramolecular or intermolecular hydrogen bond. In this case, the SQM calculations predict the NH stretching modes of amide at 3566.08 and 3434.65 cm⁻¹. Normally, in related compounds the CH stretching vibrations of aromatic rings are assigned in the region 3200–3000 cm⁻¹. For TMZ-BITC(1), the CH stretching modes were predicted by calculations between 3036.67 and 3059.79 cm⁻¹. The C–H stretching mode corresponding to CH₂ group is predicted the SQM calculations at 2911.99 and 2959.49 cm⁻¹. The N=C stretching modes of isothiocyanate group is predicted at 2057.39. The instance peak is observed for the C=N of isothiocyanate group at 2147.59 cm⁻¹.

2000-1000 cm⁻¹ regions:

The C=O, C=C, S=C, C–C, N=N and C–N stretching modes, deformation and rocking modes of NH, CH and CH₃ groups and, some deformations of tetrazine and benzyl rings of TMZ-BITC(1) are characteristics of this region. In particular, the C=O stretching mode is usually assigned free of other vibrations (1800–1600 cm⁻¹). Here, the C=O stretching mode is predicted by calculation as an intense band at 1714 cm⁻¹. In particular, the C=O stretching mode is usually assigned free of other vibrations (1800–1600 cm⁻¹). Here, the two C=O stretching mode is predicted at 1767.88 and 1730.29 cm⁻¹. The N=N stretching mode of tetrazine ring calculated at 1515.09 and 1489.87 cm⁻¹. The C–N stretching modes of imidazole ring is calculated at 1350.04 and 1383.39 cm⁻¹. The C=C stretching modes at 1555.60 cm⁻¹. The benzyl ring in plane and out plane calculated at 1309.89 and 1617.55 cm⁻¹. CH₂ wagging at 1580.83 and 1347.16 cm⁻¹, and rocking mode at 1495.04 cm⁻¹, and scissoring at 1472.30 cm⁻¹. C–H rocking modes of imidazole ring at 1201.56 and 1213.25 cm⁻¹.

1000-0 cm⁻¹ regions:

In this region, the S-C stretching, C-H and N-H out-of-plane deformations, deformations, wagging and twisting modes of C=O group, deformations and torsions modes of rings of TMZ-BITC(1) are calculated. The S-C stretching of imidazole group is calculated at 684.42 and 705.37 cm⁻¹. The out-of-plane of benzyl ring is calculated at 796.09-890.78 cm⁻¹, carboxamide at 730.06 -784.34 cm⁻¹. The N-H of NH₂ group is calculated at 553.27 and 580.02 cm⁻¹. The out-of-plane of the whole molecule is calculated at 461.89-0 cm⁻¹.

Table 4.8: Vibrational assignments of TMZ-BITC(1) fundamental modes along with calculated IR and PED using the B3LYP method.

Mode	Calculated (cm ⁻¹)	Scaled (cm ⁻¹)	Intensity (kM/mol)	Characterization of normal modes with PED (%)
90	3722.42	3566.08	88.10	ν_a NH2 (99)
89	3585.23	3434.65	67.81	ν_s NH2 (99)
88	3269.51	3132.19	7.54	ν C6-H16 (99)
87	3217.29	3082.16	0.63	ν_s C19-H28 (94)
86	3193.94	3059.79	0.05	ν C18-H27 (97)
85	3188.66	3054.73	11.36	ν C21-H29 (74) ν C22-H30 (18)
84	3169.80	3036.67	3.40	ν C21-H29 (18) ν C22-H30 (81)
83	3089.24	2959.49	10.65	ν_a CH2 (85)
82	3039.66	2911.99	26.77	ν_a CH2 (85)
81	2147.59	2057.39	1228.51	ν N24=C25 (83)
80	1798.46	1767.88	426.42	ν O10-C4 (86)
79	1760.21	1730.29	323.30	ν O12-C11 (79)
78	1645.52	1617.55	12.15	ν C18-C17 (11) ν C22-C21 (28)
77	1631.45	1603.72	11.49	ν C19-C17 (31) ν C20-C18 (11) β C20C18C17 (12)
76	1608.17	1580.83	294.93	β NH2 (53)
75	1582.50	1555.60	6.88	ν C9-C8 (43) β N13-H15 (24)
74	1541.29	1515.09	26.70	ν N2=N1 (66)
73	1520.89	1495.04	29.97	β C18-C20 (14) β 9C21-C22 (30)
72	1497.77	1472.30	9.52	β C23-H31 (86)
71	1489.87	1464.54	151.34	ν N2=N1 (11) ν N7-C6 (28) β C6-N7 (26)
70	1477.90	1452.77	21.30	ν C18C17 (13) ν C20C18 (19) β C19C21 (12) ν R1(A1) C22C21 (12)
69	1407.31	1383.39	0.69	ν N7-C6 (10) ν N5-C6 (26) ν N5-C4 (16)
68	1373.39	1350.04	252.77	ν N7-C6 (13) ν N1-C9 (23) ν N13C11 (10) ν C11C8 (11) β C9C8N7 (14)

67	1370.46	1347.16	67.06	β C23N24 (12) τ C23N24 (29) τ C23N24 (41)
66	1347.91	1325.00	0.94	υ C18C17 (11) υ C21C19 (14) υ C22C21 (15) β H27C18C20 (18) β H28C19C21 (14) β H30C22C21 (14)
65	1345.31	1322.44	0.52	υ N5C6 (15) β N7C6 (11) β C8N7C6 (10)
64	1332.55	1309.89	28.05	υ C18C17 (10) β H27C18C20 (14) β H29C21C22 (13) β H31C23N24 (16)
63	1323.27	1300.77	86.80	υ N3C4 (14) υ N3C17 (24)
62	1277.60	1255.88	208.66	υ N13C11 (10) υ N7C8 (35) υ N5C4 (10) β N7C6N5 (11)
61	1255.87	1234.52	17.59	β H31C23N24 (55) τ H32C23N24C25 (13)
60	1234.23	1213.25	3.60	υ N5C6 (15) β H16C6N7 (11)
59	1222.34	1201.56	7.47	υ C23C20 (12) β H16C6N7 (22)
58	1198.62	1178.24	4.46	υ C21C19 (12) β H28C19C21 (18) β H29C21C22 (36) β H30C22C21 (10)
57	1195.82	1175.49	29.05	υ C23C20 (10) β H16C6N7 (12) β H27C18C20 (11) β H30C22C21 (10)
56	1133.22	1113.95	24.40	υ N3C4 (16) β H27C18C20 (17)
55	1123.66	1104.56	26.35	υ C21C19 (11) υ C22C21 (15) υ N24C23 (14) υ S26C25 (11) β H28C19C21 (13) β H30C22C21 (15)
54	1111.16	1092.27	3.19	υ N24C23 (37) υ S26C25 (29)
53	1091.09	1072.54	0.38	υ N13C11 (18) β H15N13C11 (55)
52	1029.74	1012.24	13.20	υ N13C11 (14) υ N3C4 (13) β N1C9C8 (11)
51	1018.84	1001.52	0.56	υ C19C17 (12) υ C21C19 (10) β C22C21C19 (32) β C19C17C18 (14) β C21C19C17 (15)
50	1007.75	990.62	58.89	υ N3C4 (11) β N5C4N3 (15) β N7C6N5 (11) β C8N7C6 (15)
49	996.40	979.46	1.55	τ H28C19C21C22 (10) τ H29C21C22C20 (41) τ H30C22C21C19 (14) τ C22C21C19C17 (23)
48	981.69	965.00	122.42	β N2N1C9 (16) β C8N7C6 (10)
47	952.64	936.44	42.49	β N2N1C9 (17) τ H31C23N24C25 (10) τ C25N24C23C20 (10)
46	929.81	914.00	4.73	τ H28C19C21C22 (40) τ H30C22C21C19 (43)
45	906.19	890.78	12.13	τ H27C18C20C23 (68) τ C20C18C17C19 (11)
44	875.96	861.07	53.99	υ C23C20 (13) β N2N1C9 (16) β C21C19C17 (18)

43	838.42	824.17	7.12	τ H16C6N7C8 (83)
42	809.86	796.09	9.24	τ H28C19C21C22 (17) τ H29C21C22C20 (41) τ H30C22C21C19 (10)
41	797.91	784.34	3.61	τ C9C8N7C6 (16) τ O12N13C8C11 (55) γ C11C9N7C8 (17)
40	769.08	756.01	2.37	β C21C19C17 (11)
39	742.69	730.06	23.34	γ O10N5N3C4 (81)
38	717.57	705.37	66.16	υ S26C25 (15) τ H30C22C21C19 (18) γ C23C18C22C20 (15)
37	703.44	691.48	5.77	υ N1C9 (12) β C9C8N7 (10)
36	697.91	686.04	8.60	τ N2N1C9N5 (23) τ C9C8N7C6 (21))
35	696.25	684.42	7.37	υ S26C25 (13)
34	685.70	674.04	83.60	υ N1C9 (13) υ C11C8 (12) β O12C11N13 (11)
33	664.89	653.58	15.97	τ C8N7C6N5C (48)
32	637.77	626.93	17.05	β N2N1C9 (13) β C19C17C18 (10)
31	624.16	613.55	18.95	β N24C23C20 (11) γ N3C18C19C17 (12)
30	590.05	580.02	5.98	τ N13C11 (23) τ N13C11 (24)
29	589.38	579.36	1.33	β O12C11N13 (11) β N1C9C8 (16) τ H14N13C11C8 (11)
28	562.84	553.27	21.23	β N1C9C8 (16)
27	546.17	536.88	8.65	τ N2N1C9N5 (14) τ C6N5C4N3C (12) γ N1N5C8C9 (13)
26	536.13	527.01	31.77	τ C6N5C4N3C (12)
25	495.74	487.31	30.67	β S26C25N24 (70)
24	469.88	461.89	1.50	β N13C11C8 (11)
23	454.33	446.61	1.28	τ C22C21C19C17 (14) τ S26C25N24C23 (24)
22	449.69	442.05	0.81	τ S26C25N24C23 (68)
21	433.35	425.98	2.89	β N3C17C19 (28) β C23C20C22 (14)
20	371.84	365.52	5.71	υ C11C8 (10) β N13C11C8 (23)
19	321.02	315.56	9.32	β N24C23C20 (12) β C23C20C22 (21)
18	316.58	311.20	2.53	β O10C4N3 (25)
17	305.09	299.90	91.27	τ H14N13C11C8 (15) τ H15N13C11C8 (16)
16	298.65	293.57	107.19	τ H14N13C11C8 (25) τ H15N13C11C8 (22)

15	282.30	277.50	4.36	β N13C11C8 (16) τ C21C19C17C18 (14)
14	236.60	232.57	5.42	γ N1N5C8C9 (36)
13	230.02	226.11	3.04	δ N3C17 (11) γ N1N5C8C9 (14)
12	220.03	216.29	10.15	τ N7C6N5C4 (32) γ C11C9N7C8 (36)
11	159.37	156.66	1.64	τ C21C19C17C18 (11) τ C6N5C4N3C (18) γ C23C18C22C20 (16)
10	145.32	142.85	3.32	β C11C8N7 (36)
9	125.22	123.09	3.71	τ C6N5C4N3C (21) γ C23C18C22C20 (13)
8	87.79	86.29	1.88	τ N7C6N5C4 (29) τ N5C4N3C17 (20) γ C11C9N7C8 (20)
7	79.38	78.03	8.08	β C25N24C23 (32) β C4N3C17 (13)
6	68.63	67.46	3.58	β C25N24C23 (32) β C4N3C17 (10) γ N3C18C19C17 (14)
5	51.04	50.17	1.35	τ N13C11C8C9 (69)
4	32.96	32.40	1.90	τ N7C6N5C4 (13) τ N13C11C8C9 (13) τ C6N5C4N3C (11) τ N5C4N3C17 (37)
3	26.41	25.96	1.30	τ C4N3C17C18 (62)
2	14.08	13.84	0.81	τ C25N24C23C20 (44) τ C4N3C17C18 (12) τ N24C18 (16)
1	5.79	5.69	0.55	τ C25N24C23C20 (40)

Symbol for stretching here: stretching (a = antisymmetric; s = symmetric); β = deformation in the plane; γ = deformation out of the plane; τ = torsion; β R = deformation ring; τ R = torsion ring; τ w = twisting; δ = deformation; and R = Ring

4.3 TMZ-BITC(2)

4.3.1 Optimization and properties in both media:

TMZ-BITC(2) was optimized at DFT/B3LYP/6-311++G(d,p) level of theory in both the gas and the aqueous phases as depicted in **Figure 4.7**. Furthermore, frequency calculations were performed at the same level of theory to ensure that the optimized structure corresponds to true energetic minima. Results of optimizations of TMZ-BITC(2) in the gas phase and aqueous solution can be seen in **Table 4.1**. The difference between the value optimized in the aqueous solution and the corresponding gas phase ($-1749.64 + 1749.60 = 0.04$ Hartrees = 100.29 kJ/mol) was used to calculate the relative energy. It can be seen that the calculated total energies (E) in both phases, as well as the corrected ZPVE energy (EZPVE), were primarily negative. The differences in dipole moments (μ) from 8.37 D in the gas phase to 13.55 D in the aqueous solution imply that an ionic bond is more prominent in the predicted solution with increased polarity. Decrease or contraction of volume can be seen in aqueous solution from 367.2 A³ to 361.5 A³.

Table 4.9: Calculated total energies (E), dipole moments (μ), and volumes (V) for compound TMZ-BITC(2) in gas and aqueous phases using B3LYP/6-311++ G(d,p) basis set.

Medium	E (Hartrees)	EZPVE (Hartrees)	μ (D)	V(A ³)
Gas phase	-1749.34	-1749.60	8.37	367.2
Aqueous phase	-1749.37	-1749.64	13.55	361.5

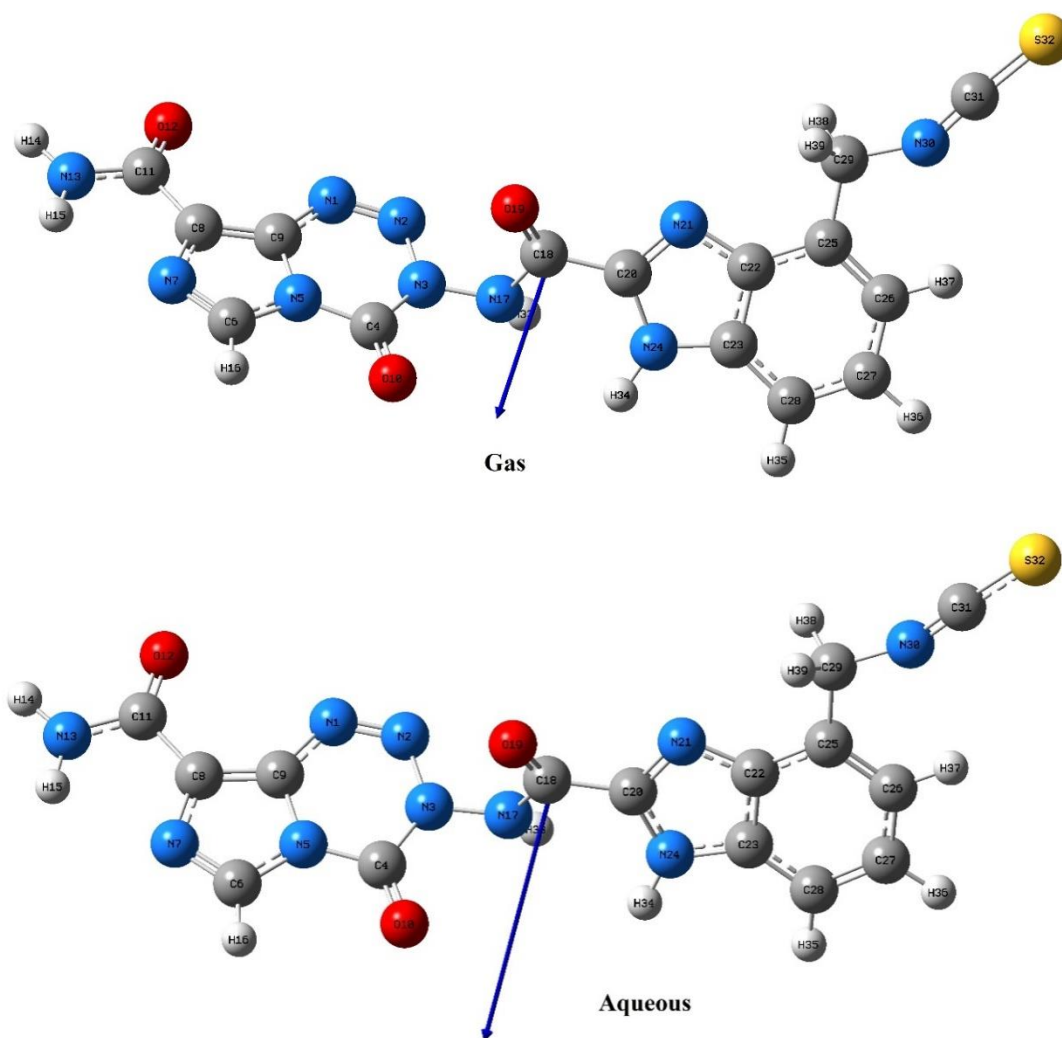


Figure 4.7: Optimized structure of TMZ-BITC(2) at B3LYP/6-311++G(d,p) basis set. (a) gas phase (b) aqueous solution

4.3.2 Geometrical parameters

The optimized structure of TMZ-BITC(2) possess C_1 point group symmetry. The optimized geometrical parameters of TMZ-BITC(2) in gas phase and aqueous solution using B3LYP/ 6-311++G(d,p) method are presented in **Table 4.10**. The bond length of N1-N2 in TMZ is found to be 1.25 Å in gas phase and 1.25 Å in aqueous solution. C-C bond length is found to be in the range of 1.49 Å to 1.51 Å in both phases. There are three C=O bond whose bond length is found between 1.20 Å to 1.21 Å in both phases. The C-C bond length of benzene ring in BITC is found in the

range of 1.39 Å to 1.41 Å. The C=S bond and C=N bond of Isocyanate group bond lengths are 1.59 Å and 1.19 Å in the gas phase (1.60 Å and 1.18 Å in aqueous solution) respectively. The bond angle of N1-N2-N3=118.88° (119.08° in aqueous solution), N3-C4-N5=108.89° (109.30° in aqueous solution), and N2-N1-C9 = 120.18° (120.10° in aqueous solution) indicates an irregular hexagon structure of tetrazine ring. And the bond angles of C22-C23-C28, C23-C22-C25 and C25-C26-C25 in both the phases also indicates a slightly irregular hexagon structure of the benzyl ring. The two rings (benzyl and imidazole ring) are co-planar to each other.

Table 4.10: Selected geometrical parameters of TMZ-BITC(2) using B3LYP/6-311++G(d,p) basis set.

Bond lengths(Å)		
Parameters	Gas	Aqueous
N1-N2	1.25	1.26
N1-C9	1.37	1.37
N2-N3	1.42	1.40
N3-C4	1.39	1.40
N3-N17	1.37	1.37
C4-O10	1.20	1.20
N5-C6	1.37	1.37
C8-C9	1.39	1.39
N13-H14	1.01	1.01
C18-O19	1.20	1.21
C18-C20	1.49	1.49
C22-C23	1.41	1.41
C23-N24	1.38	1.38
N24-H34	1.01	1.01
C25-C29	1.51	1.51
N30-C31	1.19	1.18
C31-S32	1.59	1.60
Bond angles(°)		
Parameters	Gas	Aqueous
N2-N1-C9	120.12	120.10
N1-N2-N3	118.88	119.08
N2-N3-N17	114.12	114.23
N3-C4-N5	108.89	109.30
N3-C4-O10	126.63	126.01

N5-C6-N7	110.79	110.67
N5-C6-H16	122.14	122.38
N7-C8-C11	121.89	121.81
C8-C11-O12	122.38	122.08
C8-C11-N13	113.12	113.80
N17-C18-C20	112.27	114.29
C22-C23-C28	122.45	122.58
N30-C31-S32	175.88	176.95
C23-C22-C25	120.61	120.47
C25-C26-C25	121.77	121.82
C29-N30-C31	148.05	159.52
Dihedral angles(ϕ)		
Parameters	Gas	Aqueous
N2-N1-C9-N5	0.33	0.14
N1-N2-N3-C4	-4.76	-2.48
N1-N2-N3-N17	-175.70	-178.11
N2-N3-C4-N5	3.60	2.38
O10-C4-N5-C6	0.13	-0.33
C9-N5-C6-N7	0.18	0.10
C9-N5-C6-H16	-179.78	-179.97
N7-C8-C9-N1	-178.71	-179.53
N7-C8-C11-O12	-177.60	179.73
O12-C11-N13-H14	-0.09	-0.16
O19-C18-C20-N21	-33.96	-28.72
C20-N21-C22-C23	-0.32	-0.39
C23-C22-C25-C29	179.71	179.70
C22-C23-C28-C27	-0.59	-0.57
C25-C26-C27-C28	0.24	0.16
C26-C27-C28-C23	0.02	0.11
C25-C29-N30-C31	179.63	-179.75

4.3.3 Atomic charges and MEP

The atomic charges and molecular electrostatic potentials (MEP) charges of the optimized structures of TMZ-BITC(2) for the gas phase and the aqueous solution are summarized in **Table 4.11**. The trends in the Mulliken and NPA charges on N-atoms are different, thus some N-atoms are positive in Mulliken, negative in NPA and vice versa. Most of the N atoms shows negative values in NPA but in Mulliken most shows positive values. O-atoms show negative values in both the Mulliken and

NPA. Certain C-atoms values in both the Mulliken and NPA shows opposite charge. C4 is the most positive and C28 is the most negative in NPA while C6 is the most positive and C9 is the most negative in Mulliken charges. Both NPA and MEP atomic charges shows the same trend in both the media except for N2 and C27 of NPA charges.

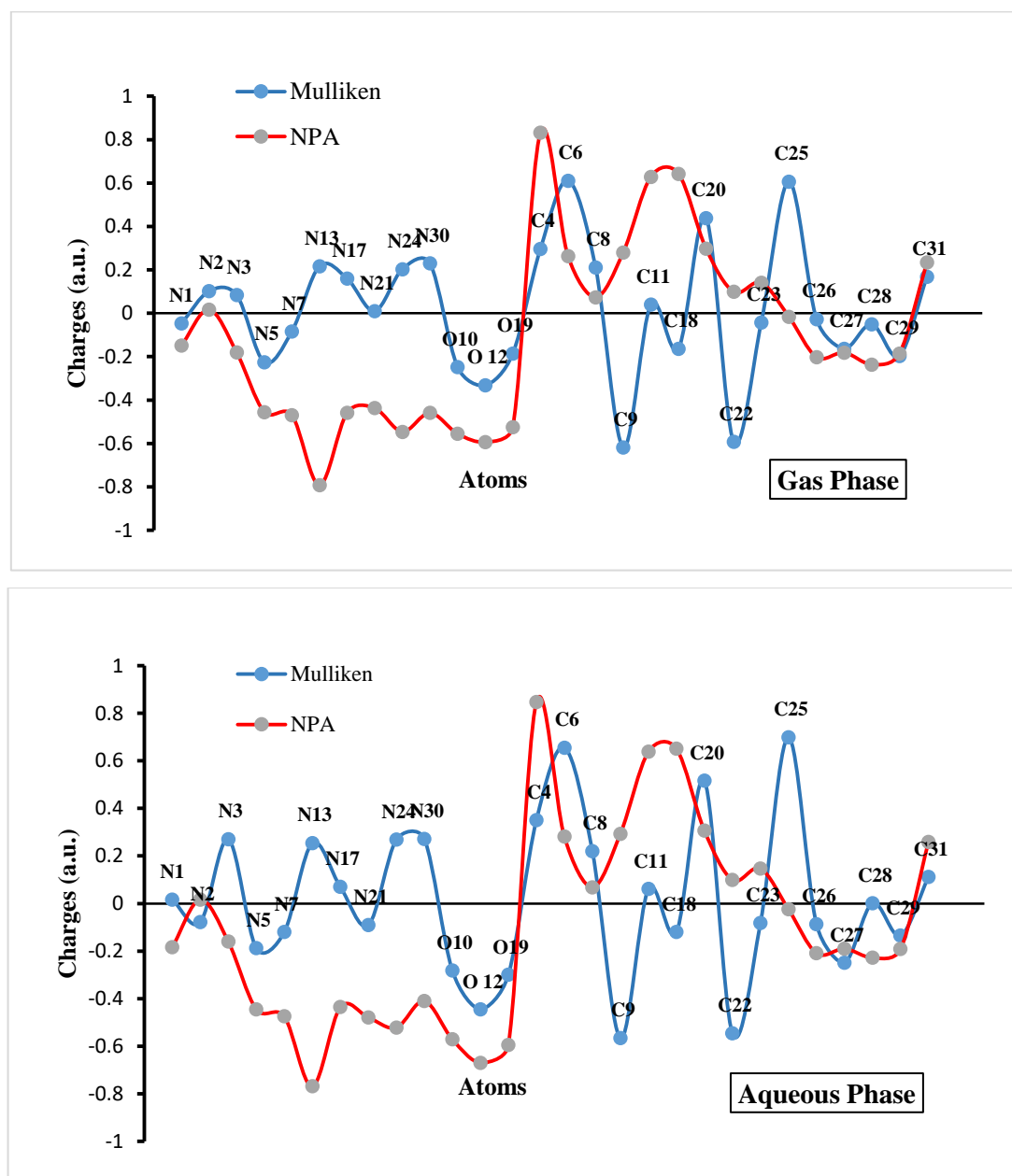


Figure 4.8: Graph showing the trends for Mulliken and Natural Population Analysis (NPA) Atomic charges of TMZ-BITC(2) in the gas phase (upper) and the aqueous solution (bottom).

Table 4.11: Mulliken, Natural Population Analysis (NPA) charges (in a.u.) and Molecular Electrostatic Potentials (MEP) of TMZ-BITC(2) in the gas phase and aqueous solution calculated at B3LYP/6-311++G(d,p) level of theory.

Atoms	Gas Phase			Aqueous Solution		
	Mulliken	NPA	MEP	Mulliken	NPA	MEP
N1	-0.05	-0.15	-18.31	0.02	-0.18	-18.33
N2	0.10	0.02	-18.28	-0.08	0.02	-18.28
N3	0.08	-0.18	-18.24	0.27	-0.16	-18.22
C4	0.30	0.83	-14.57	0.35	0.85	-14.55
N5	-0.23	-0.46	-18.27	-0.19	-0.45	-18.25
C6	0.61	0.26	-14.66	0.66	0.28	-14.65
N7	-0.08	-0.47	-18.36	-0.12	-0.48	-18.35
C8	0.21	0.07	-14.70	0.22	0.07	-14.70
C9	-0.62	0.28	-14.66	-0.57	0.29	-14.65
O10	-0.25	-0.56	-22.34	-0.28	-0.57	-22.33
C11	0.04	0.63	-14.65	0.06	0.64	-14.66
O12	-0.33	-0.59	-22.40	-0.45	-0.67	-22.43
N13	0.22	-0.79	-18.36	0.25	-0.77	-18.35
N17	0.16	-0.46	-18.29	0.07	-0.44	-18.26
C18	-0.16	0.64	-14.62	-0.12	0.65	-14.62
O19	-0.19	-0.53	-22.35	-0.30	-0.60	-22.38
C20	0.44	0.30	-14.67	0.52	0.31	-14.66
N21	0.01	-0.44	-18.38	-0.09	-0.48	-18.39
C22	-0.59	0.10	-14.72	-0.55	0.10	-14.72
C23	-0.04	0.14	-14.70	-0.08	0.15	-14.69
N24	0.20	-0.55	-18.30	0.27	-0.52	-18.27
C25	0.61	-0.02	-14.74	0.70	-0.02	-14.74
C26	-0.03	-0.20	-14.76	-0.09	-0.21	-14.75
C27	-0.16	-0.18	-14.75	-0.25	-0.19	-14.74
C28	-0.05	-0.24	-14.74	0.00	-0.23	-14.73
C29	-0.20	-0.19	-14.69	-0.14	-0.19	-14.69
N30	0.23	-0.46	-18.36	0.27	-0.41	-18.34
C31	0.17	0.24	-14.68	0.11	0.26	-14.68
S32	-0.41	-0.02	-59.25	-0.47	-0.13	-59.27

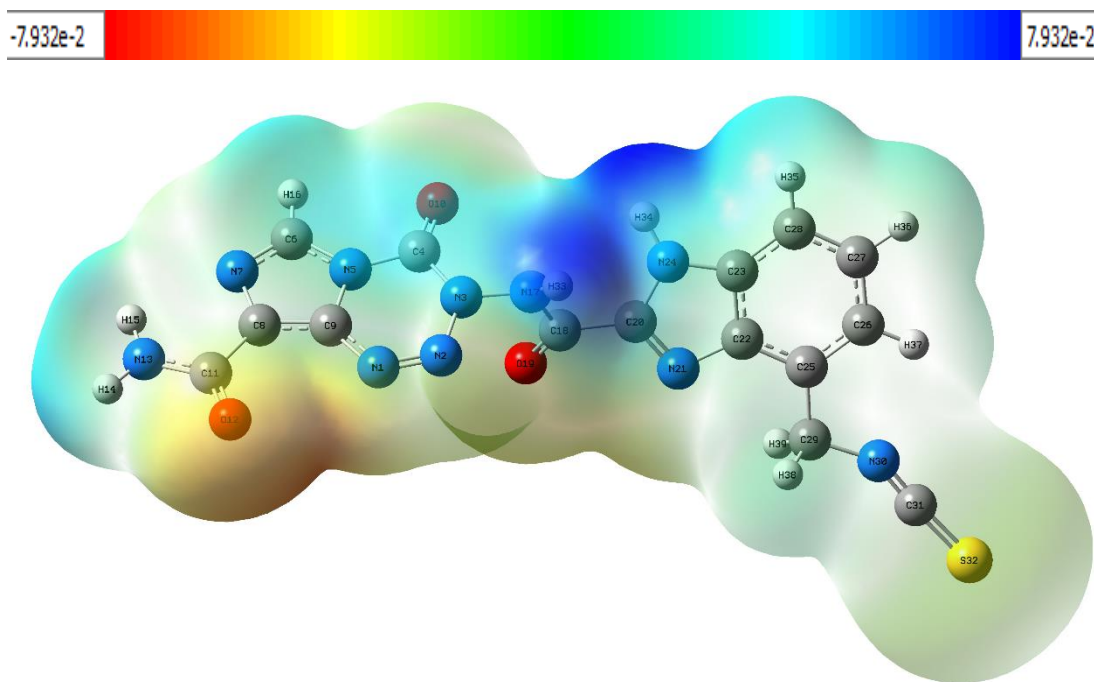


Figure 4.9: Calculated electrostatic potential surfaces on the molecular surface of TMZ-BITC(2) in the gas phase, using 6-311++G(d,p) basis set.

The molecular electrostatic potentials (MEP) charges are also presented in **Table 4.11**. The same trends of values are observed in both media and the relative expected tendency is observed as MEP O-atoms > MEP N-atoms. The MEP of TMZ-BITC(2) molecule shows the negative potential region around oxygen atom of O12 and the most positive region is localized on H21 of amine group and N13 atom indicating a nucleophilic region and a possible site for electrophilic attack, respectively.

4.3.4 ^1H and ^{13}C NMR analysis

The ^1H and ^{13}C NMR calculations were performed by GIAO (Gauge-Independent Atomic Orbital) method at the B3LYP/6-311++G(d,p) basis set in DMSO solvent. The calculated chemical shift of TMZ-BITC(2) is shown in **Table 4.12**. The ^1H NMR of TMZ-BITC(2) in DMSO shows a chemical shift at 9.40 ppm and 8.49 ppm (deshield) for H34 and H16 of the two imidazole rings respectively. The two protons of NH_2 show chemical shifts at 7.34 ppm (H15) and 5.23 ppm (H14). The ^{13}C NMR calculations of the title show a chemical shift of 165.73

ppm(C18) and 164.49 ppm(C11) respectively for C=O groups. The lowest chemical shift is found for C29 at 48.85 ppm(CH₂). The chemical shift of aromatic carbons are calculated in the range of 115.58-145.30 ppm.

Table 4.12: Calculated chemical shifts of TMZ-BITC(2) calculated in GIAO method using DMSO as solvents.

¹ H NMR		¹³ C NMR	
Atom	Calculated(ppm)	Atom	Calculated(ppm)
34-H	9.40	18-C	165.73
16-H	8.49	11-C	164.49
33-H	8.21	20-C	147.24
35-H	7.82	31-C	145.74
36-H	7.81	22-C	145.30
37-H	7.76	4-C	142.76
15-H	7.34	8-C	140.26
39-H	5.76	9-C	139.34
38-H	5.75	23-C	139.17
14-H	5.23	25-C	135.43
		6-C	134.98
		27-C	132.51
		26-C	124.52
		28-C	115.58
		29-C	48.85

4.3.5 UV-vis analysis.

The Wavelengths (λ) and the excitation energies (E) are both expressed in nm, and oscillator strength (f) of TMZ evaluated by the TD-DFT method are shown in **Table 4.13** and **Figure 4.10** displays the plot of the ultraviolet spectra. A strong theoretical absorption peak is found at 332.03 nm with an oscillator strength of 0.0033 and excitation energy of 3.73 eV. This peak is the major contributor of the excitation from HOMO-5 to LUMO with 90% contribution. The peak observed at 345.08 nm with oscillator strength of 0 and excitation energy of 3.59 eV have the major contribution of 95 % from HOMO-1 to LUMO transition, and the peak

observed at 366.51 nm with oscillator strength of 0.0009 and excitation energy of 3.38 eV have the major contribution from HOMO to LUMO (98%).

Table 4.13: Electronics properties of TMZ-BITC(2) calculated using TD-DFT (B3LYP)/6-311++G(d,p)

Wavelength λ (nm)	Energy eV	Oscillator strength f	Symmetry	Major contributions
366.51	3.38	0.0009	Singlet-A	H→L (98%)
345.08	3.59	0.0	Singlet-A	H-1→L (95%)
332.03	3.73	0.0033	Singlet-A	H-5→L (90%), H-7→L (4%), H-1→L (2%)

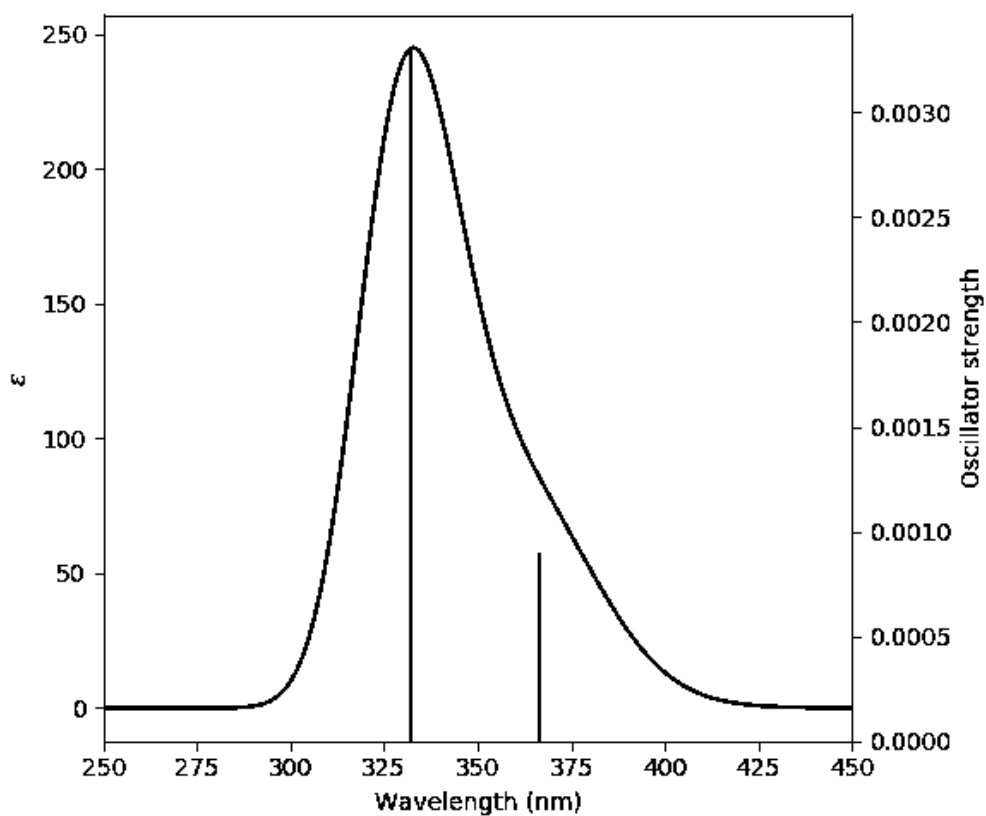


Figure 4.10: UV spectra of TMZ-BITC(2) calculated at B3LYP/6-311++G(d,p) basis set

4.3.6 Frontier Molecular Orbitals analysis (FMO)

The computation results indicate that the molecule has 712 molecular orbitals, where 105 are occupied, and the remaining are unoccupied molecular orbitals. Molecular orbitals 106 and 105 were identified as LUMO and HOMO molecular orbitals, respectively. The HOMO and LUMO orbitals with energy values are shown in **Figure 4.11**. HOMO is localized by π bonding type orbitals on BITC group and LUMO is localized by π^* bonding type orbitals on TMZ-BITC(2) molecule (**Figure 4.11**).

The LUMO and HOMO energies obtained are at -3.15 eV and -6.86 eV for the gas phase and -3.06 eV and -6.80 eV for the aqueous solution, respectively. The HOMO-LUMO energy gap (ΔE) in gas phase is 3.72 eV, and 3.74 eV for the aqueous solution. A slight increase in the energy gap is observed in the aqueous phase upon comparison in both the media.

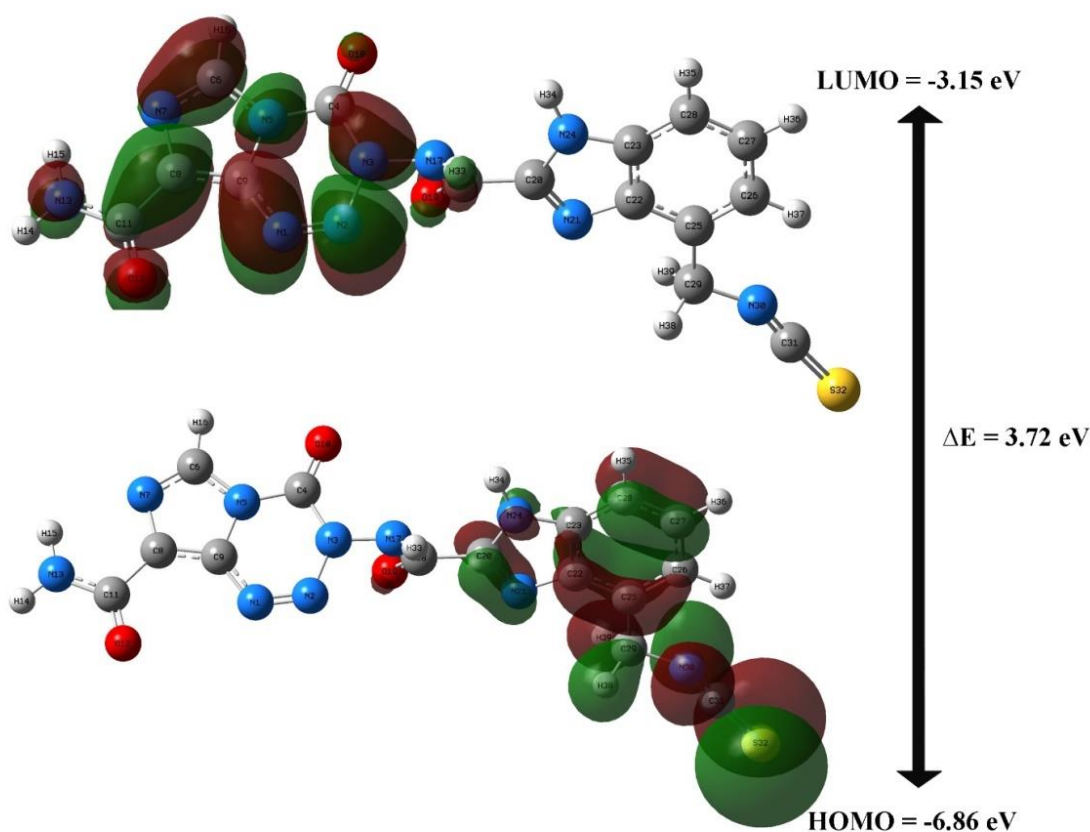


Figure 4.11: HOMO-LUMO graphical reproduction of TMZ-BITC(2)

Table 4.14: Frontier Molecular Orbitals energy parameters and global reactivity descriptors of TMZ-BITC(2).

FMOs	Gas	PCM
HOMO energy	-6.86	-6.80
LUMO energy	-3.15	-3.06
Energy gap (ΔE)	3.72	3.74
Ionization potential (I)	6.86	6.80
Electron affinity (A)	3.15	3.06
Hardness (η)	1.86	1.87
Chemical potential (μ)	-5.01	-4.93
Electronegativity (χ)	5.01	4.93
Electrophilicity (ω)	6.74	6.50

The tabulated FMO energy parameters and global reactivity descriptors of TMZ in both media are shown in **Table 4.14**. The electron affinity and electronegativity values of molecule shows a moderate acceptor properties as well as a high ability to pull electron density to itself. This could be attributed to the good number of N-atoms in the molecular structure with lone pairs of electrons donated for reactions. The high ionization potential of the molecule in both media indicates high reactivity of atoms and the molecule.

4.3.7 Natural bond orbital (NBO) analysis

The interactions occurring between localized Lewis orbitals and vacant non-Lewis orbitals are listed in **Table 4.15**. The results of the natural bondorbital analysis showed that the strongest intramolecular hyperconjugative interaction in the $\pi \rightarrow \pi^*$ occurs via overlapping between $\pi(\text{C}25\text{-C}26)$ bonding orbital participating as donor and the $\pi^*(\text{C}23\text{-C}26)$ as an acceptor antibonding orbital, which ensues massivestabilization energy of 25.68 kJ/mol. The $\pi \rightarrow \pi^*$ orbital overlap intramolecular interactions in the system occurs in the TMZ rings: $\pi(\text{C}6\text{-C}7) \rightarrow \pi^*(\text{C}8\text{-C}9)$, [21.99kJ/mol] and $\pi^*(\text{C}8\text{-C}9) \rightarrow \pi^*(\text{N}1\text{-N}2)$ [24.50 kJ/mol]. The highest π^*

antibonding orbitals conjugation with π^* antibonding orbitals is found to be $\pi^*(\text{C27-C28})$, $\pi^*(\text{C25-C26})$ with 197.14 kJ/mol.

Table 4.15: Second-order perturbation theory analysis of Fock matrix in NBO of TMZ-BITC(2).

Donor (i)	Acceptor (j)	E2 kJ/mol	E(j)-E(i) a.u.	F(i,j) a.u.
$\pi(\text{N1-N2})$	$\pi^*(\text{C8-C9})$	13.34	0.40	0.07
$\pi(\text{C6-N7})$	$\pi^*(\text{C8-C9})$	21.99	0.34	0.08
$\pi(\text{C8-C9})$	$\pi^*(\text{N1-N2})$	24.50	0.24	0.07
	$\pi^*(\text{C6-N7})$	17.34	0.27	0.06
	$\pi^*(\text{C11-O12})$	14.12	0.32	0.06
$\pi(\text{C20-N21})$	LP(1)C22	34.87	0.21	0.10
	$\pi^*(\text{C18-O19})$	10.84	0.35	0.06
$\pi(\text{C23-N24})$	$\pi^*(\text{C20-N21})$	25.68	0.36	0.09
$\pi(\text{C25-C26})$	LP(1)C22	46.23	0.14	0.09
	$\pi^*(\text{C27-C28})$	20.01	0.28	0.07
$\sigma(\text{C25-C29})$	$\sigma^*(\text{C31-S32})$	12.55	3.10	0.18
	$\pi^*(\text{C31-S32})$	21.06	5.13	0.31
$\sigma(\text{C27-C28})$	$\pi^*(\text{C23-N24})$	35.08	0.21	0.09
	$\pi^*(\text{C25-C26})$	16.19	0.30	0.06
$\sigma(\text{C29-N30})$	$\pi^*(3)\text{N30-C31}$	17.08	3.65	0.24
	$\pi^*(\text{C31-S32})$	18.64	5.29	0.30
$\sigma(\text{C29-H38})$	$\pi^*(\text{C31-S32})$	21.81	5.01	0.31
$\sigma(\text{C29-H39})$	$\pi^*(\text{C31-S32})$	53.79	5.00	0.49
$\sigma(\text{C31-S32})$	$\sigma^*(\text{N30-C31})$	13.33	1.41	0.13
	$\pi^*(3)\text{N30-C31}$	32.54	3.43	0.31
	$\pi^*(\text{C31-S32})$	27.21	5.08	0.34
	$\pi^*(3)\text{N30-C31}$	35.97	3.08	0.30
	$\sigma^*(\text{C31-S32})$	16.42	2.69	0.20
LP(1)N1	$\sigma^*(\text{N2-N3})$	19.06	0.63	0.10
LP(1)N3	$\pi^*(\text{N1-N2})$	32.00	0.26	0.08
	$\pi^*(\text{C4-O10})$	51.59	0.29	0.11
LP(1)N5	$\pi^*(\text{C4-O10})$	45.26	0.29	0.11
	$\pi^*(\text{C6-N7})$	41.46	0.29	0.10
	$\pi^*(\text{C8-C9})$	28.85	0.31	0.09
LP(2)O10	$\sigma^*(\text{N3-C4})$	29.50	0.65	0.13
	$\sigma^*(\text{C4-N5})$	28.91	0.64	0.12

LP(2)O12	$\sigma^*(\text{C8-C11})$	20.53	0.65	0.11
	$\sigma^*(\text{C11-N13})$	25.08	0.70	0.12
LP(1)N13	$\pi^*(\text{C11-O12})$	61.37	0.28	0.12
LP(1)N17	$\pi^*(\text{C18-O19})$	29.65	0.35	0.09
LP(2))19	$\sigma^*(\text{N17-C18})$	30.76	0.63	0.13
	$\sigma^*(\text{C18-C20})$	20.35	0.67	0.11
LP(1)S32	$\sigma^*(\text{N30-C31})$	18.86	1.54	0.15
	$\pi^*(\text{N30-C31})$	66.23	0.25	0.12
N1-N2)	$\pi^*(\text{C8-C9})$	44.45	0.05	0.08
$\pi^*(\text{C6-N7})$	$\pi^*(\text{C8-C9})$	78.18	0.02	0.06
$\pi^*(\text{C8-C9})$	$\pi^*(\text{C11-O12})$	84.01	0.03	0.08
$\pi^*(\text{C23-N24})$	$\pi^*(\text{C20-N21})$	30.87	0.05	0.05
	$\pi^*(\text{C27-C28})$	71.98	0.08	0.09
$\pi^*(\text{C27-C28})$	$\pi^*(\text{C25-C26})$	197.14	0.01	0.08

Note: where $E(2)$ = Energy of hyper conjunctive interactions; $E(j)-E(i)$ = Energy difference between the donor (i) and acceptor (j) NBO orbitals and $F(i,j)$ = Fock matrix element between i and j NBO orbital.

4.3.8 Vibrational Assignment

The TMZ-BITC(2) molecule with 39 atoms produces 111 normal modes of vibrations from the $3N-6$ relation, consisting of 38 stretching, 37 bending, and 36 torsional modes. There are 18 modes related to C-H bonds out of 111 normal modes. The 111 normal vibrational modes are assigned based on the detailed movement of individual atoms. The computed wavenumbers obtained are usually higher than the observed wavenumbers due to the combination of electron similarity effects and DFT basis set deficiencies. As a result, scaling factors are used to fit the experimental values, with a scaling factor of 0.958 for values greater than 1800 cm^{-1} and a scaling factor of 0.983 for values less than 1800 cm^{-1} . Only Potential energy distribution contributions (PED) $\geq 10\%$ were considered in the assignments of vibration modes. The calculated wavenumbers and assignments for TMZ-BITC(2) in gas phase by using the B3LYP/6-311++G(d,p) method are shown in **Table 4.16**. After that, a brief discussion of assignments by regions is presented at continuation.

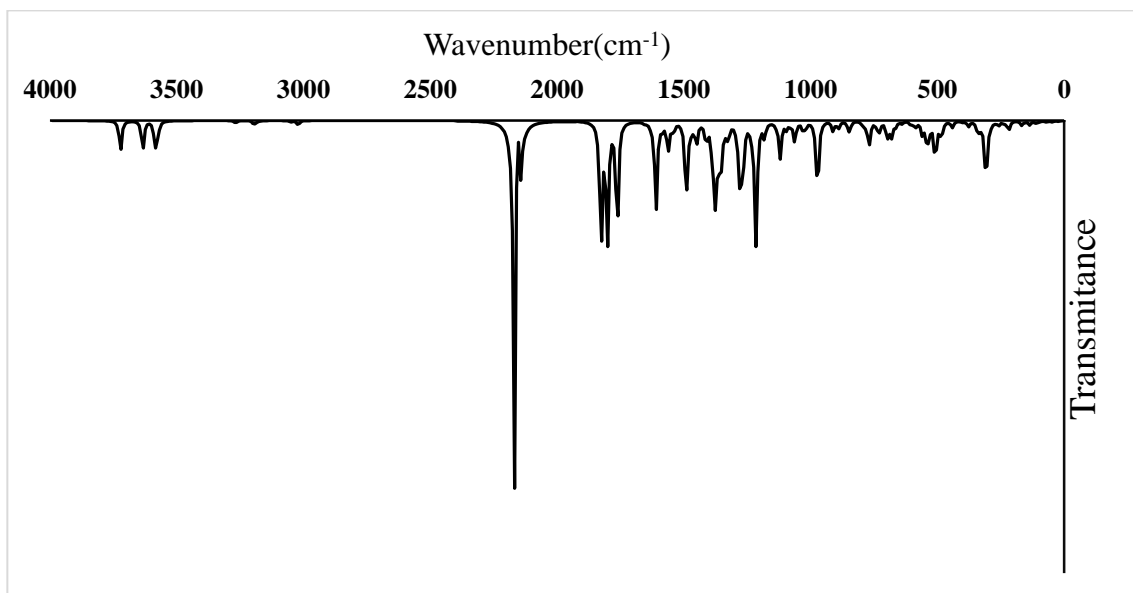


Figure 4.12: DFT FT-IR spectra of TMZ-BITC(2).

Assignments bands:

4000–2000 cm^{-1} region.

In this region, the stretching modes of N–H, C–H, N=C and CH₂ groups present in TMZ-BITC(2) are expected. The bands characteristics of NH groups are generally observed around 3500–3300 cm^{-1} . This absorption is strongly influenced by the chemical environment, in particular when NH groups are involved in the intramolecular or intermolecular hydrogen bond. In this case, the SQM calculations predict the N-H asymmetric and symmetric stretching modes of amide at 3565.55 and 3434.67 cm^{-1} . The N-H stretching mode has been calculated at 3423.83 and 3481.33. The C-H stretching mode has been calculated at 3130.80. Normally, in related compounds the C–H stretching vibrations of aromatic rings are assigned in the region 3200–3000 cm^{-1} . Normally, in related compounds the C–H stretching vibrations of aromatic rings are assigned in the region 3200–3000 cm^{-1} . For TMZ-BITC(2), the CH stretching modes of benzyl ring were predicted by calculations between 3063.61 and 3042.05 cm^{-1} . For TMZ-BITC(2), the CH stretching modes of benzyl ring were predicted by calculations between 3063.61 and 3042.05 cm^{-1} . The C–H stretching mode corresponding to CH₂ group is predicted by the SQM calculations at 2921.51 and 2894.10 cm^{-1} . The C–H stretching modes of cyclobutene calculated at

2921.51 and 3055.53 cm^{-1} respectively. The C-H asymmetric and symmetric stretching modes of cyclopentane ring at 2955.83-2916.16 and 2924.26 cm^{-1} . The N=C stretching modes of isothiocyanate group is predict at 2071.95 cm^{-1} .

2000–1000 cm^{-1} region.

The C=O, C=C, S=C, C–C, N=N and C–N stretching modes, deformation and rocking modes of NH, CH and CH₂ groups and, some deformations of the rings of TMZ-BITC(2) are characteristics of this region. In particular, the C=O stretching mode is usually assigned free of other vibrations (1800–1600 cm^{-1}). Here, the three C=O stretching mode is predicted by calculation at 1732.82, 1770.71 and 1795.33 cm^{-1} . The N=N stretching made of tetrazine ring calculated at 1526.39 and 1535.52 cm^{-1} . The C-N stretching modes of imidazole ring is calculated at 1389.21 and 1383.39 cm^{-1} . The C=C stretching modes at 1555.60. The benzyl ring in plane and out plane calculated at 1309.89 and 1301.23 cm^{-1} . CH₂ wagging at 1443.96 and rocking mode at 1495.04, and scissoring at 1443.96 cm^{-1} . C-H rocking modes of imidazole ring at 1466 cm^{-1} .

1000–0 cm^{-1} region:

In this region, the S-C stretching, C–H and N–H out-of-plane deformations, deformations, wagging and twisting modes of C=O group, deformations and torsions modes of rings of TMZ-BITC(2) are calculated. The out-of-plane of benzyl ring is calculated at 776.54-755.21 cm^{-1} , carboxamide at 688.91 cm^{-1} . The N-H of NH₂ group is calculated at 553.27 and 580.02 cm^{-1} . The out-of-plane of the whole molecule is calculated at 593.47-0 cm^{-1} .

Table 4.16: Vibrational assignments of TMZ-BITC(2) fundamental modes along with calculated IR and PED using the B3LYP method.

Mode	Calculated (cm ⁻¹)	Scaled (cm ⁻¹)	Intensity (kM/mol)	Characterization of normal modes with PED (%)
111	3721.87	3565.55	89.91	ν _a NH2 (99)
110	3633.95	3481.33	85.49	νN24-H34 (100)
109	3585.25	3434.67	70.69	ν _s NH2 (99)
108	3573.93	3423.83	36.90	νN17-H33 (100)
107	3268.06	3130.80	7.63	νC6-H16 (99)
106	3197.93	3063.61	6.62	νC26-H37 (56) νC27-H36 (30) νC28-H35 (14)
105	3189.44	3055.49	7.31	νC26-H37 (34) νC28-H35 (57)
104	3175.42	3042.05	1.05	νC27-H36 (62) νC28-H35 (28)
103	3049.59	2921.51	3.96	νCH2 (90)
102	3020.98	2894.10	13.77	νCH2 (95)
101	2162.79	2071.95	1855.07	νN30-C31 (83)
100	1826.38	1795.33	371.56	νO10-C4 (76)
99	1801.33	1770.71	352.17	νO19-C18 (77)
98	1762.79	1732.82	320.54	νO12-C11 (80)
97	1653.09	1624.99	4.87	νC26-C25 (24) νC28-C23 (21)
96	1628.82	1601.13	10.08	νC27-C28 (14) νC25-C22 (10) βC26C25C22 (14) βC22N21C20 (12)
95	1609.50	1582.14	265.38	βNH2 (51)
94	1584.58	1557.64	15.86	νC9-C8 (40) βNH2 (27)
93	1562.08	1535.52	85.95	νN2=N1 (15) νN21-C20 (24)
92	1552.79	1526.39	4.14	νN2 =N1 (49)
91	1540.44	1514.26	27.34	νC26-C25 (13) νC28-C23 (11) βH37C26C27 (13) βH36C27C26 (14)
90	1491.35	1466.00	193.66	νN7-C6 (32) βH16 C6 N7 (24)
89	1486.97	1461.70	45.67	νN2 =N1 (10) βH33N17C18 (55)
88	1468.93	1443.96	23.20	βH39-C29-H38 (86)

87	1450.42	1425.76	64.20	βH34N24C23 (11) βH36C27C26 (14) βH35C28C27 (27)
86	1413.23	1389.21	10.98	υN7-C6 (11) υN5-C6 (20) υN5-C4 (19)
85	1411.70	1387.70	44.55	βH34-N24-C23 (14)
84	1386.53	1362.96	99.19	υN21-C20 (10) υN24-C20 (19) βC22N21C20 (11)
83	1375.30	1351.92	209.00	υN13-C11 (10) υN1-C9 (19) υC11-C8 (11) βC9C8N7 (12)
82	1362.84	1339.67	98.86	τH38C29N30C31 (16) τH39C29N30C31 (30)
81	1351.52	1328.54	101.65	υN17-N3 (30) βN5C6N7 (11)
80	1331.40	1308.76	25.24	υN7-C6 (12) βC9C8N7 (12) βC8N7C6 (10)
79	1323.73	1301.23	31.75	υC27-C28 (17) υN24-C23 (30) βC23N24C20 (15)
78	1288.77	1266.86	30.45	υC26-C25 (15) υN21-C22 (10) βH37C26C27 (39)
77	1276.73	1255.02	215.81	υN13-C11 (10) υN7-C8 (34) υN5-C4 (10) βN5C6N7 (14)
76	1265.27	1243.76	87.62	υN21-C22 (27) βC25C22N21 (10)
75	1256.88	1235.51	0.22	βH38C29N30 (78) τH39C29N30C31 (14)
74	1233.71	1212.73	27.07	υN7 C6 (14) υN1 C9 (11) υN5 C6 (10) βH16 C6 N7 (23)
73	1215.59	1194.92	353.26	υC20-C18 (10) βH34N24C23 (25) βH36C27C26 (10)
72	1206.95	1186.43	4.15	υN7 C8 (14) βH16 C6 N7 (21)
71	1181.95	1161.86	43.51	βH36C27C26 (19) βH35C28C27 (21)
70	1136.25	1116.94	8.25	υN30-C29 (70)
69	1119.90	1100.86	105.23	υN24-C20 (12) υN17-C18 (20)
68	1095.26	1076.64	21.12	υN13-C11 (12) βH15N13C11 (51)
67	1077.89	1059.57	8.65	βH35C28C27 (13) βC28C23C22 (13)
66	1062.19	1044.13	60.38	υN3 C4 (12)
65	1030.58	1013.06	20.14	υN24-C23 (13) υN30-C29 (13) υC29-C25 (20) βC26C25C22 (12)
64	1020.24	1002.90	20.65	υN3 C4 (27) βN1C9C8 (12)
63	988.61	971.80	0.69	τH37C26C27C28 (24) τH36C27C28C23 (22) τH38C29N30C31 (14)
62	987.59	970.80	3.55	υN24C20 (27) υN17C18 (19)
61	972.29	955.76	214.84	βO10C4N3 (14) βN2N1C9 (15) βC8N7C6 (14)
60	971.07	954.56	0.55	τH36C27C28C23 (29) τH38C29N30C31 (18)

59	911.18	895.69	27.66	β O19C18N17 (13) β N2 N1 C9 (15) β C18N17 N3 (16)
58	896.50	881.25	0.77	τ H37C26C27C28 (47) τ H35C28C27C26 (36)
57	889.90	874.77	21.52	β C27C28C23 (14) β N2N1C9 (11)
56	849.71	835.27	27.82	β C27C28C23 (12) β O19C18N17 (12) β N2N1C9 (13)
55	842.75	828.43	8.34	τ H16C6N7 C8 (83) τ C8N7C6N5 (12)
54	797.77	784.20	3.30	τ C9C8N7C6 (15) γ O12N13 C8C11 (55) γ C11C9N7C8 (18)
53	789.97	776.54	8.93	τ C26C25C22C23 (15) τ C22N21C20N24 (17) γ C25C23N21C22 (13)
52	780.23	766.96	1.28	τ C22N21C20N24 (17)
51	778.56	765.32	16.49	γ O19N17C20C18 (47)
50	768.27	755.21	62.02	ν N30-C29 (29) β N30C29C25 (22)
49	739.01	726.44	14.52	τ H37C26C27C28 (14) τ H36C27C28C23 (26) τ H35C28C27C26 (38)
48	729.13	716.73	28.47	γ O10 N5 N3 C4 (68)
47	700.82	688.91	13.34	ν C28-C23 (10) ν C29-C25 (11) ν N30C29 (11) γ O10N5N3C4 (16)
46	697.56	685.70	22.49	β C9C8N7 (12)
45	692.93	681.15	19.38	τ N2N1C9 N5 (25) τ C9C8N7C6 (19) γ N1N5C8C9 (12)
44	680.42	668.85	42.66	τ C9C8N7C6 (19)
43	664.18	652.89	13.97	β C23N24C20 (18)
42	639.94	629.06	6.88	τ C9C8N7C6 (10) τ C8N7C6N5 (51)
41	603.73	593.47	10.63	ν C28C23 (18) ν C25C22 (15) β C23N24C20 (18) β C22N21C20 (11)
40	588.02	578.03	7.63	β N2 N1 C9 (11)
39	586.18	576.22	8.40	β O12C11N13 (13) β N1C9C8 (19)
38	582.87	572.96	2.64	τ H14N13C11 C8 (34) τ H15N13C11 C8 (35)
37	559.47	549.96	35.60	τ C26C25C22C23 (10) τ C27C28C23N24 (27) γ C25C23N21C22 (13)
36	543.28	534.04	32.99	β C28C23C22 (16)
35	542.67	533.44	10.06	β C4N5C9 (16) τ H34N24C23C22 (15)
34	534.14	525.06	43.72	τ N2N1C9N5 (13) τ N3C4N5C6 (11) γ N1N5C8C9 (13)
33	512.54	503.83	7.12	τ H34N24C23C22 (39)
32	508.11	499.48	107.50	γ C29C22C26C25 (14) γ C25C23N21C22 (10) γ C28N24C22C23 (12)

31	488.99	480.68	27.62	β N3C4N5 (19)
30	479.56	471.41	22.14	β S32C31N30 (61)
29	453.59	445.88	0.47	β S32C31N30 (19)
28	440.76	433.26	18.14	τ S32C31N30C29 (95)
27	401.91	395.07	2.55	β O10C4N3 (12) τ H33N17C18C20 (21)
26	377.48	371.06	15.60	β C20C18N17 (19)
25	343.52	337.68	16.91	β O10C4N3 (13) β N17N3C4 (19) τ H33N17C18C20 (16)
24	333.17	327.51	26.94	β N13C11 C8 (28) β C18N17N3 (11)
23	309.17	303.91	45.48	β O19C18N17 (18) β C18N17N3 (18) τ H33N17C18C20 (11)
22	307.74	302.51	140.13	β O10C4N3 (19) τ H14N13C11C8 (10) τ H15N13C11C8 (10)
21	292.54	287.57	11.68	τ H14N13C11C8 (32) τ H15N13C11C8 (32)
20	275.74	271.05	2.22	γ N24C18N21C20 (12)
19	257.99	253.60	11.63	γ C28N24C22C23 (26) γ N24C18N21C20 (19)
18	235.62	231.62	7.18	τ C23N24C20C18 (16) γ C25C23N21C22 (11) γ N24C18N21C20 (11)
17	221.87	218.10	1.41	τ N2N1C9N5 (11) τ N3C4N5C6 (10) γ N1N5C8C9 (48)
16	218.13	214.42	25.94	β N30C29C25 (22) γ C11C9N7C8 (15) γ C4C6C9N5 (14)
15	168.05	165.19	12.48	β N30C29C25 (18) γ C11C9N7C8 (20) γ C4C6C9N5 (17)
14	156.53	153.87	3.14	τ C26C25C22C23 (32) γ C29C22C26C25 (43)
13	135.64	133.34	11.66	β C20C18N17 (11) β C11C8N7 (27)
12	113.05	111.13	5.92	β C11C8N7 (16) β C29C25C26 (17) τ N3C4N5C6 (13)
11	103.08	101.33	2.97	β N21C20C18 (14) β C11C8N7 (14) τ C23N24C20C18 (11)
10	94.00	92.41	1.22	τ N3C4N5C6 (34)
9	74.86	73.58	1.71	τ N17N3C4N5 (22) γ C11C9N7C8 (17) γ C4C6C9N5 (12)
8	67.20	66.06	3.00	τ N30C29C25C22 (24)
7	60.30	59.28	0.04	τ C31N30C29C25 (11) τ N21C20C18N17 (13) τ N30C29C25C22 (23)
6	46.90	46.11	3.33	τ N21C20C18N17 (12) τ C18N17N3C4 (31) τ N30C29C25C22 (16)
5	35.81	35.20	0.41	τ N13C11C8C9 (70)
4	25.23	24.80	0.97	β C31N30C29 (57)

3	21.15	20.79	89.91	τ C31N30C29C25 (22) τ N21C20C18N17 (25) τ C18N17 N3 C4 (26)
2	15.48	15.22	85.49	τ N17N3C4N5 (26) τ C20C18N17N3 (30) γ C4C6C9N5 (14)
1	11.55	11.35	70.69	τ N17N3C4N5 (16) τ C20C18N17N3 (28)

Symbol for stretching here: stretching (a = antisymmetric; s = symmetric); β = deformation in the plane; γ = deformation out of the plane; τ = torsion; β R = deformation ring; τ R= torsion ring; τ w= twisting; δ = deformation; and R = Ring

4.4 TMZ-BITC(3)

4.4.1 Optimization and properties in both media:

TMZ-BITC(3) was optimized at DFT/B3LYP/6-311++G(d,p) level of theory in both the gas and the aqueous phases as depicted in **Table 4.17**. Furthermore, frequency calculations were performed at the same level of theory to ensure that the optimized structure corresponds to true energetic minima. Results of optimizations of TMZ-BITC(3) in the gas phase and aqueous solution can be seen in **Figure 4.13**. The difference between the value optimized in the aqueous solution and the corresponding gas phase ($-1744.25 + 1744.27 = 0.02$, Hartrees = 63.80 kJ/mol) was used to calculate the relative energy. It can be seen that the calculated total energies (E) in both phases, as well as the corrected ZPVE energy (EZPVE), were primarily negative. The differences in dipole moments (μ) from 3.02 D in the gas phase to 5.89 D in the aqueous solution imply that an ionic bond is more prominent in the predicted solution with increased polarity. Increase or expansion of volume can be seen in aqueous solution from 420.5 A³ to 424.4 A³.

Table 4.17: Calculated total energies (E), dipole moments (μ), and volumes (V) for compound TMZ-BITC(3) in gas and aqueous phase phases by using B3LYP/6-31++G(d,p) basis set.

Medium	E (Hartrees)	E _{ZPVE} (Hartrees)	μ (D)	V(A ³)
Gas phase	-1743.8654	-1744.247	3.02	420.5
Aqueous phase	-1743.8901	-1744.2713	5.89	424.4

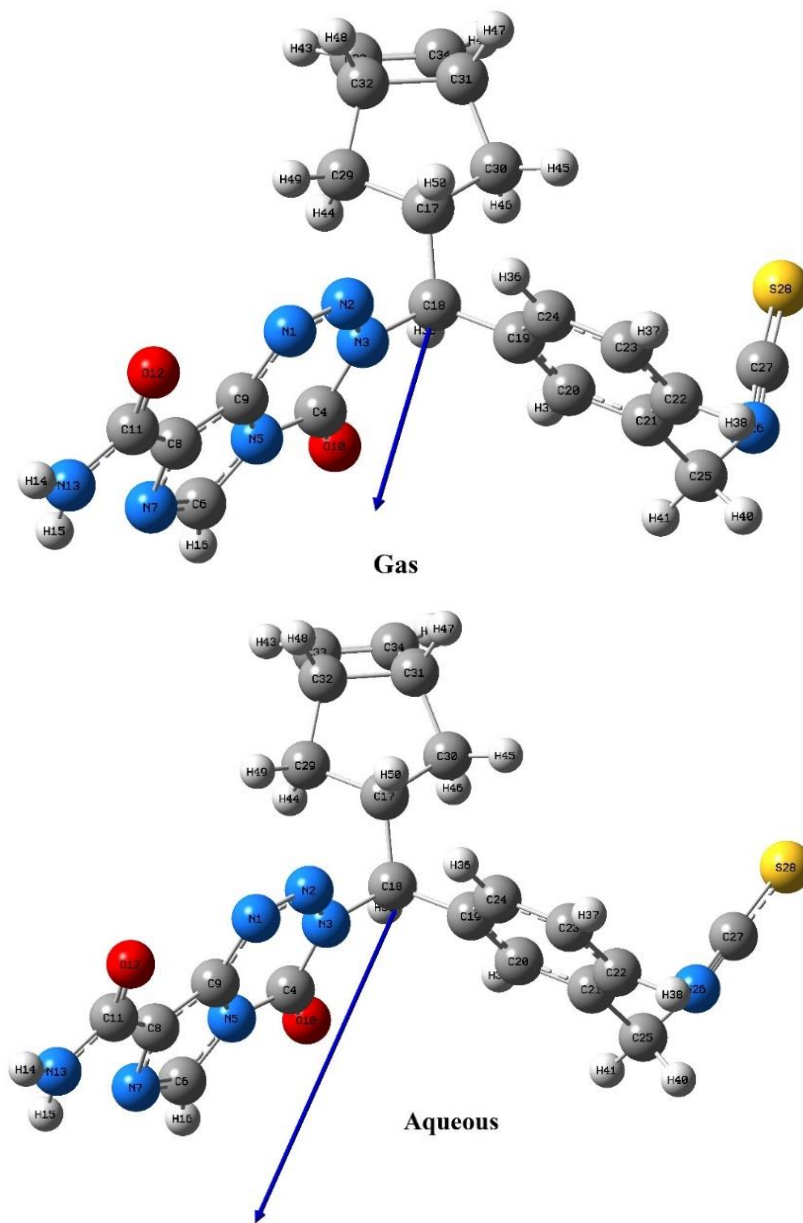


Figure 4.13: Optimized structure of TMZ-BITC(3) at B3LYP/6-311++G(d,p) basis set for gas phase (upper) aqueous solution (bottom).

4.4.2 Geometrical parameters

The optimized structure of TMZ-BITC(3) possess C_1 point group symmetry. The optimized geometrical parameters of TMZ-BITC(3) in gas phase and aqueous solution by using the B3LYP/ 6-311++G(d,p) method are presented in **Table 4.18**. The N=N and N-N bond length in the tetrazine ring is found to be 1.26 Å and 1.39 Å

in gas (1.27 Å and 1.38 Å in aqueous) respectively. The C=O bond length is found to be 1.21 Å. The C-N bond length in the isothiocyanate group is 1.19 Å in gas and 1.18 Å in aqueous. The C-C bond lengths in the benzyl ring are in the range of 1.39 Å to 1.4 Å. The only C=S bond length of the molecule in the Isocyanate group is found to be 1.59 Å. The C-C and C=C bond length in the cyclobutene ring are 1.52 Å and 1.34 Å respectively and the C-C bond lengths in the cyclopentane ring is found to be 1.54 Å to 1.58 Å.

The bond angle N-N-N in the tetrazine ring is calculated at 120.7°. The C-C-C bond angles in the benzyl ring are in the range of 120.12° to 120.62° which depicts the hexagonal shape of a benzene ring. The dihedral angles found for the molecules shows the planarity in the TMZ and benzyl rings.

Table 4.18: Selected geometrical parameters of TMZ-BITC(3) using B3LYP/6-311++G(d,p) basis set.

Bondlengths(Å)		
Parameters	Gas	Aqueous
N1-N2	1.26	1.27
N1-C9	1.37	1.36
N2-N3	1.39	1.38
N3-C4	1.39	1.39
N3-C18	1.49	1.50
C4-O10	1.21	1.21
N5-C6	1.37	1.37
N7-C8	1.37	1.37
C8-C9	1.39	1.39
C8-C11	1.49	1.49
C17-C30	1.55	1.55
C20-C21	1.40	1.40
C22-C23	1.39	1.39
C23-C24	1.39	1.39
C25-N26	1.44	1.44
N26-C27	1.19	1.18
C27-S28	1.59	1.61
C31-C32	1.58	1.58
C32-C33	1.52	1.52
C33-C34	1.34	1.34

Bondangles(°)		
Parameters	Gas	Aqueous
N2-N1-C9	119.41	119.35
N1-N2-N3	120.70	120.89
N2-N3-C4	126.15	125.92
N3-C4-N5	110.47	110.80
C4-N5-C9	122.45	122.27
C9-C8-C11	128.86	128.95
C8-C11-N13	113.16	113.92
C29-C17-C30	104.18	104.13
C20-C21-C25	120.20	120.13
C22-C21-C25	120.62	120.47
C21-C22-C23	120.12	119.97
C22-C23-C24	120.35	120.33
C19-C24-C23	120.23	120.31
C29-C32-C31	106.16	106.16
C29-C32-C33	119.35	119.32
C31-C32-C33	85.41	85.44
Dihedral angles(ϕ)		
Parameters	Gas	Aqueous
N2-N1-C9-N5	0.50	0.21
N1-N2-N3-C4	-1.76	-1.44
N1-N2-N3-C18	-178.04	-177.65
N3-C4-N5-C6	179.21	179.29
C4-N5-C9-N1	0.11	0.44
C4-N5-C9-C8	-0.11	-0.08
C11-C8-C9-N5	-179.97	-179.99
C9-C8-C11-O12	0.18	-0.17
C24-C19-C20-C21	-0.46	-0.17
C20-C19-C24-C23	0.05	-0.23
C19-C20-C21-C22	0.51	0.44
C20-C21-C22-C23	-0.13	-0.32
C30-C31-C32-C29	0.14	0.05
C30-C31-C34-C33	106.00	106.03
C32-C31-C34-C33	-0.04	-0.01
C29-C32-C33-C34	-106.02	-106.00
C31-C32-C33-C34	-0.04	-0.01

4.4.3 Atomic charges and MEP

The atomic charges and molecular electrostatic potentials (MEP) charges of the optimized structures of TMZ-BITC(3) for the gas phase and the aqueous solution are summarized in Error! Reference source not found.. The trends in the Mulliken and NPA charges on N-atoms are different, some N-atoms are positive in Mulliken, negative in NPA and vice versa. Most of the N-atoms shows negative values in NPA but in Mulliken most shows positive values. Both in Mulliken and NPA, O-atoms shows negative values, O-atoms in NPA shows more negative values than Mulliken. Certain C atoms values in both the Mulliken and NPA shows opposite charge. C4 is the most positive and C30 is the most negative in NPA while C19 is the most positive and C18 is the most negative in Mulliken charges.

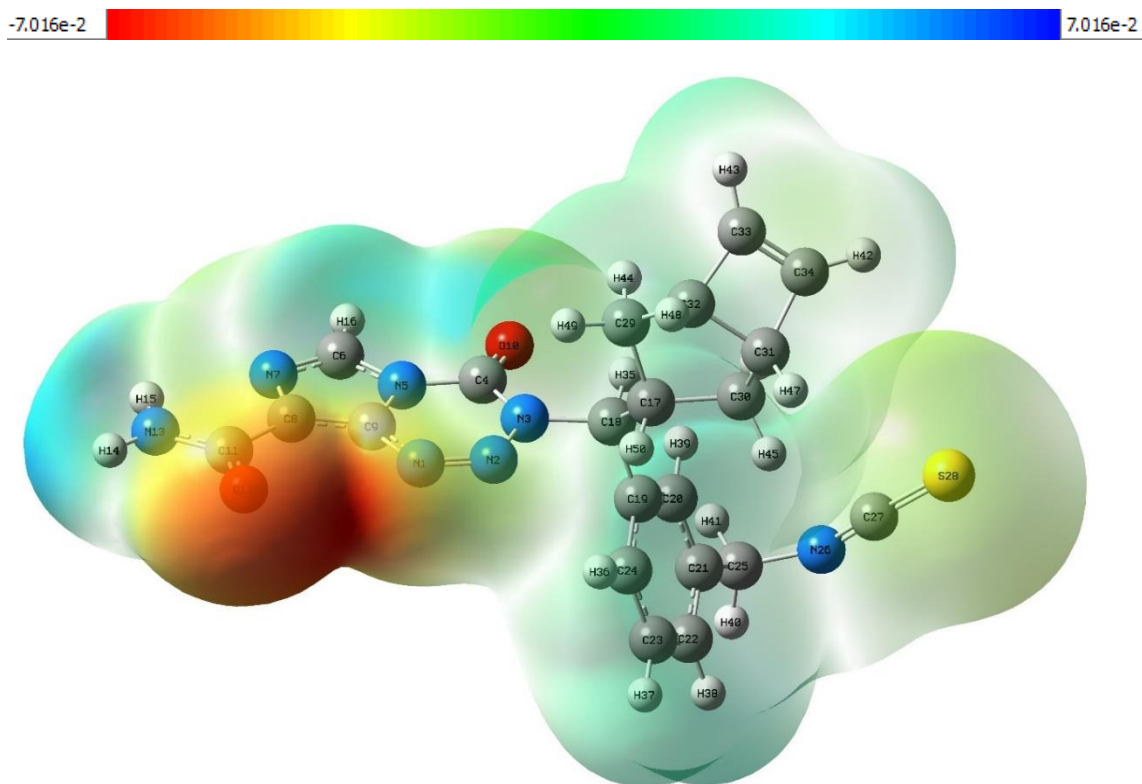


Figure 4.14: Calculated electrostatic potential surfaces on the molecular surface of TMZ-BITC(2) in the gas phase, using 6-311++G(d,p) basis set.

The molecular electrostatic potentials (MEP) charges are also presented in Error! Reference source not found.. The same trends of values are observed in both media and the relative expected tendency is observed as MEP O-atoms > MEP N-atoms. The MEP of TMZ-BITC(3) molecule shows the negative potential region around oxygen atom of O12 and most positive region localized on H of amine group and C6 of imidazole ring indicating a possible site for electrophilic attack and nucleophilic region, respectively(**Figure 4.14**).

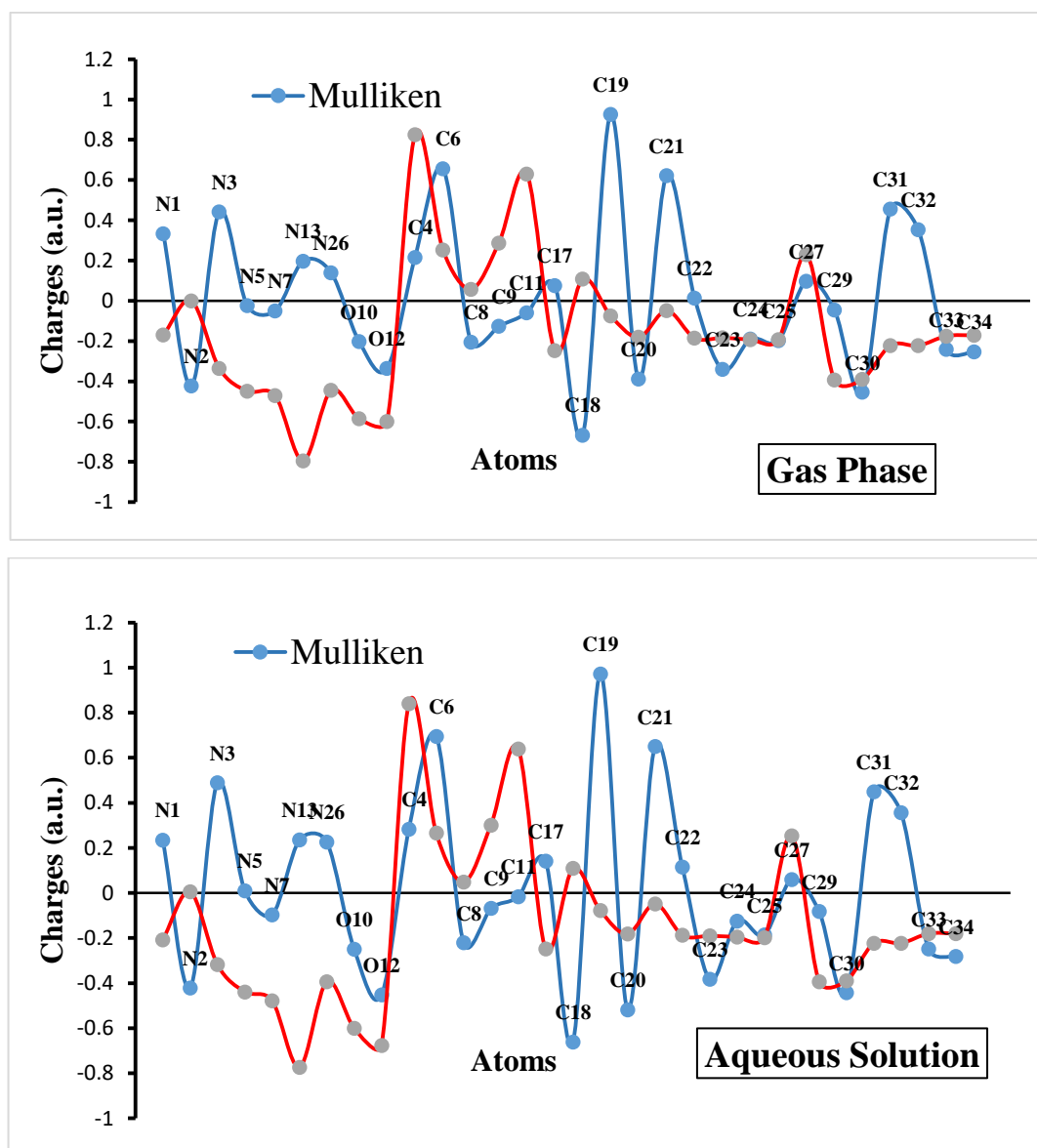


Figure 4.15: Graph showing the trends for Mulliken and Natural Population Analysis (NPA) Atomic charges of TMZ-BITC(3) in the gas phase (upper) and the aqueous solution (bottom).

Table 4.19: Mulliken, Natural Population Analysis (NPA) charges (in a.u.) and Molecular Electrostatic Potentials (MEP) of TMZ-BITC(3) in the gas phase and aqueous phase calculated at B3LYP/6-311++G(d,p) level of theory.

Atoms	Gas Phase			Aqueous Phase		
	Mulliken	NPA	MEP	Mulliken	NPA	MEP
N1	0.33	-0.17	-18.33	0.24	-0.21	-18.34
N2	-0.42	0.00	-18.29	-0.42	0.01	-18.29
N3	0.44	-0.34	-18.28	0.49	-0.32	-18.27
C4	0.22	0.83	-14.58	0.28	0.84	-14.57
N5	-0.02	-0.45	-18.28	0.01	-0.44	-18.27
C6	0.66	0.25	-14.67	0.70	0.27	-14.66
N7	-0.05	-0.47	-18.37	-0.10	-0.48	-18.37
C8	-0.21	0.06	-14.71	-0.22	0.05	-14.71
C9	-0.13	0.29	-14.67	-0.07	0.30	-14.67
O10	-0.20	-0.59	-22.35	-0.25	-0.60	-22.34
C11	-0.06	0.63	-14.66	-0.02	0.64	-14.66
O12	-0.34	-0.60	-22.40	-0.45	-0.68	-22.43
N13	0.20	-0.80	-18.37	0.24	-0.77	-18.36
C17	0.08	-0.25	-14.75	0.14	-0.25	-14.74
C18	-0.67	0.11	-14.70	-0.66	0.11	-14.69
C19	0.93	-0.08	-14.74	0.97	-0.08	-14.74
C20	-0.39	-0.18	-14.75	-0.52	-0.18	-14.74
C21	0.62	-0.05	-14.74	0.65	-0.05	-14.73
C22	0.01	-0.19	-14.75	0.12	-0.19	-14.75
C23	-0.34	-0.18	-14.75	-0.38	-0.19	-14.75
C24	-0.19	-0.19	-14.76	-0.12	-0.20	-14.75
C25	-0.20	-0.19	-14.69	-0.19	-0.20	-14.67
N26	0.14	-0.45	-18.36	0.23	-0.39	-18.34
C27	0.10	0.23	-14.68	0.06	0.25	-14.68
S28	-0.33	-0.04	-59.25	-0.47	-0.15	-59.27
C29	-0.05	-0.39	-14.77	-0.08	-0.39	-14.76
C30	-0.45	-0.39	-14.77	-0.44	-0.39	-14.77
C31	0.46	-0.22	-14.76	0.45	-0.22	-14.76
C32	0.35	-0.22	-14.76	0.36	-0.22	-14.76
C33	-0.24	-0.18	-14.77	-0.25	-0.18	-14.78
C34	-0.25	-0.17	-14.77	-0.28	-0.18	-14.78

4.4.4 ^1H and ^{13}C NMR analysis

The ^1H and ^{13}C NMR calculations were performed by GIAO (Gauge-Independent Atomic Orbital) method at the B3LYP/6-311++G(d,p) basis set in DMSO solvent. The calculated chemical shift of TMZ-BITC(3) is shown in **Table 4.20**. The ^1H NMR of TMZ-BITC(3) in DMSO shows a chemical shift at 8.25ppm(deshield) for H16 of imidazole ring. The aromatic protons are calculated at thr range 8.16-7.61 ppm. The two proton of NH_2 shows chemical shifts at 7.24 ppm(H15) and 5.10 ppm(H14). The ^{13}C NMR calculations of the title shows a chemical shift of 165.06 ppm(C11) of carboxamide group. The lowest chemical shift of 35.17ppm and 35.65 ppm found for C30 and C29(CH_2) of cyclopentene ring. The chemical shift of aromatic carbons are calculated in the range of 132.81-146.95ppm.

Table 4.20: Calculated chemical shifts of TMZ-BITC(3) in GIAO method using DMSO as solvents.

^1H NMR		^{13}C NMR	
Atom	Calculated(ppm)	Atom	Calculated(ppm)
16-H	8.25	11-C	165.06
36-H	8.16	34-C	151.58
39-H	7.82	33-C	151.40
37-H	7.71	19-C	146.95
38-H	7.61	27-C	144.93
15-H	7.24	4-C	143.55
42-H	6.67	21-C	142.95
43-H	6.67	9-C	139.71
35-H	5.72	8-C	137.08
14-H	5.10	20-C	136.44
41-H	4.77	22-C	134.99
40-H	3.92	23-C	134.90
50-H	3.90	24-C	132.81
48-H	3.41	6-C	132.77
47-H	3.38	18-C	71.11
49-H	1.72	17-C	59.45
45-H	1.36	32-C	52.70
46-H	1.23	31-C	52.66
44-H	1.19	25-C	51.37
		30-C	35.65
		29-C	35.17

4.4.5 UV-vis analysis

The Wavelengths (λ) and the excitation energies (E) are both expressed in nm, and oscillator strength (f) of TMZ-BITC(3) evaluated by the TD-DFT method are shown in **Table 4.21** and displays of the ultraviolet spectra plot in **Figure 4.16**. A strong theoretical absorption peak is found at 327.84 nm with an oscillator strength of 0.00959 and excitation energy of 3.78 eV. This peak is the major contribution of the excitation from HOMO-2 to LUMO with 42%. The peak observed at 338.23 nm with oscillator strength of 0.0277 and excitation energy of 3.67 eV have the major contribution of 98% from HOMO to LUMO transition, and the peak observed at 322.4 nm with oscillator strength of 0.0707 and excitation energy of 3.85 eV have the major contribution from HOMO-6 to LUMO (56%). Both of these peaks relate to the $\pi \rightarrow \pi^*$ transitions.

Table 4.21: Electronics properties of TMZ-BITC(3) calculated using TD-DFT (B3LYP)/6-311++G(d,p)

Wavelength λ (nm)	Energy eV	Oscillator strength f	Symmetry	Major contributions
338.23	3.67	0.0277	Singlet-A	HOMO \rightarrow LUMO (98%)
327.84	3.78	0.00959	Singlet-A	H-2 \rightarrow LUMO (42%)
322.40	3.85	0.0707	Singlet-A	H-6 \rightarrow LUMO (56%)

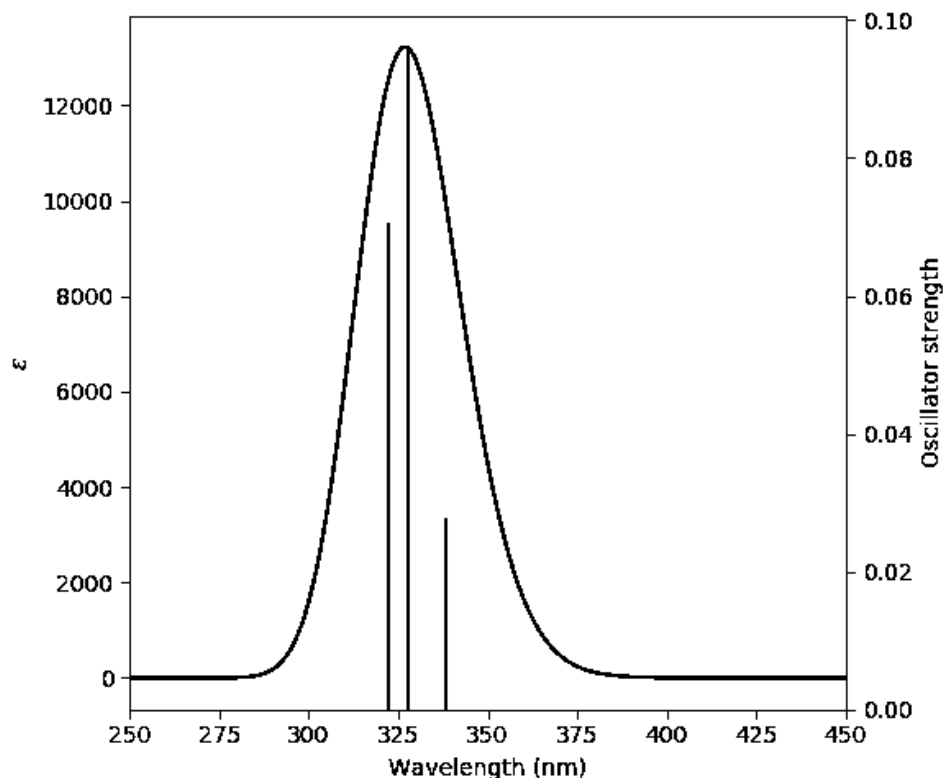


Figure 4.16: UV spectra of TMZ-BITC(3) calculated at B3LYP/6-311++G(d,p).

4.4.6 Frontier Molecular Orbitals analysis (FMO)

The computation results indicate that the molecule has 819 molecular orbitals, where 113 are occupied, and the remaining are unoccupied molecular orbitals. Molecular orbitals 114 and 113 are identified as LUMO and HOMO molecular orbitals, respectively. The HOMO and LUMO orbitals with energy values are shown in **Table 4.22**. HOMO is localized by π bonding type orbitals on isothiocyanate group and LUMO is localized by π^* bonding type orbitals on TMZ-BITC(3) molecule (**Figure 4.17**).

The LUMO and HOMO energies obtained are at -2.83 eV and -6.89 eV for the gas phase and -2.82 eV and -6.87 eV for the aqueous phase, respectively. The HOMO-LUMO energy gap (ΔE) in gas phase is 4.07 eV, and for the aqueous phase it is 4.05 eV. A slight decrease in the energy gap is observed for the aqueous phase.

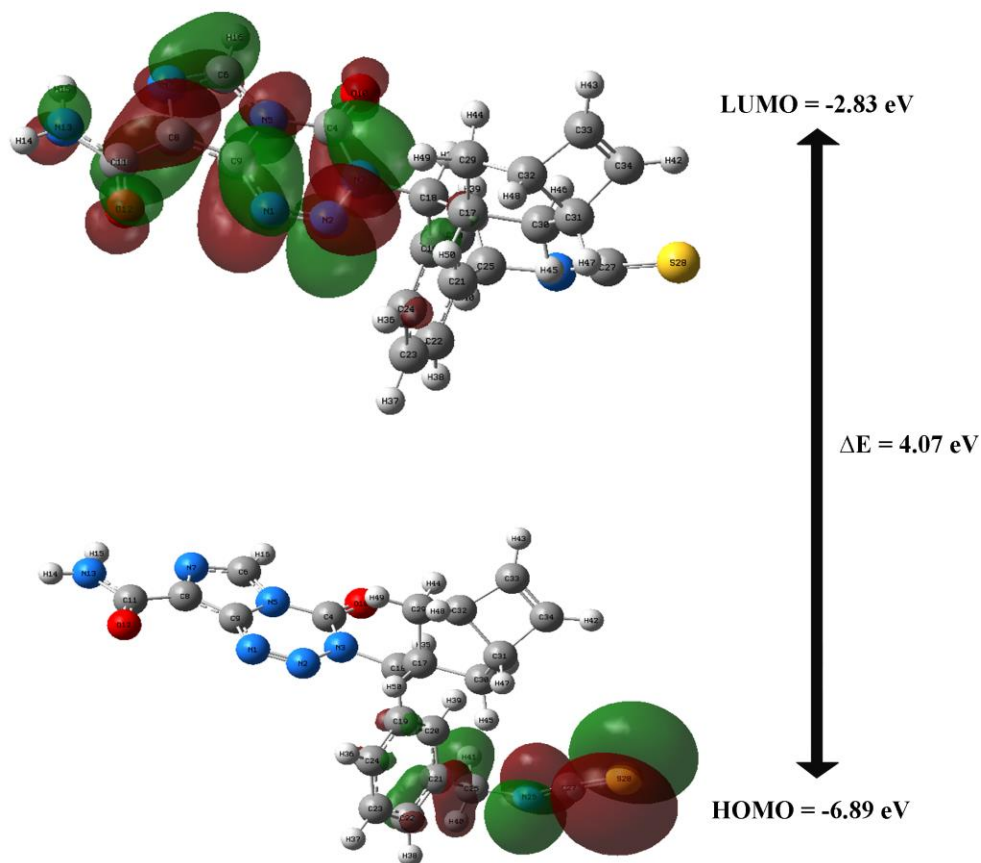


Figure 4.17: HOMO-LUMO graphical reproduction of TMZ-BITC(3)

Table 4.22: Frontier Molecular Orbitals energy parameters and global reactivity descriptors of TMZ-BITC(3)

FMOs	Gas	PCM
HOMO energy	-6.89	-6.87
LUMO energy	-2.83	-2.82
Energy gap (ΔE)	4.07	4.05
Ionization potential (I)	6.89	6.87
Electron affinity (A)	2.83	2.82
Hardness (η)	2.03	2.02
Chemical potential (μ)	-4.86	-4.85
Electronegativity (χ)	4.86	4.85
Electrophilicity (ω)	5.81	5.80

The tabulated FMO energy parameters and global reactivity descriptors of TMZ in both media are shown in Table 4.22. The electron affinity and electronegativity values of molecule shows a moderate acceptor properties as well as a high ability to pull electron density to itself. This could be attributed to the good number of N-atoms in the molecular structure with lone pairs of electrons donated for reactions. The high ionization potential of the molecule in both media indicates high reactivity of atoms and the molecule.

4.4.7 Natural bond orbital (NBO) analysis

The interactions occurring between localized Lewis orbitals and vacant non-Lewis orbitals are listed in Table 4.23. The results of the natural bond orbital analysis showed that the strongest intramolecular hyperconjugative interaction in the $\pi \rightarrow \pi^*$ occurs via overlapping between $\pi(\text{C8-N9})$ bonding orbital participating as donor and the $\pi^*(\text{N1-N2})$ as an acceptor antibonding orbital, which ensues a stabilization energy of 22.79 kJ/mol.

The other significant $\pi \rightarrow \pi^*$ interactions also occurs in the benzyl ring. Of all the interaction, those involving lone-pair LP(1) of nitrogen, LP(1) and LP(2) of oxygen towards the π^* are mostly higher than the other types of interaction. The lone-pair LP(1) N3 shows highest stabilizing energy of 57.33 kJ/mol with antibonding $\pi^*(\text{C4-O10})$. The LP(2) O10 also shows highest stabilizing energy of 26.35 kJ/mol with $\sigma^*(\text{C4-N5})$ among the LP to σ^* interactions. The lone-pair LP(2) S28 also occurs towards $\pi^*(\text{N26-C27})$ with stabilizing energy of 60.58 kJ/mol. The appreciable highest interaction energies $\pi^* \rightarrow \pi^*$ orbital overlap intramolecular interactions in the system occurs in the rings, $\pi^*(\text{C6-C7}) \rightarrow \pi^*(\text{C8-C9})$ with stabilizing energy of 92.37 kJ/mol and $\pi^*(\text{N1-N2}) \rightarrow \pi^*(\text{C8-C9})$ with stabilizing energy of 43.97 kJ/mol.

Table 4.23: Second-order perturbation theory analysis of Fock matrix in NBO of TMZ-BITC(3).

Donor (i)	Acceptor (j)	E2 kJ/mol	E(j)-E(i) a.u.	F(i,j) a.u.
π (N1-N2)	π^* (C8-C9)	14.72	0.40	0.07
π (C6-N7)	π^* (C8-C9)	20.92	0.33	0.08
π (C8-C9)	π^* (N1-N2)	22.79	0.23	0.07
	π^* (C6-N7)	17.69	0.27	0.06
	π^* (C11-O12)	16.86	0.30	0.07
σ (C17-C18)	σ^* (C34-H42)	26.56	5.72	0.35
σ (C17-C29)	σ^* (C34-H42)	28.71	5.69	0.36
σ (C17-C30)	π^* (C33-C34)	12.59	2.88	0.17
	σ^* (C33-H43)	16.36	3.19	0.20
	σ^* (C34-H42)	52.61	5.59	0.49
π (C19-C20)	π^* (C21-C22)	20.66	0.29	0.07
	π^* (C23-C24)	19.92	0.29	0.07
π (C21-C22)	π^* (C19-C20)	20.67	0.29	0.07
	π^* (C23-C24)	19.31	0.29	0.07
π (C23-C24)	π^* (C19-C20)	20.98	0.29	0.07
	π^* (C21-C22)	21.21	0.28	0.07
LP(1)N1	σ^* (N2-N3)	16.39	0.71	0.10
	σ^* (N5-C9)	11.14	0.79	0.09
LP(1)N3	π^* (N1-N2)	45.93	0.23	0.10
	π^* (C4-O10)	57.33	0.27	0.11
LP(1)N5	π^* (C4-O10)	47.75	0.28	0.11
	π^* (C6-N7)	41.25	0.28	0.10
	π^* (C8-C9)	31.46	0.30	0.09
LP(2)O10	σ^* (N3-C4)	26.35	0.67	0.12
	σ^* (C4-N5)	27.62	0.65	0.12
LP(2)O12	σ^* (C8-C11)	18.30	0.67	0.10
	σ^* (C11-N13)	22.81	0.73	0.12
LP(1)N13	π^* (C11-O12)	69.05	0.27	0.12
LP(1)S28	σ^* (N26-C27)	18.02	1.54	0.15
LP(2)S28	π^* (N26-C27)	60.58	0.25	0.11
π^* (N1-N2)	π^* (C8-C9)	43.97	0.06	0.08
π^* (C6-N7)	π^* (C8-C9)	92.37	0.02	0.06

Note: where E(2) = Energy of hyper conjunctive interactions; E(j)-E(i) = Energy difference between the donor (i) and acceptor (j) NBO orbitals and F(i,j) = Fock matrix element between i and j NBO orbital.

4.4.8 Vibrational Assignment

The TMZ-BITC(3) molecule with 50 atoms produces 144 normal modes of vibrations from the $3N-6$ relation, consisting of 49 stretching, 48 bending, and 47 torsional modes as tabulated in **Table 4.24**. There are 51 modes related to C-H bonds out of 144 normal modes. The 144 normal vibrational modes are assigned based on the detailed movement of individual atoms. The computed wavenumbers obtained are usually higher than the observed wavenumbers due to the combination of electron similarity effects and DFT basis set deficiencies. As a result, scaling factors are used to fit the experimental values, with a scaling factor of 0.958 for values greater than 1800 cm^{-1} and a scaling factor of 0.983 for values less than 1800 cm^{-1} . Only Potential energy distribution contributions (PED) $\geq 10\%$ were considered in the assignments of vibration modes. The calculated wavenumbers and assignments for TMZ-BITC(3) in gas phase by using the B3LYP/6-311++G(d,p) method are shown in **Table 4.24**. After that, a brief discussion of assignments by regions is presented at continuation.

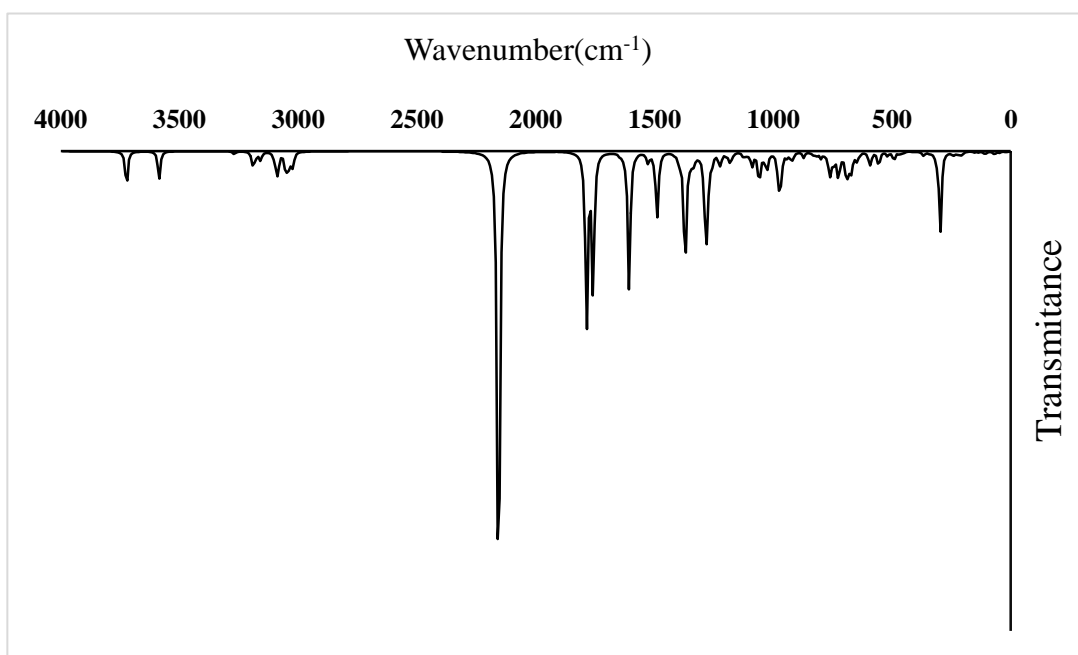


Figure 4.18: DFT FT-IR spectra of TMZ-BITC(3).

Assignments bands:

4000–2000 cm⁻¹ region:

In this region, the stretching modes of N–H, C–H, N=C and CH₂ groups present in TMZ-BITC(3) are expected. The bands characteristics of NH groups are generally observed around 3500–3300 cm⁻¹. This absorption is strongly influenced by the chemical environment, in particular when NH groups are involved in the intramolecular or intermolecular hydrogen bond. In this case, the SQM calculations predict the N-H asymmetric and symmetric stretching modes of amide at 3566.91 and 3435.06 cm⁻¹. Normally, in related compounds the C–H stretching vibrations of aromatic rings are assigned in the region 3200–3000 cm⁻¹. For TMZ-BITC(3), the CH stretching modes of benzyl ring were predicted by calculations between 3060.15 and 3025.65 cm⁻¹. The C-H stretching mode corresponding to CH₂ group is predicted by the SQM calculations at 2955.45 and 2910.59 cm⁻¹. The C-H asymmetric and symmetric stretching modes of cyclobutene calculated at 3025.28 and 3055.53 cm⁻¹ respectively. The C-H asymmetric and symmetric stretching modes of cyclopentane ring at 2955.83–2916.16 and 2924.26 cm⁻¹. The N=C stretching modes of isothiocyanate group is predicted at 2065.79 cm⁻¹.

2000–1000 cm⁻¹ region:

The C=O, C=C, S=C, C–C, N=N and C–N stretching modes, deformation and rocking modes of NH, CH and CH₂ groups and, some deformations of the rings of TMZ-BITC(3) are characteristics of this region. In particular, the C=O stretching mode is usually assigned free of other vibrations (1800–1600 cm⁻¹). In particular, the C=O stretching mode is usually assigned free of other vibrations (1800–1600 cm⁻¹). Here, the two C=O stretching mode is predicted at 1755.11 and 1728.49 cm⁻¹. The N=N stretching mode of tetrazine ring calculated at 1502.94 cm⁻¹. The C–N stretching modes of imidazole ring is calculated at 1391.84, 1348.79 and 1318.31 cm⁻¹. The benzyl ring in plane deformation is calculated at 1617.04, 1496.22, 1452.71 and 1236.47 cm⁻¹. NH₂ wagging at 1579.58 and scissoring at 1553.50 cm⁻¹. C–H rocking modes of imidazole ring at 1166.47 and 1206.32 cm⁻¹.

1000–0 cm⁻¹ region:

In this region, the S-C stretching, C –H and N –H out-of-plane deformations, deformations, wagging and twisting modes of C = O group, deformations and torsions modes of rings of TMZ-BITC(3) are calculated. The S-C stretching of isothiocyanate group is calculated at 706.40 and 679.79. The out-of-plane of benzyl ring is calculated at 803.55 and 715.43 cm⁻¹, carboxamide at 784.12-688.09 cm⁻¹. The twisting of N-H in NH2 group is calculated at 553.27 and 580.02 cm⁻¹. The out-of-plane of the whole molecule is calculated at 462.05-0 cm⁻¹.

Table 4.24: Vibrational assignments of TMZ-BITC(3) fundamental modes along with calculated IR and PED using the B3LYP method.

Mode	Calculated (cm ⁻¹)	Scaled (cm ⁻¹)	Intensity (kM/mol)	Characterization of normal modes with PED (%)
144	3723.29	3566.91	86.50	ν _a NH ₂ (98)
143	3585.66	3435.06	66.28	ν _s NH ₂ (98)
142	3269.64	3132.32	6.54	νC6-H16(99)
141	3194.31	3060.15	3.35	νC24-H36(70) νC23-H37(27)
140	3189.49	3055.53	30.29	νC33-H43(45) νC34-H42(53)
139	3179.73	3046.18	11.38	νC24-H36 (27) νC22-H38(22) νC23-H37(50)
138	3163.58	3030.71	4.15	νC22-H38(75) νC23-H37 (23)
137	3158.30	3025.65	3.38	νC20-H39(99)
136	3157.91	3025.28	13.94	νC33-H43(54) νC34-H42 (46)
135	3101.46	2971.19	9.52	νC18-H35(89)
134	3092.94	2963.04	24.68	νC30-H45(74) νC30-H46 (10)
133	3085.41	2955.83	34.75	νC29-H44 (11) νC29-H49(75)
132	3085.02	2955.45	10.83	νCH ₂ (84)
131	3052.47	2924.26	38.36	νC31-H47(46) νC32-H48(47)
130	3049.28	2921.21	9.46	νC17-H50(81)
129	3044.01	2916.16	5.87	νC31-H47(49) νC32-H48 (46)
128	3038.20	2910.59	26.59	νCH ₂ (84)
127	3026.64	2899.52	17.82	νC30-H46(83)
126	3021.46	2894.56	21.26	νC29-H44(85)
125	2156.36	2065.79	1200.43	νN26-C27(83)
124	1785.46	1755.11	408.01	νO10-C4(85)
123	1758.38	1728.49	326.51	νO12-C11(79)
122	1645.00	1617.04	5.94	νC24-C23 (22) νC20-C19(24) νC21-C20 (13) νC23-C22(12) βH39C20C21(11)
121	1628.12	1600.44	5.19	νC22-C21(34) βC24C23C22(13)

120	1621.58	1594.01	4.20	υC34-C33(83)
119	1606.90	1579.58	319.46	υC9-C8(10) βH15N13H14(67)
118	1580.36	1553.50	3.51	υC9-C8(41) βH15N13H14 (23)
117	1528.93	1502.94	19.65	υN2-N1(60)
116	1522.09	1496.22	6.49	βH39C20C21(16) βH37C23C22(31)
115	1502.07	1476.54	5.27	βH49C29H44(44) βH46C30H45(46)
114	1496.07	1470.63	8.16	βH41C25H40(85)
113	1490.62	1465.28	12.29	βH49C29H44 (42) βH46C30H45(41)
112	1489.02	1463.71	134.54	υN2-N1 (10) βN5C6N7(22) βH16C6N7(20) βC8N7C6(12)
111	1477.83	1452.71	7.90	υC20-C19(17) υC21-C20(13) βH36C24C23(12) βH35C18C19(12) βH38C22C23(10)
110	1415.91	1391.84	2.44	υN5-C6(23) τH35C18C19C20 (15)
109	1395.77	1372.04	18.15	υN5-C6 (14) τH50C17C30C31 (14) τH35C18C19C20 (29)
108	1392.34	1368.67	5.55	βH35C18C19(25) τH50C17C30C31(27)
107	1372.12	1348.79	201.46	υN1-C9(18) υN7-C8(12)
106	1368.40	1345.14	86.54	βH40C25N26 (19) τH40C25N26C27(21) τH41C25N26C27 (24)
105	1351.28	1328.31	12.30	τH35C18C19C20 (15)
104	1349.15	1326.22	0.87	υC24-C23(13) βH36C24C23 (19) βH39C20C21(26) βH38C22C23(17)
103	1343.99	1321.14	5.95	βH50C17C30(48) τH50C17C30C31 (12) τH46C30C31C32 (20)
102	1341.11	1318.31	7.95	υN5-C6 (14) υN5-C9(42)
101	1333.91	1311.24	10.79	βH44C29C32 (19) βH48C32C33(33) τH48C32C33C34 (10)
100	1333.35	1310.69	8.65	υC31-C34 (11) βH47C31C34(32) τH47C31C34C33(10)
99	1315.74	1293.37	6.07	τH44C29C32C31(10)
98	1297.28	1275.23	13.65	βH43C33C34 (25) βH42C34C33(26)
97	1285.30	1263.45	56.96	βH45C30C31(10)
96	1282.06	1260.27	170.77	υN3-C4 (12) βC4N3N2(12)
95	1278.87	1257.13	9.10	τH44C29C32C31(10) τH49C29C32C31 (25)
94	1270.98	1249.38	37.89	υN7-C8(22)
93	1257.85	1236.47	11.40	υC21-C20 (10) υC25-C21(13) υC19-C18(17) βC21C20C19 (10)

92	1255.75	1234.40	7.88	βH40C25N26(49) τH41C25N26C27 (14)
91	1227.19	1206.32	19.49	βH16C6N7(28)
90	1223.32	1202.52	10.91	βH47C31C34(11) τH47C31C34C33 (13) τH48C32C33C34 (15)
89	1217.37	1196.68	6.16	βH35C18C19 (10)
88	1199.92	1179.52	4.57	βH36C24C23 (23) βH38C22C23(21) βH37C23C22(27)
87	1186.65	1166.47	12.01	ϖN7-C8 (17) βH16C6N7 (18)
86	1179.98	1159.92	17.14	ϖC25-C21(13) ϖC19-C18 (13) βH39C20C21 (24) βH37C23C22 (14)
85	1171.43	1151.52	1.33	βH47C31C34 (13) βH48C32C33 (15)
84	1166.77	1146.94	3.62	βH44C29C32(19) βH45C30C31(17)
83	1126.63	1107.48	5.78	ϖC31-C34 (11) τH47C31C34C3315 τH48C32C33C34(13)
82	1125.77	1106.63	3.71	ϖC17-C18(20)
81	1119.22	1100.19	3.61	ϖN26-C25(11) βH38C22C23(10)
80	1108.93	1090.07	6.64	ϖN26-C25 (36) ϖS28-C27(28)
79	1092.09	1073.53	11.36	ϖN13-C11 (16) βH14N13C11(44)
78	1088.10	1069.61	23.37	ϖC29-C17 (18) βC32C29C17(11)
77	1059.87	1041.85	75.00	ϖN3-C4(13) ϖC29-C17(19)
76	1043.27	1025.53	8.23	βH43C33C34 (11) βH42C34C33 (18)
75	1037.25	1019.62	3.94	ϖC32-C29(30) βH43C33C34(14)
74	1030.52	1013.00	11.97	ϖC30-C31(16) βC30C31C34 (10) βH42C34C33(11)
73	1024.88	1007.46	30.66	ϖN13-C11 (12) βN2N1C9(14) βC8N7C6(14)
72	1017.38	1000.09	0.95	ϖC22-C21 (11) ϖC23-C22 (10) βC24C23C22 (36) βC22C21C20 (15) βC23C22C21(14)
71	1004.60	987.52	1.71	τH36C24C23C22(19) τH37C23C24C19(38) τC24C23C22C21(25)
70	977.87	961.24	75.42	ϖN3-N2 (12)
69	967.41	950.96	57.11	τH42C34C33C32(28)
68	963.94	947.55	0.60	τH43C33C34C31(24) τH42C34C33C32(25)
67	943.88	927.83	1.32	τH36C24C23C22 (26) τH38C22C23C24 (32)
66	943.11	927.08	7.31	τH36C24C23C22(10) τH38C22C23C24(11)
65	938.86	922.90	2.26	τH43C33C34C31(14) τH42C34C33C32(12)

64	923.63	907.93	18.66	τ H39C20C21C25 (44)
63	914.56	899.01	7.97	β C23C22C21(12) τ H39C20C21C25(22)
62	897.18	881.93	0.40	υ C31-C34 (10) υ C33-C32(12) β C31C34C33(36)
61	871.78	856.96	13.40	υ C29-C17 (11) τ C34C33C32C2913 γ C30C32C34C31 (11)
60	847.37	832.97	1.03	υ N3-C18(17) β N2N1C9 (10)
59	833.97	819.79	6.29	τ H16C6N7C882 τ N5C6N7C8(11)
58	821.68	807.71	3.43	β C34C33C32(20) β C31C34C33(18)
57	817.45	803.55	5.96	τ H37C23C24C19 (29)
56	800.66	787.05	9.18	υ C22-C21(11) υ C25-C21(10) β C19C18N3 (10)
55	797.68	784.12	5.48	τ C9C8N7C612 γ O12N13C8C1150 γ C11C9N7C8 (19)
54	780.08	766.82	5.59	τ H44C29C32C3117 τ H45C30C31C32 (10)
53	762.20	749.25	56.86	τ H43C33C34C31(35) τ H42C34C33C32 (33)
52	747.28	734.58	26.31	γ O10N5N3C4 (74)
51	727.80	715.43	47.40	τ H36C24C23C22(13) τ C22C21C20C19 (13)
50	718.62	706.40	20.75	υ S28-C27(13) γ C25C20C22C21(11)
49	700.30	688.40	1.81	υ N1-C9(21) υ N7-C8(10) β C9C8N7(10)
48	699.99	688.09	2.44	τ C9C8N7C6(18) τ N3N2N1C9 (12) γ O12N13C8C11 (17) γ N1N5C8C9 (21)
47	691.55	679.79	65.69	υ S28-C27 (13)
46	675.26	663.78	51.70	β O12C11N13(13)
45	665.73	654.42	12.25	τ H16C6N7C8(11) τ N5C6N7C8(51)
44	656.20	645.05	1.88	β C34C33C32 (15) τ C31C34C33C32 (22)
43	647.97	636.95	17.95	υ N26-C25(12) υ S28C27(10)
42	636.53	625.71	5.46	β C21C20C19(16) β C17C18C19 (12)
41	595.21	585.09	18.92	τ H15N13C11C8(10) τ C9C8N7C6 (32)
40	589.99	579.96	15.42	τ H14N13C11C8 (25) τ H15N13C11C8 (28) τ N5C6N7C8 (12)
39	586.20	576.24	2.10	β O12C11N13 (11) β N13C11C8(10) β C11C8N7 (10)
38	556.59	547.13	34.04	υ N3-N2(24) β O12C11N13(10) β C4N3N2(14) β N3N2N1(14)
37	552.29	542.91	0.63	τ H15N13C11C8(10) τ C9C8N7C6 (32) τ N3N2N1C9 (20)

36	518.62	509.80	9.49	β C22C21C20 (10) τ C23C22C21C20 (14)
35	491.58	483.22	21.37	β S28C27N26(69)
34	470.04	462.05	4.65	ν C11-C8(11) β O10C4N3(10) β O12C11N13 (11) β N13C11C8 (11) β C11C8N7(10)
33	460.52	452.69	3.22	β C30C31C34 (15) β C33C32C29(11) τ C34C33C32C29 (15)
32	451.50	443.83	1.97	β S28C27N26 (12) τ C24C23C22C21(13) τ S28C27N26C25(30)
31	446.73	439.13	0.30	τ S28C27N26C25 (66)
30	410.80	403.81	0.75	β C20C19C18(16)
29	376.11	369.71	0.59	β C33C32C29(17)
28	365.93	359.71	9.32	β N13C11C8(12)
27	341.44	335.64	2.58	β N13C11C8(21)
26	339.74	333.96	0.67	β C25C21C22 (25) β C19C18N3(11)
25	315.67	310.30	4.66	β O10C4N3(19) β N1C9C8(21)
24	310.12	304.85	10.63	β N26C25C21(22) τ C23C22C21C20(16)
23	296.95	291.90	184.57	τ H14N13C11C8(39) τ H15N13C11C8 (38)
22	263.14	258.67	0.30	β C17C18C19(11) β C29C17C18(17)
21	242.35	238.23	8.32	γ N1N5C8C9(45)
20	227.14	223.28	5.20	τ N2N1C9N517 γ C11C9N7C8(19)
19	215.07	211.41	4.58	β C18N3N2(16)
18	209.89	206.32	1.50	β C20C19C18(10) β C25C21C22 (10)
17	204.29	200.82	6.22	τ C21C20C19C1814 τ C23C22C21C20(10) γ C11C9N7C8(10) γ C4C18N2N3(11)
16	170.46	167.56	0.06	β C33C32C29(12) τ C31C34C33C3230
15	152.28	149.69	2.32	β C20C19C18 (10) β C11C8N7(20)
14	134.77	132.48	1.99	β C27N26C25(10) β C20C19C18 (12) γ C25C20C22C21(22)
13	110.52	108.65	4.35	τ N3N2N1C9(11) γ C4C18N2N3 (30)
12	103.82	102.05	2.78	β C11C8N7 (18) τ C33C32C29C1711
11	87.86	86.37	0.47	τ N2N1C9N5 (21) τ N3N2N1C915 γ C11C9N7C8 (19)
10	68.92	67.75	6.68	β C27N26C25(37)
9	63.43	62.35	0.89	β C17C18C19(23) τ C21C20C19C18 (15) τ C29C17C18N3(10)

8	48.85	48.02	0.15	β C18N3N2 (10) τ C32C29C17C18(36) γ C17N3C19C18(16)
7	47.50	46.69	2.88	τ N13C11C8C9(74)
6	41.69	40.98	0.11	τ C29C17C18N3(55)
5	24.90	24.48	0.20	τ C20C19C18N3(19) τ C18N3N2N1 (24)
4	20.66	20.31	1.16	τ C19C18N3N2(66)
3	18.65	18.33	0.35	τ N26C25C21C20(21) τ C18N3N2N1(20)
2	10.81	10.62	0.63	τ C20C19C18N3(43) τ N26C25C21C20 (17)
1	3.02	2.97	0.60	τ C27N26C25C21(45) τ N26C25C21C20(44)

Symbol for stretching here: stretching (a = antisymmetric; s = symmetric); β = deformation in the plane; γ = deformation out of the plane; τ = torsion; β R = deformation ring; τ R = torsion ring; τ w=twisting; δ =deformation; and R=Ring

4.5 TMZ-BITC(4)

4.5.1 Optimization and properties in both media

TMZ-BITC(4) was optimized at DFT/B3LYP/6-311++G(d,p) level of theory in both the gas and the aqueous phases as depicted in **Table 4.25**. Furthermore, frequency calculations were performed at the same level of theory to ensure that the optimized structure corresponds to true energetic minima. Results of optimizations of TMZ-BITC(4) in the gas phase and aqueous solution can be seen in **Figure 4.19**. The difference between the value optimized in the aqueous solution and the corresponding gas phase ($-1743.03+1743.05 = 0.06$ Hartrees = 69.31 kJ/mol) was used to calculate the relative energy. It can be seen that the calculated total energies (E) in both phases, as well as the corrected ZPVE energy (EZPVE) were primarily negative. The differences in dipole moments (μ) from 3.02 D in the gas phase to 5.89 D in the aqueous solution imply that an ionic bond is more prominent in the predicted solution with increased polarity. Increase or expansion of volume can be seen in aqueous solution from 420.5 A³ to 424.4 A³.

Table 4.25: Calculated total energies (E), dipole moments (μ), and volumes (V) for compound TMZ-BITC(4) in gas and aqueous phase phases by using B3LYP/6-311++ G(d,p) basis set.

Medium	E (Hartrees)	EZPVE (Hartrees)	μ (D)	V(A ³)
Gas phase	-1742.67	-1743.03	6.30	420.4
Aqueous phase	-1742.70	-1743.05	9.16	420.6

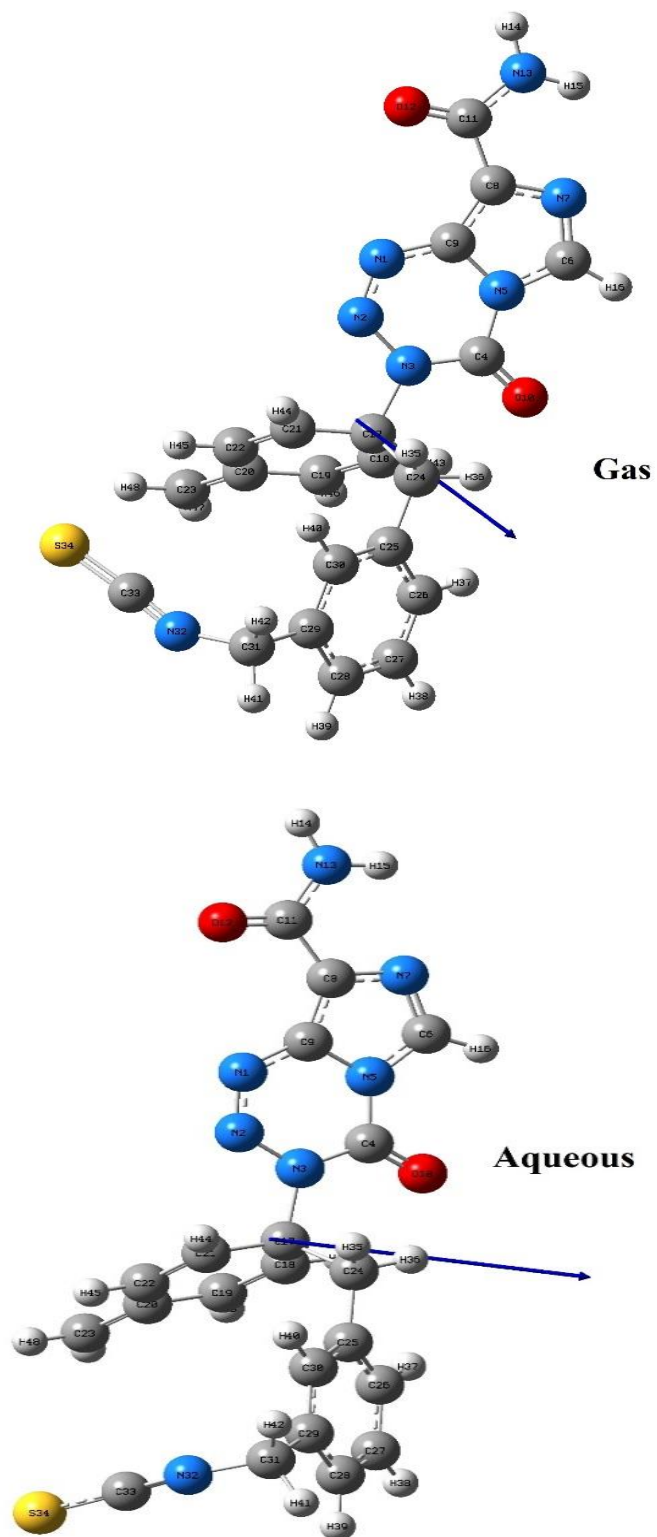


Figure 4.19: Optimized structure of TMZ-BITC(4) at B3LYP/6-311++G(d,p) basis set in gas phase (up) aqueous solution (bottom)

4.5.2 Geometrical parameters

The optimized structure of TMZ-BITC(4) possess C_1 point group symmetry. The optimized geometrical parameters of TMZ-BITC(4) in gas phase and aqueous solution calculated at B3LYP/ 6-311++G(d,p) method is presented in **Table 4.26**. The N=N and N-N bond length in the tetrazine ring is found to be 1.26 Å and 1.394 Å respectively. The C=O bond length is found to be 1.21 Å. The C-N bond length in the Isothiocyanate is 1.19 Å. The C-C bond lengths in the benzyl ring are in the range of 1.4 Å to 1.4 Å. The C=S bond of Isocyanate group bond length is found to be 1.59 Å. The C-C and C=C bond length in the cyclohexadiene ring are 1.460 Å and 1.338 Å respectively.

Table 4.26: Selected geometrical parameters of TMZ-BITC(4) using B3LYP/6-311++G(d,p) basis set.

Bond lengths(Å)		
Parameters	Gas	Aqueous
N1-N2	1.26	1.27
N1-C9	1.36	1.36
N2-N3	1.39	1.38
N3-C4	1.39	1.39
N3-C17	1.54	1.54
C4-O10	1.21	1.21
N5-C6	1.37	1.37
N7-C8	1.37	1.38
C8-C9	1.39	1.39
C17-C24	1.57	1.57
C18-C19	1.34	1.34
C18-H43	1.08	1.08
C19-C20	1.46	1.46
C20-C23	1.35	1.35
C24-C25	1.51	1.51
C25-C26	1.40	1.40
C26-C27	1.39	1.39
C27-C28	1.39	1.39
C27-H38	1.08	1.08
C29-C30	1.40	1.40
C29-C31	1.52	1.52
N32-C33	1.19	1.18
C33-S34	1.59	1.61

Bond angles(°)		
Parameters	Gas	Aqueous
N2-N1-C9	119.66	119.47
N1-N2-N3	121.16	121.49
N2-N3-C4	125.13	124.97
N2-N3-C17	114.15	114.26
N5-C6-N7	110.61	110.53
N7-C8-C9	109.21	109.12
C8-C11-N13	113.17	113.97
N3-C17-C21	108.70	108.38
C17-C18-C19	123.22	123.29
C18-C19-C20	122.88	122.77
C26-C27-C28	120.18	120.23
C27-C28-C29	119.97	119.82
C28-C29-C30	119.31	119.52
C29-C31-N32	112.65	112.13
Dihedral angles(φ)		
Parameters	Gas	Aqueous
N2-N1-C9-N5	-0.39	0.56
N1-N2-N3-C4	0.34	-1.43
N1-N2-N3-C17	-178.82	-179.43
N3-C4-N5-C6	-179.58	179.52
N3-C4-N5-C9	0.60	-0.66
C4-N5-C6-N7	-179.87	179.98
C9-N5-C6-N7	-0.03	0.14
C6-N5-C9-C8	-0.02	-0.13
N5-C6-N7-C8	0.07	-0.08
C17-C18-C19-C20	-0.24	-0.57
C18-C19-C20-C22	0.77	-0.14
C18-C19-C20-C23	-178.87	-179.72
C19-C20-C22-C21	1.14	1.93
C23-C20-C22-C21	-179.22	-178.50
C25-C26-C27-C28	-0.10	-0.30
C26-C27-C28-C29	-0.38	-0.12
C27-C28-C29-C30	0.28	0.21
C28-C29-C30-C25	0.32	0.12

The bond angle N-N-N in the tetrazine ring is calculated at 121.16°. The C-C-C bond angles in the benzyl ring are in the range of 119.31° to 120.18° which depicts the hexagonal shape of a benzene ring. The dihedral angles found for the molecules shows planarity in the rings.

4.5.3 Atomic charges and MEP

The atomic charges and molecular electrostatic potentials (MEP) of the optimized structures of TMZ-BITC(4) for the gas phase and the aqueous solution are summarized in **Table 4.27**. The Mulliken charges on N-atoms shows that N2 is the most positive and N13 is the most negative while NPA atomic charges shows that all the N-atoms are negative except for N2 in both cases. Both Mulliken and NPA shows that the two O-atoms are negative. The trends in Mulliken and NPA charges for C-atoms are different to each other, wherein Mulliken atomic charge shows positivity for certain C-atoms while NPA atomic charges show negativity. C25 is the most positive charge in NPA and C6 is the most positive charge in the Mulliken charge.

The molecular electrostatic potentials (MEP) charges are also presented in **Table 4.27**. The same trends of values are observed in both media and the relative expected tendency is observed as MEP O-atoms > MEP N-atoms. The MEP of TMZ-BITC(4) molecule shows the negative potential region around oxygen atom of O12 (carboxamide group). The most positive region is localized on H13 of the amine group (N24 and N17) indicating a possible site for electrophilic attack, respectively.

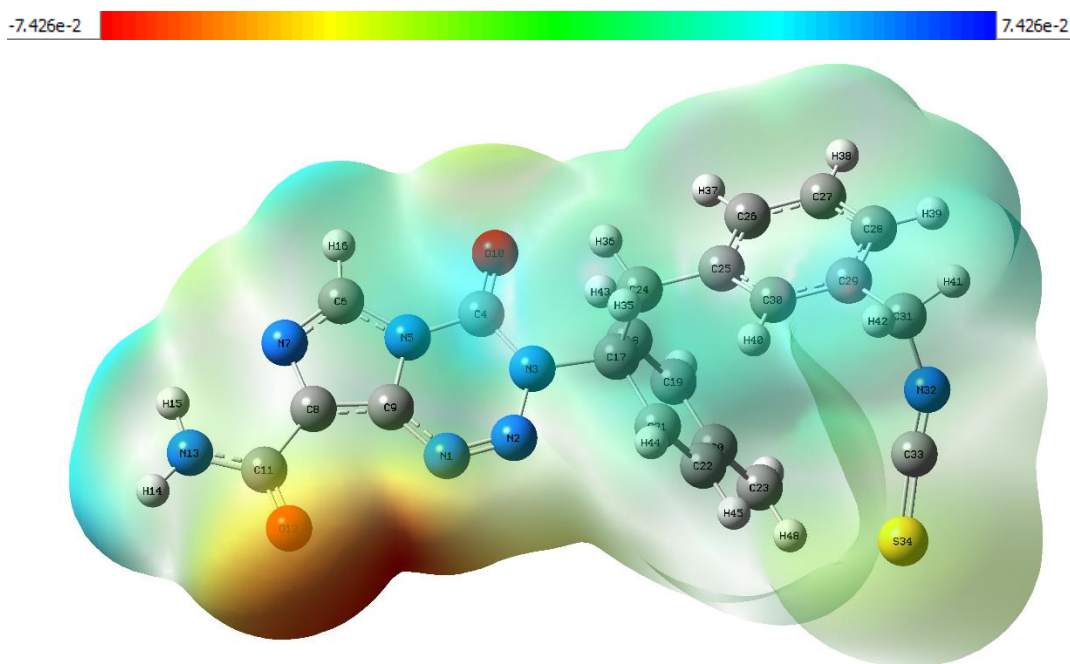


Figure 4.20: Calculated electrostatic potential surfaces on the molecular surface of TMZ-BITC(4) in the gas phase, using 6-311++G(d,p) basis set.

Table 4.27: Mulliken, Natural Population Analysis (NPA) charges (in a.u.) and Molecular Electrostatic Potentials (MEP) of TMZ-BITC(4) in the gas phase and aqueous phase calculated at B3LYP/6-311++G(d,p) level of theory.

Atoms	Gas Phase			Aqueous Phase		
	Mulliken	NPA	MEP	Mulliken	NPA	MEP
N1	0.11	-0.17	-18.33	-0.01	-0.21	-18.34
N2	0.45	0.02	-18.30	0.42	0.02	-18.30
N3	0.29	-0.32	-18.29	0.33	-0.31	-18.27
C4	-0.07	0.83	-14.58	-0.07	0.85	-14.57
N5	-0.07	-0.45	-18.28	-0.05	-0.44	-18.27
C6	0.60	0.25	-14.68	0.64	0.27	-14.66
N7	-0.06	-0.47	-18.37	-0.10	-0.48	-18.37
C8	-0.09	0.06	-14.71	-0.13	0.05	-14.71
C9	-0.01	0.29	-14.67	0.10	0.30	-14.67
O10	-0.21	-0.60	-22.35	-0.25	-0.60	-22.34
C11	-0.09	0.63	-14.66	-0.07	0.64	-14.67
O12	-0.34	-0.60	-22.41	-0.46	-0.68	-22.44
N13	0.20	-0.80	-18.37	0.24	-0.77	-18.36
C17	-1.27	0.11	-14.67	-1.09	0.11	-14.67
C18	0.05	-0.20	-14.76	-0.11	-0.19	-14.75
C19	-0.51	-0.16	-14.76	-0.34	-0.17	-14.76
C20	0.95	-0.10	-14.75	0.82	-0.11	-14.75
C21	-0.54	-0.18	-14.76	-0.14	-0.17	-14.76
C22	-0.22	-0.17	-14.76	-0.35	-0.18	-14.77
C23	-0.23	-0.30	-14.77	-0.26	-0.31	-14.77
C24	0.53	-0.40	-14.75	0.71	-0.40	-14.74
C25	1.23	-0.03	-14.75	0.79	-0.04	-14.74
C26	-0.09	-0.18	-14.76	-0.03	-0.19	-14.76
C27	-0.33	-0.19	-14.76	-0.33	-0.20	-14.76
C28	-0.14	-0.19	-14.76	0.10	-0.20	-14.75
C29	0.60	-0.05	-14.74	0.61	-0.06	-14.74
C30	-0.37	-0.18	-14.76	-0.61	-0.15	-14.75
C31	-0.26	-0.19	-14.69	-0.15	-0.20	-14.67
N32	0.17	-0.44	-18.36	0.24	-0.39	-18.34
C33	0.05	0.23	-14.68	0.04	0.25	-14.68
S34	-0.32	-0.05	-59.25	-0.47	-0.16	-59.28

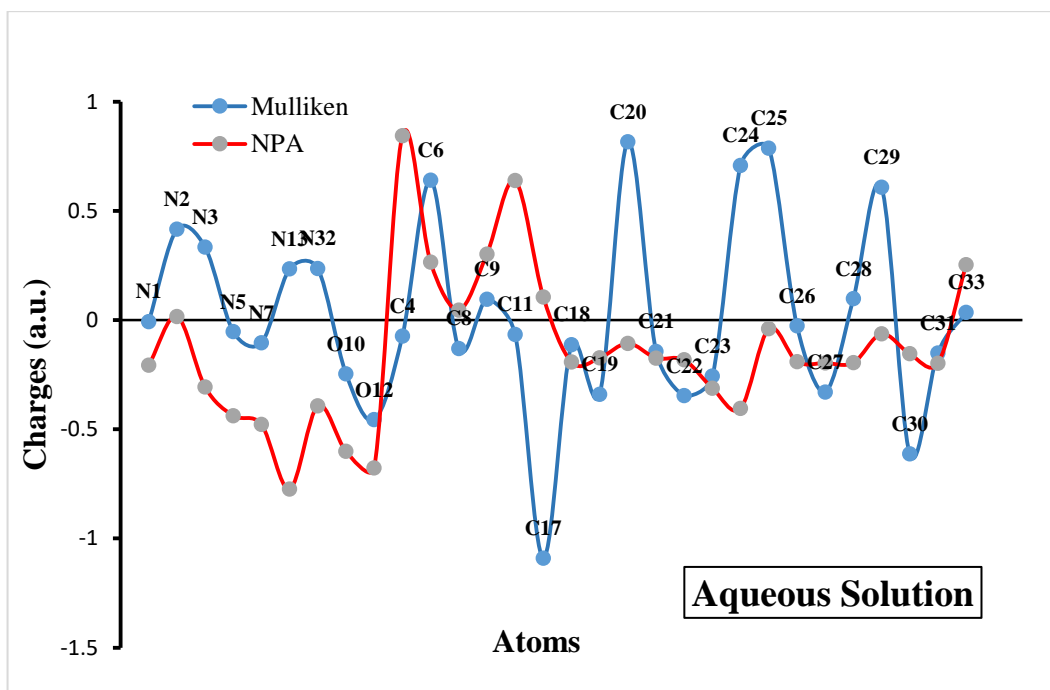
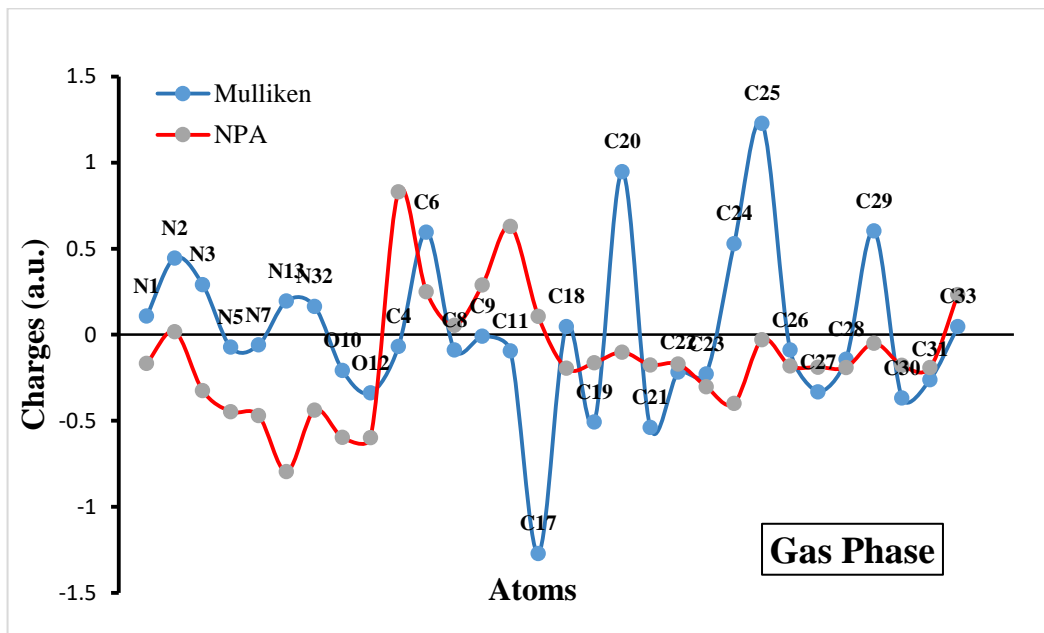


Figure 4.21: Graph showing the trends for Mulliken and Natural Population Analysis (NPA) Atomic charges of TMZ-BITC(4) in the gas phase (upper) and the aqueous solution (bottom).

4.5.4 ^1H and ^{13}C NMR analysis

The ^1H and ^{13}C NMR calculations were performed by GIAO (Gauge-Independent Atomic Orbital) method at the B3LYP/6-311++G(d,p) basis set in DMSO solvent. The calculated chemical shift of TMZ-BITC(4) is shown in **Table 4.28**. The ^1H NMR of TMZ-BITC(4) in DMSO shows a chemical shift at 8.41 ppm(deshield) for H16 of imidazole ring. The two proton of NH_2 shows chemical shifts at 7.28 ppm(H15) and 5.14ppm(H14). The aromatic protons of the title molecule chemical range is found in the range of 7.38-7.60 ppm. The ^{13}C NMR calculations of the title shows a chemical shift of 165.22 ppm(C11) of carboxamide group. The lowest chemical shift of 46.59ppm is found for C24(CH_2). The chemical shift of aromatic carbons are calculated in the range of 132.97-144.41 ppm.

Table 4.28: Calculated chemical shifts of TMZ-BITC(4) calculated in GIAO method using DMSO as solvents.

^1H NMR		^{13}C NMR	
Atom	Calculated(ppm)	Atom	Calculated(ppm)
16-H	8.41	11-C	165.22
40-H	7.60	25-C	144.41
37-H	7.57	20-C	143.89
38-H	7.48	4-C	143.42
39-H	7.38	33-C	142.91
15-H	7.28	29-C	141.80
43-H	7.28	9-C	139.45
44-H	6.84	30-C	138.42
45-H	6.77	19-C	138.02
46-H	6.62	26-C	137.00
47-H	5.22	8-C	136.93
48-H	5.22	22-C	136.54
14-H	5.13	21-C	136.40
42-H	5.01	27-C	133.09
36-H	4.55	28-C	132.97
41-H	3.84	6-C	132.39
35-H	3.17	18-C	131.86
		23-C	124.35
		17-C	78.70
		31-C	51.38
		24-C	46.59

4.5.5 UV-vis analysis

The Wavelengths (λ) and the excitation energies (E) are both expressed in nm, and oscillator strength (f) of TMZ-BITC(4) evaluated by the TD-DFT method are shown in **Table 4.29** and **Figure 4.22** displays the plot of the ultraviolet spectra. A strong theoretical absorption peak is found at 329.64 nm with an oscillator strength of 0.2167 and an excitation energy of 3.76 eV. This peak is the major contribution of the excitation from HOMO-1 to LUMO with 75%. The peak observed 395.75 nm with oscillator strength of 0.0007 and excitation energy of 3.13 eV have the major contribution of 98% from HOMO to LUMO transition, and the peak observed at 321.99 nm with oscillator strength of 0.01 and excitation energy of 3.85 eV have the major contribution from HOMO-6 to LUMO (34%). Both of these peaks relate to the $\pi \rightarrow \pi^*$ transitions.

Table 4.29: Electronics properties of TMZ-BITC(4) calculated using TD-DFT (B3LYP)/6-311++G(d,p)

Wavelength λ (nm)	Energy eV	Oscillator strength f	Symmetry	Major contributions
395.75	3.13	0.0007	Singlet-A	HOMO \rightarrow LUMO (98%)
329.64	3.76	0.2167	Singlet-A	H-1 \rightarrow LUMO (75%), H-3 \rightarrow LUMO (14%)
321.99	3.85	0.01	Singlet-A	H-6 \rightarrow LUMO (34%), H-4 \rightarrow LUMO (21%), H-2 \rightarrow LUMO (28%)

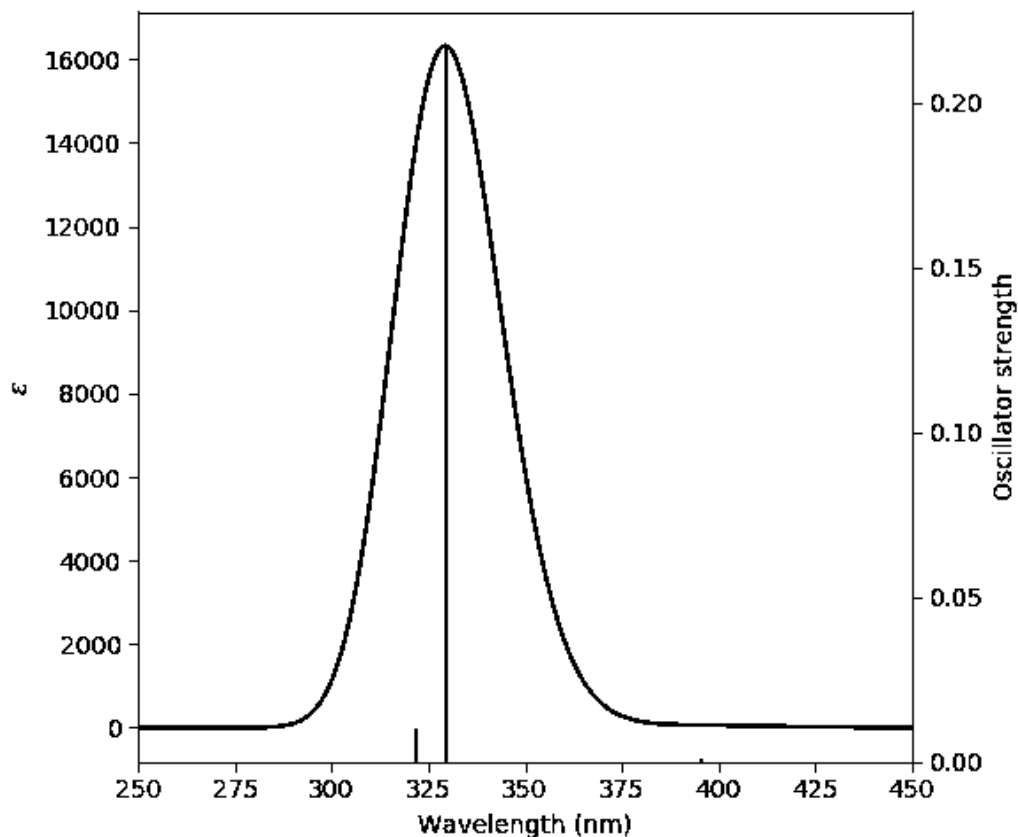


Figure 4.22: UV spectra of TMZ-BITC(4) calculated at B3LYP/6-311++G(d,p).

4.5.6 Frontier Molecular Orbitals analysis (FMO)

The computation results indicate that the molecule has 804 molecular orbitals, where 113 are occupied, and the remaining are unoccupied molecular orbitals. Molecular orbitals 113 and 112 were identified as LUMO and HOMO molecular orbitals, respectively. The HOMO and LUMO orbitals with energy values are shown in **Table 4.30**. HOMO is localized by π bonding type orbitals on isothiocyanate group and LUMO is localized by π^* bonding type orbitals on TMZ molecule (**Figure 4.23**). The LUMO and HOMO energies obtained are at -2.73eV and -6.58eV for the gas phase and -2.80eV and -6.57eV for the aqueous solution, respectively. The HOMO-LUMO energy gap (ΔE) for gas phase is 3.85eV, and for the aqueous phase, it is 3.77eV. Comparing the energy gap of TMZ in both media, a slight decrease in the energy gap is observed in the aqueous phase.

The tabulated FMO energy parameters and global reactivity descriptors of TMZ in both media are shown in **Table 4.30**. The electron affinity and electronegativity values of molecule shows a moderate acceptor properties as well as a high ability to pull electron density to itself. This could be attributed to the good number of N-atoms in the molecular structure with lone pairs of electrons donated for reactions. The high ionization potential of the molecule in both media indicates high reactivity of atoms and the molecule.

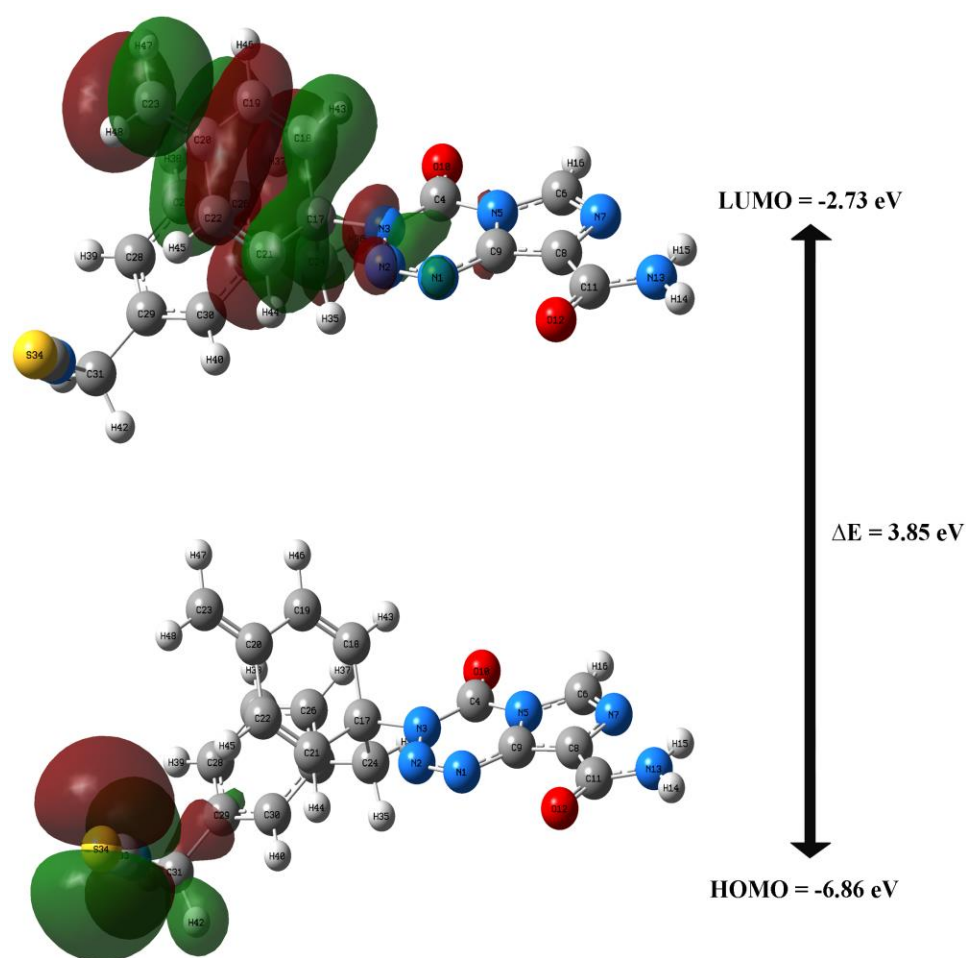


Figure 4.23: HOMO-LUMO graphical reproduction of TMZ-BITC(4)

Table 4.30: Frontier Molecular Orbitals energy parameters and global reactivity descriptors of TMZ-BITC(4).

FMOs	Gas	PCM
HOMO energy	-6.58	-6.57
LUMO energy	-2.73	-2.80
Energy gap (ΔE)	3.85	3.77
Ionization potential (I)	6.58	6.57
Electron affinity (A)	2.73	2.80
Hardness (η)	1.93	1.88
Chemical potential (μ)	-4.66	-4.68
Electronegativity (χ)	4.66	4.68
Electrophilicity (ω)	5.63	5.81

4.5.7 Natural bond orbital (NBO) analysis

The calculated E(2) energy values and types of transition, taking place in TMZ-BITC(4) structure were listed in **Table 4.31**. The results of the natural bondorbital analysis showed that the strongest intramolecular hyperconjugative interaction in the $\pi \rightarrow \pi^*$ occurs via overlapping between π (C8-N9) bonding orbital participating as donor and the π^* (N1-N2) as an acceptor antibonding orbital, which ensues a stabilization energy of 22.58 kJ/mol.

The other significant $\pi \rightarrow \pi^*$ interactions also occurs in the benzyl ring. Of all the interaction, those involving lone-pair LP(1) of nitrogen, LP(1) and LP(2) of oxygen towards the π^* are mostly higher than the other types of interaction. The lone-pair LP(1) N13 shows highest stabilizing energy of 69.27 kJ/mol with antibonding π^* (C11-O12). The LP(2) O10 also shows highest stabilizing energy of 27.97 kJ/mol with σ^* (C4-N5) among the LP to σ^* interactions. The appreciable highest interaction energies $\pi \rightarrow \pi^*$ orbital overlap intramolecular interactions in the system occurs in the rings, π (C6-C7) \rightarrow π^* (C8-C9) with stabilizing energy of 90.60 kJ/mol and π^* (N1-N2) \rightarrow π^* (C8-C9) with stabilizing energy of 44.06 kJ/mol. The highest stabilizing energy is found for π^* (N32-C33) with σ^* (C33-S34) of 116.78 kJ/mol.

Table 4.31: Second-order perturbation theory analysis of Fock matrix in NBO of TMZ-BITC(4).

Donor (i)	Acceptor (j)	E2 kJ/mol	E(j)-E(i) a.u.	F(i,j) a.u.
π (N1-N2)	π^* (C8-C9)	14.91	0.40	0.07
π (C6-N7)	π^* (C8-C9)	20.72	0.33	0.08
π (C8-C9)	π^* (N1-N2)	22.58	0.23	0.07
	π^* (C6-N7)	17.82	0.27	0.06
	π^* (C11-O12)	17.09	0.30	0.07
π (C18-C19)	π^* (C20-C23)	14.07	0.32	0.06
σ (C20-C23)	π^* (N32-C33)	15.40	3.02	0.21
π (C20-C23)	π^* (C18-C19)	15.16	0.32	0.06
	π^* (C21-C22)	14.67	0.32	0.06
π (C21-C22)	π^* (C20-C23)	14.35	0.32	0.06
σ (C23-H48)	π^* (N32-C33)	24.21	2.78	0.25
π (C25-C26)	π^* (C27-C28)	20.50	0.28	0.07
	π^* (C29-C30)	19.80	0.29	0.07
π (C27-C28)	π^* (C25-C26)	20.46	0.29	0.07
	π^* (C29-C30)	20.79	0.29	0.07
π (C29-C30)	π^* (C25-C26)	20.14	0.29	0.07
	π^* (C27-C28)	20.31	0.28	0.07
LP(1) N1	σ^* (N2-N3)	16.95	0.71	0.10
LP(1) N3	π^* (N1-N2)	46.33	0.23	0.10
	π^* (C4-O10)	57.43	0.27	0.11
LP(1) N5	π^* (C4-O10)	47.83	0.28	0.11
	π^* (C6-N7)	41.01	0.28	0.10
	π^* (C8-C9)	31.90	0.30	0.09
LP(2) O10	σ^* (N3-C4)	25.96	0.66	0.12
	σ^* (C4-N5)	27.97	0.65	0.12
LP(2) O12	σ^* (C8-C11)	18.25	0.68	0.10
	σ^* (C11-N13)	22.80	0.73	0.12
LP(1) N13	π^* (C11-O12)	69.27	0.27	0.12
LP(1) S34	σ^* (N32-C33)	17.93	1.55	0.15
π^* (N1-N2)	π^* (C8-C9)	44.06	0.06	0.08
π^* (C6-N7)	π^* (C8-C9)	90.60	0.02	0.06
π^* (C20-C23)	π^* (C21-C22)	45.26	0.01	0.07
π^* (N32-C33)	σ^* (C33-S34)	116.78	0.10	0.24

Note: where E(2) = Energy of hyper conjunctive interactions; E(j)-E(i) = Energy difference between the donor (i) and acceptor (j) NBO orbitals and F(i,j) = Fock matrix element between i and j NBO orbital.

4.5.8 Vibrational Assignment

The TMZ-BITC(4) molecule with 48 atoms produces 138 normal modes of vibrations from the $3N-6$ relation, consisting of 47 stretching, 46 bending, and 45 torsional modes as tabulated in **Table 4.32**. There are 45 modes related to C-H bonds out of 138 normal modes. The 138 normal vibrational modes are assigned based on the detailed movement of individual atoms. The computed wavenumbers obtained are usually higher than the observed wavenumbers due to the combination of electron similarity effects and DFT basis set deficiencies. As a result, scaling factors are used to fit the experimental values, with a scaling factor of 0.958 for values greater than 1800 cm^{-1} and a scaling factor of 0.983 for values less than 1800 cm^{-1} . Only Potential energy distribution contributions (PED) $\geq 10\%$ were considered in the assignments of vibration modes. The calculated wavenumbers and assignments for TMZ-BITC(4) in gas phase by using the B3LYP/6-311 ++ G(d,p) method are shown in **Table 4.24**. After that, a brief discussion of assignments by regions is presented at continuation.

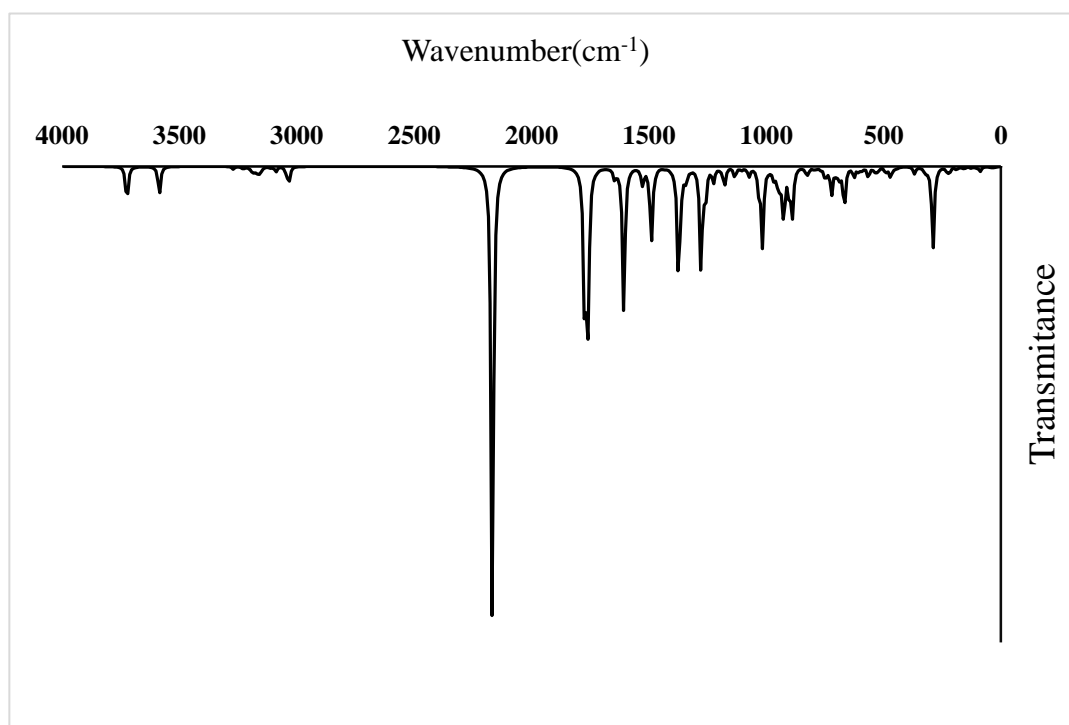


Figure 4.24: DFT FT-IR spectra of TMZ-BITC(4).

Assignments bands:

4000–2000 cm⁻¹ region:

In this region, the stretching modes of N–H, C–H, N=C and CH₂ groups present in TMZ-BITC(4) are expected. The bands characteristics of NH groups are generally observed around 3500–3300 cm⁻¹. This absorption is strongly influenced by the chemical environment, in particular when NH groups are involved in the intramolecular or intermolecular hydrogen bond. In this case, the SQM calculations predict the N-H asymmetric and symmetric stretching modes of amide at 3567.33 and 3435.38 cm⁻¹. Normally, in related compounds the C–H stretching vibrations of aromatic rings are assigned in the region 3200–3000 cm⁻¹. For TMZ-BITC(4), the C–H stretching modes of benzyl ring were predicted by calculations between 3186.51 and 3024.54 cm⁻¹. The C–H stretching mode corresponding to cyclopentene ring is predicted the SQM calculations at 2955.45 and 3060.10 cm⁻¹. The C–H asymmetric and symmetric stretching modes of cyclobutene calculated at 3228.13 and 3055.53 cm⁻¹ respectively. The CH asymmetric stretching modes of CH₂ at 3008.54–2959.90 cm⁻¹ and symmetric modes calculated at 2905.55–2915.08 cm⁻¹. The N=C stretching modes of isothiocyanate group is predicted at 2075.57 cm⁻¹.

2000–1000 cm⁻¹ region:

The C=O, C=C, S=C, C–C, N=N and C–N stretching modes, deformation and rocking modes of NH, CH and CH₂ groups and, some deformations of the rings of TMZ-BITC(4) are characteristics of this region. In particular, the C=O stretching mode is usually assigned free of other vibrations (1800–1600 cm⁻¹). Here, the two C=O stretching mode is calculated at 1742.80 and 1728.69 cm⁻¹. The N=N stretching mode of tetrazine ring calculated at 1502.49 cm⁻¹. The C–N stretching modes of imidazole ring is calculated at 1350.04 and 1383.39 cm⁻¹. The C=C stretching modes of cyclopentene ring is calculated at 1696.12 cm⁻¹, benzyl ring at 1618.55 cm⁻¹ and C–C=CH₂ at 1617.31 cm⁻¹. The SQM calculations predict the CH wagging of CH₂ at 1348.55 (C31) and 1312.08 (C24), and CH scissoring at 1475.91 and 1470.64 cm⁻¹. C–H rocking modes of imidazole ring at 1450.16 cm⁻¹, benzyl ring at 1495.23 and 1324.22 cm⁻¹.

1000–0 cm⁻¹ region:

In this region, the S-C stretching, C–H and N–H out-of-plane deformations, deformations, wagging and twisting modes of C=O group, deformations and torsions modes of the rings of TMZ-BITC(4) are calculated. The S-C stretching of imidazole group is calculated at 721.61 and 674.21 cm⁻¹. This region consist of mixture of all the deformation and out-of-plane modes. The out-of-plane for the whole molecule is calculated from 417.15-0 cm⁻¹.

Table 4.32: Vibrational assignments of TMZ-BITC(4) fundamental modes along with calculated IR and PED using the B3LYP method.

Mode	Calculated (cm ⁻¹)	Scaled (cm ⁻¹)	Intensity (kM/mol)	Characterization of normal modes with PED (%)
138	3723.72	3567.33	85.99	ν _a NH ₂ (98)
137	3585.99	3435.38	66.62	ν _s NH ₂ (98)
136	3271.19	3133.80	6.42	νC6-H16 (99)
135	3228.13	3092.55	5.53	ν _a CH ₂ (53)
134	3203.35	3068.81	2.64	νC18-H43 (95)
133	3194.25	3060.10	3.65	νC21-H44 (87) νC22-H45 (11)
132	3186.51	3052.68	12.55	νC26-H37 (28) νC27-H38 (60) νC28-H39 (11)
131	3171.40	3038.20	13.25	νC26-H37 (60) νC28-H39 (31)
130	3166.84	3033.83	1.74	νC21-H44 (12) νC22-H45 (87)
129	3161.57	3028.79	1.94	νC26-H37 (11) νC27-H38 (31) νC28-H39 (57)
128	3157.14	3024.54	6.70	νC30-H40 (98)
127	3156.12	3023.56	8.17	νC19-H46 (94)
126	3140.44	3008.54	2.25	ν _a CH ₂ (52)
125	3113.87	2983.09	2.54	ν _a CH ₂ (87)
124	3089.66	2959.90	11.87	ν _a CH ₂ (87)
123	3042.88	2915.08	18.82	ν _s CH ₂ (87)
122	3032.93	2905.55	29.33	ν _s CH ₂ (87)
121	2166.56	2075.57	1082.41	νN32-C33 (83)
120	1772.94	1742.80	391.79	νO10-C4 (83)

119	1758.58	1728.69	342.22	υO12-C11 (79)
118	1725.46	1696.12	2.68	υC18-C19 (30) υC22-C21 (26)
117	1658.64	1630.45	0.64	υC18-C19 (39) υC22-C21 (44)
116	1646.54	1618.55	7.58	υC26-C27 (22) υC27-C28 (10) υC29-C30 υC30-C25 (19) βH40C30C29 (10)
115	1645.28	1617.31	18.78	υC18-C19 (14) υC23-C20 (51) βH48C23H47 (16)
114	1628.41	1600.73	5.12	υC28-C29 (34) βC26C27C28 (13) βC29C30C25 (11)
113	1606.79	1579.47	338.74	υC9-C8 (10) βH15N13H14 (66)
112	1580.99	1554.11	3.44	υC9-C8 (44) βH15N13H14 (25)
111	1528.47	1502.49	35.82	υN2=N1 (60) υN7-C6 (12)
110	1521.09	1495.23	7.26	βH37C26C27 (10) βH38C27C28 (32) βH40C30C29 (16)
109	1501.43	1475.91	5.60	βH36C24H35 (74)
108	1496.08	1470.64	13.09	βH42C31H41 (84)
107	1489.03	1463.71	163.68	υN2-N1 (14) υN7-C6 (22) βN5C6N7 (12) βH16C6N7 (25)
106	1475.24	1450.16	6.09	υC29-C30 (14) υC30-C25 (17) βH37C26C27 (11) βH39C28C29 (14)
105	1469.91	1444.92	2.01	βH44C21C22 (10) βH45C22C21 (10) βH48C23H47 (47)
104	1430.22	1405.90	1.38	υC19-C20 (13) υC20-C22 (17) βH43C18C19 (16) βH44C21C22 (18)
103	1405.27	1381.38	2.85	υN7-C6 (12) υN5-C6 (30)
102	1394.06	1370.36	5.71	υC23-C20 (13) βH43C18C19 (16) βH44C21C22 (13) βH48C23H47 (28)
101	1373.41	1350.06	248.31	υN7-C6 (17) υN1-C9 (23) βC9C8N7 (12)
100	1371.87	1348.55	31.94	βH41C31N32 (24) τH41C31N32C33 (15) τH42C31N32C33 (13)
99	1359.44	1336.33	23.88	τH36C24C25C26 (12) τH42C31N32C33 (13)
98	1347.12	1324.22	2.52	υC26-C27 (12) βH37C26C27 (20) βH39C28C29 (20) βH40C30C29 (27)
97	1344.11	1321.26	15.46	υN5-C6 (19) βN5C6N7 (16) β C9C8N7 (12) β C8N7C6 (13)
96	1339.56	1316.79	10.03	βH46C19C20 (14) βH45C22C21 (19)
95	1334.77	1312.08	6.18	τH35C24C25C26 (20) τH36C24C25C26 (25)

94	1319.10	1296.68	2.59	β H43C18C19 (10)
93	1277.94	1256.21	254.54	ν N7-C8 (24) β N5C6N7 (25)
92	1262.47	1241.00	8.72	ν C25-C24 (14) ν C31-C29 (12)
91	1258.77	1237.37	59.70	β H41C31N32 (30)
90	1257.56	1236.18	9.17	β H41C31N32 (26)
89	1230.48	1209.56	4.23	β H43C18C19 (13) β H46C19C20 (21) β H44C21C22 (17) β H45C22C21 (24)
88	1223.48	1202.68	30.69	ν N7-C6 (10) β H16C6N7 (31)
87	1199.69	1179.30	0.99	β H37C26C27 (10) β H38C27C28 (20) β H39C28C29 (17)
86	1194.37	1174.07	2.95	β H35C24C25 (16) β H37C26C27 (12)
85	1179.35	1159.31	26.41	β H16C6N7 (15)
84	1176.66	1156.65	18.95	ν C25-C24 (10) ν C31-C29 (12) β H38C27C28 (14) β H40C30C29 (18)
83	1133.22	1113.95	24.28	β H35C24C25 (10)
82	1114.79	1095.84	1.43	ν N32-C31 (10) β H39C28C29 (11)
81	1103.08	1084.33	6.07	ν N32-C31 (38) ν S34-C33 (29)
80	1090.06	1071.53	0.64	ν O12-C11 (10) ν N13-C11 (20) β H14N13C11 (48)
79	1073.26	1055.01	21.19	ν C24-C17 (27) β C22C21C17 (18)
78	1032.39	1014.84	46.78	ν N3-C4 (22) β C4N3N2 (11)
77	1020.69	1003.34	9.46	τ H43C18C19C20 (28) τ H46C19C20C22 (32)
76	1018.10	1000.80	2.64	ν C27-C28 (10) ν C28-C29 (11) β C26C27C28 (34) β C27C28C29 (13) β C28C29C30 (13)
75	1015.70	998.43	171.41	β C8N7C6 (24)
74	1007.83	990.70	1.25	τ H44C21C22C20 (38) τ H45C22C21C17 (48)
73	994.39	977.48	0.38	τ H37C26C27C28 (19) τ H38C27C28C29 (46) τ H39C28C29C31 (18) τ C26C27C28C29 (12)
72	988.04	971.25	5.61	β H47C23C20 (13) τ H41C31N32C33 (13)
71	972.95	956.41	2.88	ν C19-C20 (12) β H47C23C20 (49)
70	967.29	950.85	21.20	ν N3-N2 (10) ν C24-C17 (11) β N3N2N1 (13)

69	953.46	937.25	27.02	β C18C19C20 (34) β C19C20C22 (11) β C20C22C21 (19)
68	942.27	926.25	36.04	τ H37C26C27C28 (15) τ H39C28C29C31 (22)
67	928.22	912.44	87.78	τ H47C23C20C19 (46) τ H48C23C20C19 (35)
66	923.13	907.44	2.37	τ H37C26C27C28 (26) τ H39C28C29C31 (26)
65	921.08	905.43	40.50	τ H40C30C29C31 (56)
64	901.59	886.26	57.35	ν C21-C17 (15) τ H35C24C25C26 (11)
63	888.54	873.44	106.95	τ H40C30C29C31 (20)
62	831.61	817.48	6.67	τ H16C6N7C8 (82) τ C8N7C6N5 (10)
61	823.94	809.93	11.58	τ H43C18C19C20 (32) τ H46C19C20C22 (10) τ H48C23C20C19 (11)
60	819.47	805.53	4.16	τ H38C27C28C29 (23) τ H39C28C29C31 (11) τ C28C29C30C25 (10)
59	813.94	800.10	0.73	τ H44C21C22C20 (31) τ H45C22C21C17 (12)
58	796.96	783.41	4.52	τ C9C8N7C6 (13) γ O12N13C8C11 (54) γ C11C9N7C8 (20)
57	785.86	772.50	3.07	ν C23-C20 (10) ν C19-C20 (34) ν C20-C22 (30)
56	768.16	755.10	4.66	τ H39C28C29C31 (11)
55	750.79	738.02	17.95	γ O10N3N5C4 (71)
54	744.16	731.51	10.91	γ O10N3N5C4 (10)
53	734.09	721.61	3.60	ν S34-C33 (10) β C19C20C22 (11)
52	721.03	708.77	61.92	τ H37C26C27C28 (14) τ C26C27C28C29 (14) τ C27C28C29C30 (10) γ C31C28C30C29 (13)
51	700.95	689.03	13.25	ν N1-C9 (24) ν N7-C8 (15) β C9C8N7 (12)
50	698.37	686.49	2.28	τ C9C8N7C6 (21) τ N3N2N1C9 (11) γ O12N13C8C11 (17) γ N1N5C8C9 (22)
49	692.55	680.78	4.63	τ H45C22C21C17 (10) τ H47C23C20C19 (30) τ H48C23C20C19 (32)
48	685.87	674.21	22.04	ν N32-C31 (10) ν S34-C33 (17) τ C26C27C28C29 (11)
47	667.23	655.89	86.24	ν C11-C8 (10) β O10C4N5 (15) β O12C11N13 (21)
46	665.47	654.16	12.60	τ H16C6N7C8 (11) τ C8N7C6N5 (53)
45	626.18	615.54	23.85	β C20C22C21 (14)

44	608.19	597.85	3.80	β C18C19C20 (10) β C20C22C21 (12)
43	606.88	596.57	5.01	β C22C21C17 (12) β C20C22C21 (14)
42	595.85	585.72	6.17	ψ N3-N2 (15) β O12C11N13 (10)
41	589.08	579.06	3.41	τ H14N13C11C8 (34) τ H15N13C11C8 (37) τ C8N7C6N5 (14)
40	565.22	555.61	25.26	ψ N3-N2 (26) β O12C11N13 (14) β N3N2N1 (14)
39	547.66	538.35	2.44	τ C9C8N7C6 (25) τ N3N2N1C9 (19)
38	536.58	527.46	9.13	β C19C20C22 (12)
37	525.03	516.10	12.07	β C4N3N2 (10) γ C23C19C22C20 (11)
36	491.03	482.68	13.55	β S34C33N32 (50)
35	473.70	465.64	6.19	τ C22C21C17C24 (10) τ C19C20C22C21 (17)
34	469.92	461.93	18.06	β S34C33N32 (26)
33	461.59	453.74	3.71	τ C18C19C20C22 (10) τ C22C21C17C24 (10) τ C19C20C22C21 (17) τ C20C22C21C17 (17)
32	450.43	442.77	2.91	τ S34C33N32C31 (83)
31	437.92	430.48	2.55	τ C26C27C28C29 (20) τ C28C29C30C25 (14)
30	417.15	410.06	0.15	β C22C21C17 (12) β C23C20C22 (18) γ C21C24N3C17 (19)
29	391.10	384.45	0.05	β C30C25C24 (31) β C31C29C30 (25)
28	367.94	361.68	16.11	ψ C11-C8 (11) ψ N3-C17 (10) β N13C11C8 (20)
27	336.65	330.93	0.56	β C23C20C22 (16) β C24C17N3 (14)
26	324.69	319.17	7.35	β O10C4N5 (23) β N1C9C8 (23)
25	316.80	311.42	8.49	β C23C20C22 (10) β C31C29C30 (10)
24	305.82	300.62	1.50	β N32C31C29 (12) τ C27C28C29C30 (11)
23	304.72	299.54	0.61	β C23C20C22 (10) β N32C31C29 (11)
22	289.26	284.34	191.86	τ H14N13C11C8 (40) τ H15N13C11C8 (38)
21	270.68	266.08	3.46	β C31C29C30 (20) β C17N3N2 (11)
20	230.46	226.54	7.18	τ N1N5C8C9 (50)

19	222.89	219.10	3.74	ν N3-C17 (12) τ C29C30C25C24 (15)
18	219.36	215.63	11.16	τ N2N1C9N5 (17) τ N3N2N1C9 (13) γ C11C9N7C8 (38)
17	193.49	190.20	1.40	β C21C17C24 (13) τ C19C20C22C21 (16) γ C23C19C22C20 (20)
16	188.41	185.20	5.45	β C30C25C24 (15) β C21C17C24 (19)
15	162.99	160.22	2.15	τ C20C22C21C17 (10) γ C4C17N2N3 (21)
14	155.37	152.73	3.75	γ C31C28C30C29 (21) γ C4C17N2N3 (10)
13	125.83	123.69	3.45	β C11C8N7 (12) β C24C17N3 (10) γ C4C17N2N3 (15)
12	105.69	103.90	2.42	β N1C9C8 (11) β C11C8N7 (28) β C17N3N2 (19)
11	96.26	94.62	0.23	τ C29C30C25C24 (14) τ N3N2N1C9 (11) τ C17N3N2N1 (10) γ C4C17N2N3 (11)
10	88.48	86.98	11.11	β C33N32C31 (66)
9	75.28	74.00	0.55	τ N2N1C9N5 (24) τ C29C30C25C24 (11) γ C11C9N7C8 (13)
8	53.48	52.57	0.19	τ N13C11C8C9 (47) τ C24C17N3N2 (20)
7	43.13	42.39	2.36	τ C30C25C24C17 (11) τ N13C11C8C9 (32)
6	32.50	31.95	0.51	β C25C24C17 (13) τ C22C21C17C24 (16) τ C29C30C25C24 (10) τ C25C24C17N3 (17)
5	28.05	27.57	1.97	τ C33N32C31C29 (10) τ C22C21C17C24 (27) τ C24C17N3N2 (25)
4	24.31	23.90	0.25	τ C33N32C31C29 (36) τ C17N3N2N1 (19)
3	21.01	20.65	0.29	τ C30C25C24C17 (24) τ C24C17N3N2 (28) τ C17N3N2N1 (11)
2	13.06	12.84	0.40	τ C30C25C24C17 (15) τ N32C31C29C28 (29) τ C25C24C17N3 (32)
1	6.10	5.99	0.24	τ C30C25C24C17 (11) τ N32C31C29C28 (53) τ C25C24C17N3 (25)

Symbol for stretching here: stretching (a = antisymmetric; s = symmetric); β = deformation in the plane; γ = deformation out of the plane; τ = torsion; β R = deformation ring; τ R = torsion ring; τ w=twisting; δ =deformation; and R=Ring

4.6 Conclusion

All the structure under investigation for TMZ and its BITC derivatives has been optimized at DFT/B3LYP/6-311++G(d,p) level of theory. The molecules possess non-planar structure having co-planar ring. The spectroscopic FT-IR studies as well as UV-visible spectral analysis was performed for calculating electronic properties. The Optimized minimum energy suggest that aqueous solution are more stable than the gas phase. The stability order of the optimized order can be summarized as TMZ-BITC(2) > TMZ-BITC(3) > TMZ-BITC(4) > TMZ-BITC(1). The calculated atomic charges and MEP studies suggest that O-atom is identified as region of nucleophilic attack and H-atom of amine group, the region of electrophilic attack. The ^1H and ^{13}C NMR calculations was performed by GIAO (Gauge-Independent Atomic Orbital) method at the B3LYP/6-311++G(d,p) basis set in DMSO solvent.

The intramolecular hydrogen bonding is confirmed by the behavior of the two charges discussed for both media. NBO analysis showed the intramolecular charge transfer within the molecule was primarily from the lone pairs of the electron in N-atom and O-atom. Furthermore, global reactivity descriptors of the structures in both media were determined using FMO and HOMO-LUMO analysis, indicating the molecule's bioactivity and stability.

5 PHARMACOLOGICAL AND MOLECULAR DOCKING INVESTIGATIONS

5.1 Molecular Docking study

The TMZ and its derivatives were considered as a ligand which is docked with the crystal structure of the target protein complex PDB ID: IQH4 (Eder *et al.*, 2008) that was retrieved from the Protein Data Bank (www.rcsb.org/pdb). After which the docking score and interaction of protein-ligand is being examined.

5.1.1 Ligand preparation:

Using the Gaussian16 at approximation level of B3LYP/6311++G(d,p), the optimized structure were subsequently converted to pdb format and then to the pdbqt format using AutoDock Tools (ADT).

5.1.2 Protein preparation:

The crystal structure of complex (brain-type creatine kinase),PDB ID: IQH4 was downloaded from the PDB bank. The complex contains two chains (A and B), where chain B was removed. Water molecule was also removed and kollman charges and polar hydrogen was added, and saved to pdbqt for AutoDock vina using AutoDock Tools (ADT).

5.1.3 Protein-ligand docking:

The Autodock Vina was used for virtual screening of protein-ligand binding. The size of grid box was set with dimensional of 25, 25, 25 for x, y, z coordinates. Config.txt file was created including all necessary informations. The results were then visualized in Discovery Studio 2020.

5.1.4 Analysis of interactions between ligands and protein

TMZ and its BITC derivatives were docked in active site of target complex protein (PDB ID: IQH4). 3D picture of the protein is shown in **Figure 5.1**. Target complex was prepared for docking studies after energy minimization and protonation. Out of 10 poses protein-ligand interactions, the pose with high score

binding energy value for each ligand was chosen for analyzing the ligand-protein interactions.

Figure 5.2 to **Figure 5.6** displays the molecular binding mode of TMZ and its BITC derivatives at the binding site of IQH4. **Table 5.1** presented the binding energy score of ligand-protein interactions along with residues involving hydrogen bonds and Pi-Cation, Pi-Alkyl, Pi-anion bonding between the amino acids residues and ligands. Out of the five compounds where each docking gives nine conformations, TMZ-BITC(3)-protein docking interactions shows the highest binding energy of -8.6 kcal/mol.

Four hydrogen bond interactions were observed in the IQH4-TMZ complex with docking energy of -5.8 kcal/mol. Amino acids, ARG96 and GLU232 formed Conventional H-bond with the hydrogen of imidazole and amine group. The other two amino acid residues, GLY73 and VAL72 formed Conventional H-bonds, and THR71 formed C-H bond with the O atom of carbazide group. Two hydrogen bond interactions were observed in the IQH4-TMZ-BITC(1) complex with docking energy of -7.1 kcal/mol. Amino acids, ARG96 formed Conventional H-bond with the O of carboazide group and GLU with the S of NCS group. The other two amino acid residues SER285 and CYS283 formed C-H bonds and Vander Walls bond with the ligands.

Four hydrogen bond interactions were observed in the IQH4-TMZ-BITC(2) complex with docking energy of -7.8 kcal/mol. Amino acids, GLN318 formed two Conventional H-bonds with the hydrogens of imidazole and amine groups. The other two amino acid residues ARG320 and ARG341 formed C-H bonds with the O-atom of carbazide group.

Five hydrogen bond interactions were observed in the IQH4-TMZ-BITC(3) complex with docking energy of -8.6 kcal/mol which is the lowest binding energy among the Protein-ligand interactions. Amino acids, ARG132 and ASN286 formed three Conventional H-bonds with the hydrogen of tetrazine ring and carbazide group, and GLU232 with amine and NCS groups.

Two hydrogen bond interactions were observed in the IQH4-TMZ-BITC(4) complex with docking energy of -7.2 kcal/mol. Amino acids, ARG320 and ASN286

formed Conventional H-bond with the O-atom of tetrazine ring and amine groups respectively.

Table 5.1: Binding energy and hydrogen bond distance parameter for TMZ and its derivatives on binding with IQH4 protein.

Inhibitor	Binding energy (kcal/mol)	Residues involved in H-bond	Residues involved in other interaction(Alkyl, Pi-Cation, Pi-Alkyl, Pi-anion, Pi-Pi stacked, Pi Sulphur)
TMZ	-5.8	LEU201, THR59, VAL72, GLY73	THR71, CYS283, LEU201
TMZ-BITC(1)	-7.1	ARG96, GLU232	CYS283, VAL75, SER285, CTS74, LEU201, CYS283
TMZ-BITC(2)	-7.8	GLN318, ARG320, ARG341,	ARG292, LEU201, CYS283, VAL72
TMZ-BITC(3)	-8.6	GLU232, ARG132, ASN286	CYS283, VAL72, LEU201
TMZ-BITC(4)	-7.2	ARG320, ASN286	ILE238, TRP228, ARG132, ARG236

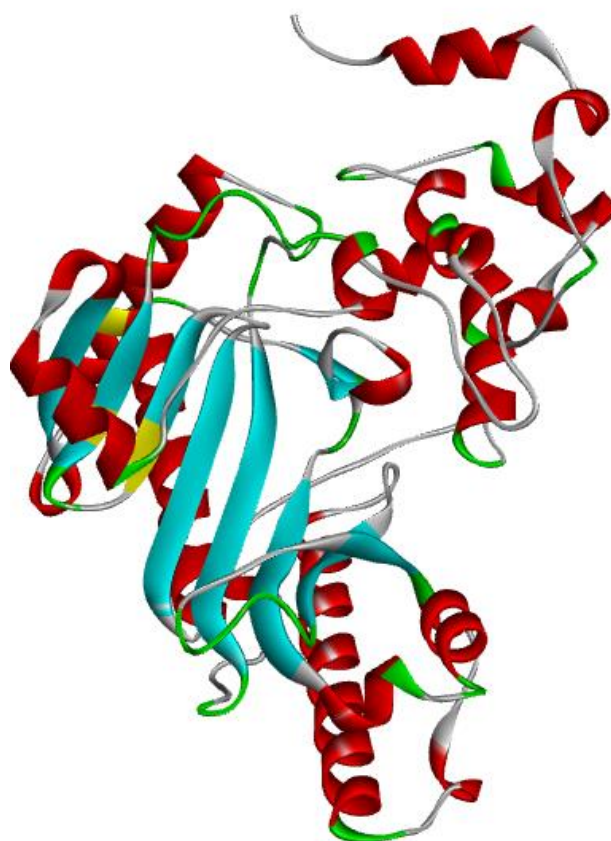


Figure 5.1: 3D Structure of target protein complex PDB ID: IQH4 from PDB Bank

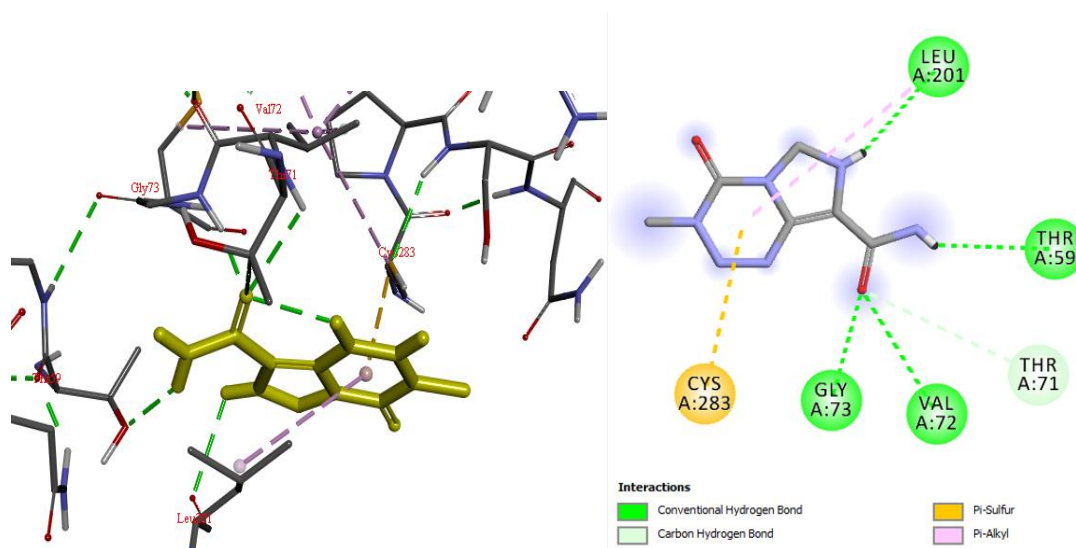


Figure 5.2: 3D and 2D binding mode of compound TMZ in the active site cavity of IQH4 protein.

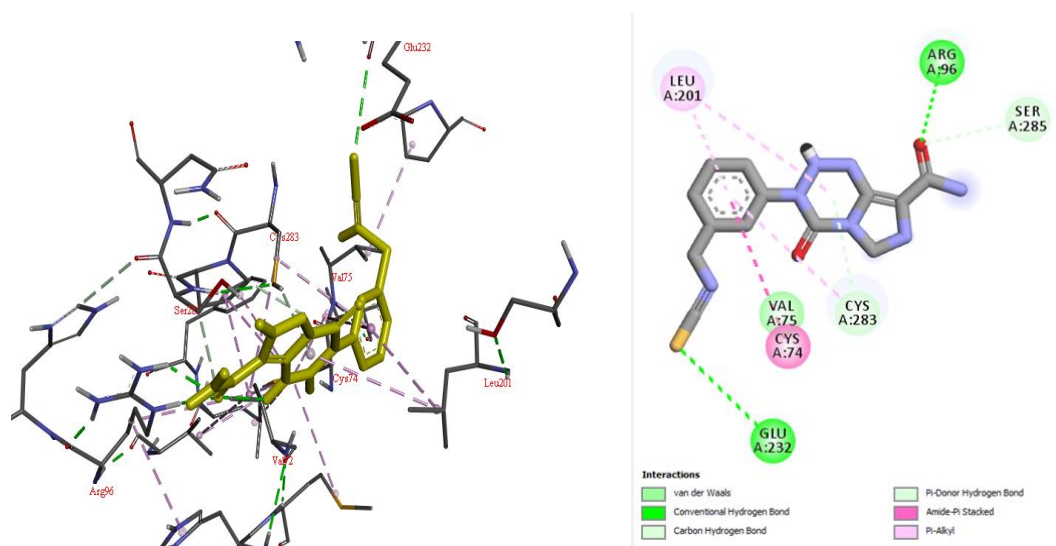


Figure 5.3: 3D and 2D binding mode of compound TMZ-BITC(1) in the active site cavity of IQH4 protein.

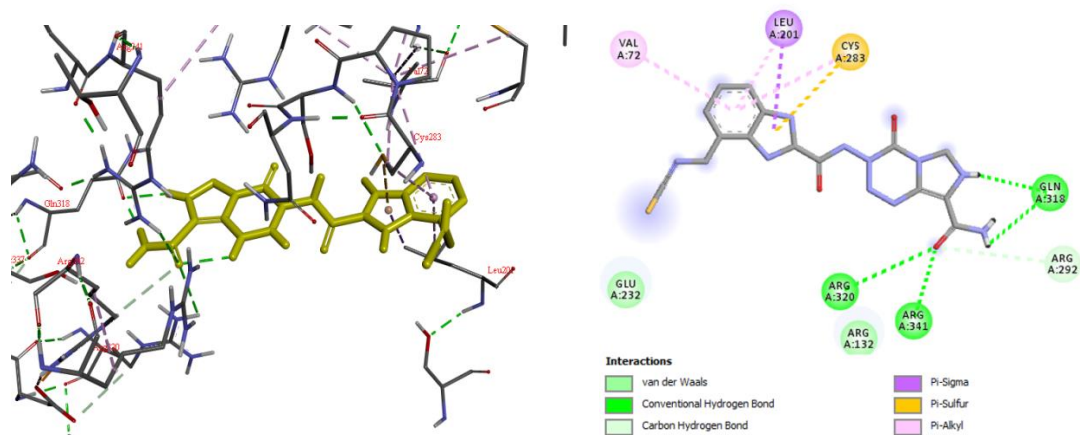


Figure 5.4: 3D and 2D binding mode of compound TMZ-BITC(2) in the active site cavity of IQH4 protein.

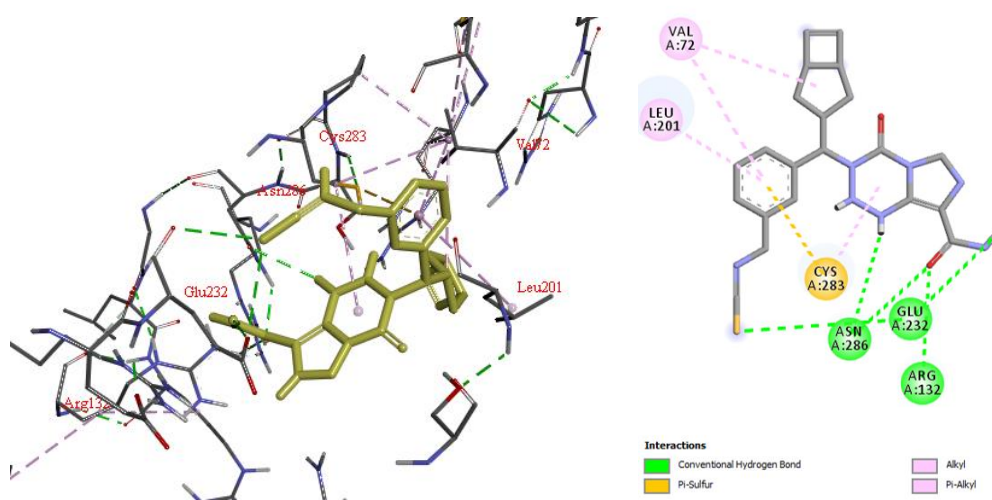


Figure 5.5: 3D and 2D binding mode of compound TMZ-BITC(3) in the active site cavity of IQH4 protein.

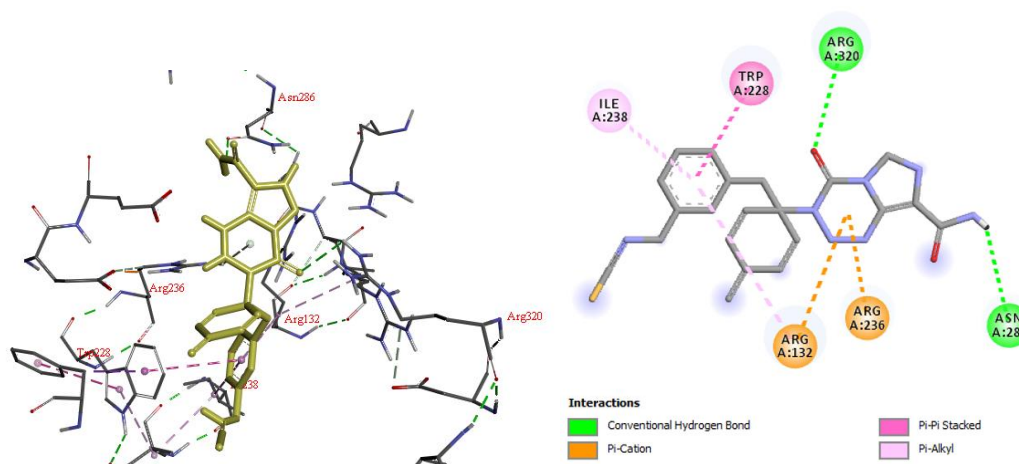


Figure 5.6: 3D and 2D binding mode of compound TMZ-BITC(4) in the active site cavity of IQH4 protein.

5.1 PASS biological activity prediction

The free web resource PASS Online is designed to predict the biological activity spectra of organic compounds based on their structural formulas for over 4000 types of biological activity with an average accuracy of more than 95% (<http://www.way2drug.com/passonline>). The prediction is analyzed on the basis of the structure-activity interactions in the training set, which contains data on the structure and biological activity of over 300,000 organic molecules (Filimonov *et al.*, 2014).

Evaluation of the pharmacological activity of TMZ and its BITC derivatives was performed using online services CLC-Pred database. As an initial information, the structural formula of the substance in MOL or SDF file formats were used to obtain prediction data in the program.

The predicted activity spectrum of a substance is estimated by PASS Software as probable activity (Pa) and probable inactivity (Pi) values. If Pa is greater than 0.7, the chance of experimental pharmacological effect is greater; if Pa is less than 0.7, the probability is lower. If Pa = 0.5, the probability of discovering the activity, experimentally is very low, but which may suggest discovering of a novel compound. **Table 5.2** shows the projected biological activity findings with $P_a > 0.7$ for the studied substances derived from the PASS online software.

Analysis of prediction data for the structures of TMZ and its BITC derivatives showed that the most probable activity of the studied compounds are Apoptosis agonist and Antineoplastic. These in silico prediction results highlighted the potential of these compounds against cancer cells lines. The pa values obtained for activity of apoptosis on TMZ is 0.960, 0.933 for TMZ-BITC(1), 0.936 for TMZ-BITC(2), 0.917 for TMZ-BITC(3) and 0.913 for TMZ-BITC(4). All the derivatives showed significant pa values ($p_a > 0.9$) as in the case of TMZ. Hence, these compounds are suggestive of having potency for anticancer drug.

Table 5.2: In silico PASS prediction of studied compounds obtained through Pass online tool

Compound	Pa	Pi	Activity
TMZ	0.960	0.003	Apoptosis agonist
	0.910	0.004	Angiogenesis inhibitor
	0.849	0.007	Antineoplastic
	0.703	0.011	Nucleoside oxidase (H ₂ O ₂ -forming) inhibitor
	0.655	0.004	Leukopoiesis inhibitor
TMZ-BITC(1)	0.933	0.004	Apoptosis agonist
	0.781	0.014	Antineoplastic
	0.507	0.019	Angiogenesis inhibitor
	0.462	0.006	Antineoplastic (lymphocytic leukemia)
	0.439	0.017	Adenosine regulator
TMZ-BITC(2)	0.936	0.004	Apoptosis agonist
	0.769	0.016	Antineoplastic
	0.576	0.012	Angiogenesis inhibitor
	0.379	0.023	Adenosine regulator
	0.329	0.018	Antineoplastic (brain cancer)
TMZ-BITC(3)	0.917	0.004	Apoptosis agonist
	0.602	0.045	Antineoplastic
	0.551	0.110	Antieczematic
	0.353	0.027	Adenosine regulator
	0.338	0.015	Antineoplastic (small cell lung cancer)
TMZ-BITC(4)	0.913	0.004	Apoptosis agonist
	0.724	0.022	Antineoplastic
	0.392	0.024	Chemoprotective
	0.375	0.024	Adenosine regulator
	0.390	0.040	Angiogenesis inhibitor

5.2 **In silico ADMET prediction**

ADMET properties (Absorption, distribution, metabolism, excretion, and Toxicity) of the title compounds are predicted to determine the drug activity inside the body. For this purpose, the title molecules were provided in mol format and their in silico ADME properties were evaluated using the online PreADMET server. Besides, the physicochemical properties (lipophilicity and water solubility), drug-likeness and bio-availability scores of these compounds were also estimated through the SwissADME on line tool. The in silico ADMET prediction of Drug-likeness and Toxicity of TMZ and its BITC derivatives are shown in **Table 5.3**.

Human intestinal absorption (HIA) is a very important process that determines the absorption of orally administered drugs from the intestine into the blood stream. Some studies have shown that values range from 75% -100% indicate good human intestinal absorption. Theoretical prediction of HIA manifests that the title compounds for TMZ-BITC(1) is 91.05 %, TMZ-BITC(2) is 69.7 %, TMZ-BITC(3) is 99.14 % and TMZ-BITC(4) is 95.79 %. All the TMZ-BITC derivatives have good human intestinal absorption ability than that of the TMZ compounds (64.65%) alone.

The skin permeability (SP) is a significant parameter for the assessment of transdermal delivery of drugs. The more negative the value of log K_p, the less the skin permeability for the molecule. In the present study, the skin permeability results showed that the TMZ-BITC derivatives are more skin permeable than the TMZ, except TMZ-BITC(2). Moreover, among the title compounds TMZ-BITC(3) shows higher Caco-2 cell permeability, showing lower MDCK cell permeability.

Plasma protein binding (PPB) is an important ADME property that refers to the degree to which drugs attach to proteins within the blood. If the drug is less bounded, the more efficiently it can penetrate tissues enhancing the rate of the excretion too. The theoretical prediction of PPB value is 58.35 % for TMZ, 79.92 % for TMZ-BITC(1), 81.31 % for TMZ-BITC(2), 92.42 % for TMZ-BITC(3) and 90.46 % for TMZ-BITC(4), which demonstrates that these compounds are weakly bounded enabling the capability of diffusing across cell membranes. All the TMZ-BITC derivatives compound shows high PPB than TMZ which means they cannot be unbound from plasma protein.

Table 5.3: In silico ADMET prediction of Drug-likeness and Toxicity of TMZ and its BITC derivatives.

ADME properties/physiochemical properties/drug-likeness		TMZ	TMZ-BITC(1)	TMZ-BITC(2)	TMZ-BITC(3)	TMZ-BITC(4)
ADME properties	Human intestinal absorption (HIA, %)	64.65	91.05	69.70	99.14	95.79
	<i>In-vitro</i> Caco-2 cell permeability (nm/sec)	20.07	21.01	20.95	21.06	20.75
	<i>In-vitro</i> MDCK cell permeability (nm/sec)	1.77	8.19	0.57	0.05	0.12
	<i>In-vitro</i> skin permeability (logKp, cm/hour)	-4.28	-4.12	-5.03	-3.25	-3.08
	<i>In-vitro</i> plasma protein binding (%)	58.35	79.92	81.31	92.42	90.46
	Blood-brain barrier penetration(BBB)(C. brain/C.blood)	0.11	0.07	0.04	0.31	0.11
Toxicity	Carcinogenicity (Mouse)	negative	positive	negative	positive	positive
	Carcinogenicity (Rat)	positive	negative	positive	negative	positive
	Ames test	mutagen	mutagen	mutagen	mutagen	non-mutagen
Water solubility	(Log S)	Very soluble	Soluble	Soluble	Moderately soluble	Soluble
Drug-likeness	Lipinski,s rules	Yes	Yes	No	Yes	Yes
	Bioavailability Score	0.55	0.55	0.55	0.55	0.55

The Blood brain barrier (BBB) is a unique assembly of blood vessels that prevents solutes in the circulating blood to enter into the central nervous system (CNS). Hence, while developing drugs targeting CNS, it is essential to ensure that the drugs cross-over the BBB. TMZ has 0.11 BBB, TMZ-BITC(1) has 0.07 BBB, TMZ-BITC(2) has 0.04 BBB, TMZ-BITC(3) has 0.31 BBB and TMZ-BITC(4) has 0.11 BBB. The theoretical prediction for blood brain barrier penetration shows that TMZ-BITC(3) have higher BBB penetration than the other compounds.

The Ames mutagenicity test shows that the title compounds are mutagenic except for TMZ-BITC(4). TMZ and TMZ-BITC(2) shows no risk of carcinogenicity in mouse, and TMZ-BITC(1) and TMZ-BITC(3) shows no risk of carcinogenicity in rat. However, TMZ-BITC(4) shows both carcinogenicity in mouse and rat.

In addition, the theoretical drug-likeness predictions carried out with respect to the selected Lipinski, and the bioavailability score was also detected using the SwissADME web tool. The screening process done with Lipinski Rule of Five showed that except for TMZ-BITC(2), all the compounds follows Lipinski Rule of Five.

5.3 Conclusion

Molecular docking study has established good inhibitory nature of the studied compounds against target complex protein (PDB ID: IQH4). Molecular docking studies revealed that the TMZ-BITC(3) with lesser binding energy of -8.6 kcal/mol has better inhibitor effects than TMZ and its derivatives having five conventional hydrogen bondings in the protein-ligand interactions. The *in silico* biological activity results predicted using the PASS and CLC-Pred database suggested that all the compounds possess anticancer activity mostly of apoptosis ($pa > 0.9$) and antineoplastic ($pa > 0.7$). *In silico* ADME prediction showed that TMZ-BITC(3) shows better pharmacokinetics properties like intestinal absorption, blood-brain barrier permeability, skin permeability, Plasma protein binding blood brain barrier and mutagenic effect amongst the others compounds. The evaluation of five rules of Lipinski for the compounds revealed that all the compounds fulfills all the five rules except for TMZ-BITC(2). The theoretical conceptual study may suggest TMZ-BITC(3) compound for verification at the clinical level drug examinations for a probable potency as an effective anticancer drug.

6 SUMMARY AND CONCLUSION

Glioblastoma (GBM) is the most severe primary brain tumor. Currently, frontline treatment for primary GBM comprises the DNA-methylating medication temozolomide (TMZ, of the imidazotetrazine family), whereas the appropriate treatment for recurrent GBM remains under research. Despite its wide usage, a majority of GBM patients do not react to TMZ therapy; expression of the O⁶-methylguanine DNA methyltransferase (MGMT) enzyme and lack of mismatch repair (MMR) serve as the key clinical routes of resistance to TMZ. This study deals with the electronic and spectroscopic study of selected TMZ-BITC derivatives along with the TMZ with the help of DFT theory

All the structure under study for TMZ and its BITC derivatives has been optimized at DFT/B3LYP/6-311++G(d,p) level of theory. All the molecules exhibit non-planar structure having co-planar ring. The experimental data and theoretical data of TMZ are well established at this DFT level of study. The spectroscopic FT-IR studies as well as UV-visible spectrum analysis was done for calculating electronic characteristics. The Optimized minimum energy implies that aqueous solution are more stable than the gas phase. The stability order of the optimized order may be stated as TMZ-BITC(2) > TMZ-BITC(3) > TMZ-BITC(4) > TMZ-BITC(1) (1). The computed atomic charges and MEP analyses reveal that O-atom is classified as region of nucleophilic attack and H-atom of amine group, the region of electrophilic attack. The theoretical and experimental chemical shifts of TMZ showed comparable values to each other.

The intramolecular hydrogen bonding is confirmed by the behavior of the two charges stated for both media. NBO analysis indicated the intramolecular charge transfer inside the molecule came predominantly from the lone pairs of the electron in N-atom and O-atom. Furthermore, global reactivity descriptors of the structures in both media were assessed using FMO and HOMO-LUMO analyses, showing the molecule's bioactivity and stability.

Lastly, Molecular docking studies of selected compounds with the protein (PDB ID: IQH4) revealed that the TMZ-BITC(3) with the lowest binding energy of -8.6 kcal/mol has better inhibitor effects than TMZ and its derivatives. The *in silico* biological activity results predicted using the PASS and CLC-Pred database suggested that all the compounds possess anticancer activity. *In silico* ADME prediction showed that TMZ-BITC(3) shows better pharmacokinetics properties like intestinal absorption, blood-brain barrier permeability, skin permeability, Plasma protein binding blood brain barrier and mutagenic effect amongst the others compounds.

7 REFERENCES

- Anderson, A. C. (2003). The Process of Structure-Based Drug Design. *Chemistry & Biology*, 10(9), 787–797. <https://doi.org/10.1016/j.chembiol.2003.09.002>
- Arora, A., & Somasundaram, K. (2019). Glioblastoma vs temozolomide: Can the red queen race be won? *Cancer Biology & Therapy*, 20(8), 1083–1090. <https://doi.org/10.1080/15384047.2019.1599662>
- Arrowsmith, J., Jennings, S. A., Clark, A. S., & Stevens, M. F. (2002). Antitumor imidazotetrazines. 41. Conjugation of the antitumor agents mitozolomide and temozolomide to peptides and lexitropsins bearing DNA major and minor groove-binding structural motifs. *Journal of Medicinal Chemistry*, 45(25), 5458–5470.
- Babu, N. J., Reddy, L. S., Aitipamula, S., & Nangia, A. (2008). *CCDC 665062: Experimental Crystal Structure Determination* [CIF]. Cambridge Crystallographic Data Centre. <https://doi.org/10.5517/CCQB1MP>
- Bolly, H. M. B., Faried, A., Hermanto, Y., Lubis, B. P., Tjahjono, F. P., Hernowo, B. S., & Arifin, M. Z. (2021). Analysis of Mutant Isocitrate Dehydrogenase 1 Immunoexpression, Ki-67 and Programmed Death Ligand 1 in Diffuse Astrocytic Tumours: Study of Single Center in Bandung, Indonesia. *Journal of Korean Neurosurgical Society*, 64(1), 100.
- Clark, A. S., Deans, B., Stevens, M. F. G., Tisdale, M. J., Wheelhouse, R. T., Denny, B. J., & Hartley, J. A. (1995). Antitumor imidazotetrazines. 32.1 synthesis of novel imidazotetrazinones and related bicyclic heterocycles to probe the

- mode of action of the antitumor drug temozolomide. *Journal of Medicinal Chemistry*, 38(9), 1493–1504.
- Cortes, E., Márquez, E., Mora, J. R., Puello, E., Rangel, N., De Moya, A., & Trilleras, J. (2019). Theoretical Study of the Adsorption Process of Antimalarial Drugs into Acrylamide-Base Hydrogel Model Using DFT Methods: The First Approach to the Rational Design of a Controlled Drug Delivery System. *Processes*, 7(7), 396. <https://doi.org/10.3390/pr7070396>
- Dahl, J. P., & Avery, J. (2013). *Local density approximations in quantum chemistry and solid state physics*. Springer Science & Business Media.
- Darkes, M. J., Plosker, G. L., & Jarvis, B. (2002). Temozolomide. *American Journal of Cancer*, 1(1), 55–80.
- Delgado-López, P. D., & Corrales-García, E. M. (2016). Survival in glioblastoma: A review on the impact of treatment modalities. *Clinical and Translational Oncology*, 18(11), 1062–1071. <https://doi.org/10.1007/s12094-016-1497-x>
- Denny, B. J., Wheelhouse, R. T., Stevens, M. F., Tsang, L. L., & Slack, J. A. (1994). NMR and molecular modeling investigation of the mechanism of activation of the antitumor drug temozolomide and its interaction with DNA. *Biochemistry*, 33(31), 9045–9051.
- Diehl, C., Schwendner, M., Sollmann, N., Oechsner, M., Meyer, B., Combs, S., & Krieg, S. (2018). RTHP-33. APPLICATION OF PRESURGICAL NAVIGATED TRANSCRANIAL MAGNETIC STIMULATION MOTOR MAPPING FOR ADJUVANT RADIOTHERAPY TREATMENT PLANNING IN PATIENTS WITH BRAIN TUMORS. *Neuro-Oncology*, 20(suppl_6), vi232–vi232. <https://doi.org/10.1093/neuonc/noy148.963>

- Dunning Jr, T. H., & Hay, P. J. (1976). *Modern theoretical chemistry*.
- Eder, M., Schlattner, U., Wallimann, T., Becker, A., Kabsch, W., & Fritz-Wolf, K. (2008). Crystal structure of brain-type creatine kinase at 1.41 Å resolution. *Protein Science*, 8(11), 2258–2269. <https://doi.org/10.1110/ps.8.11.2258>
- Esteller, M., Garcia-Foncillas, J., Andion, E., Goodman, S. N., Hidalgo, O. F., Vanaclocha, V., Baylin, S. B., & Herman, J. G. (2000). Inactivation of the DNA-repair gene MGMT and the clinical response of gliomas to alkylating agents. *New England Journal of Medicine*, 343(19), 1350–1354.
- F Sousa, S., MFSA Cerqueira, N., A Fernandes, P., & Joao Ramos, M. (2010). Virtual screening in drug design and development. *Combinatorial Chemistry & High Throughput Screening*, 13(5), 442–453.
- Filimonov, D. A., Lagunin, A. A., Glorizova, T. A., Rudik, A. V., Druzhilovskii, D. S., Pogodin, P. V., & Poroikov, V. V. (2014). Prediction of the Biological Activity Spectra of Organic Compounds Using the Pass Online Web Resource. *Chemistry of Heterocyclic Compounds*, 50(3), 444–457. <https://doi.org/10.1007/s10593-014-1496-1>
- Friedman, H. S., Kerby, T., & Calvert, H. (2000a). Temozolomide and treatment of malignant glioma. *Clinical Cancer Research*, 6(7), 2585–2597.
- Friedman, H. S., Kerby, T., & Calvert, H. (2000b). Temozolomide and Treatment of Malignant Glioma1. *Clinical Cancer Research*, 6(7), 2585–2597.
- Friedman, H. S., McLendon, R. E., Kerby, T., Dugan, M., Bigner, S. H., Henry, A. J., Ashley, D. M., Krischer, J., Lovell, S., & Rasheed, K. (1998). DNA mismatch repair and O6-alkylguanine-DNA alkyltransferase analysis and

- response to Temodal in newly diagnosed malignant glioma. *Journal of Clinical Oncology*, *16*(12), 3851–3857.
- Frisch, A., Nielson, A. B., & Holder, A. J. (2000). Gaussview user manual. *Gaussian Inc., Pittsburgh, PA*, 556.
- Frisch, M. J., Pople, J. A., & Binkley, J. S. (1984). Self-consistent molecular orbital methods 25. Supplementary functions for Gaussian basis sets. *The Journal of Chemical Physics*, *80*(7), 3265–3269. <https://doi.org/10.1063/1.447079>
- Furukawa, R., Homma, H., Inoue, T., Horiuchi, H., & Usui, K. (2018). Cytomegalovirus Hemorrhagic Cystitis in a Malignant Glioma Patient Treated with Temozolomide. *Internal Medicine*, *57*(20), 3047–3050. <https://doi.org/10.2169/internalmedicine.1005-18>
- Gibson, N. W., Hickman, J. A., & Erickson, L. C. (1984). DNA cross-linking and cytotoxicity in normal and transformed human cells treated in vitro with 8-carbamoyl-3-(2-chloroethyl) imidazo [5, 1-d]-1, 2, 3, 5-tetrazin-4 (3H)-one. *Cancer Research*, *44*(5), 1772–1775.
- Gilbert, D. (2004). Bioinformatics software resources. *Briefings in Bioinformatics*, *5*(3), 300–304. <https://doi.org/10.1093/bib/5.3.300>
- Gjika, E., Pal-Ghosh, S., Kirschner, M. E., Lin, L., Sherman, J. H., Stepp, M. A., & Keidar, M. (2020). Combination therapy of cold atmospheric plasma (CAP) with temozolomide in the treatment of U87MG glioblastoma cells. *Scientific Reports*, *10*(1), 16495. <https://doi.org/10.1038/s41598-020-73457-7>
- Glendening, E. D., & Weinhold, F. (1998). Natural resonance theory: I. General formalism. *Journal of Computational Chemistry*, *19*(6), 593–609.

- Graziani, G., Faraoni, I., Grohmann, U., Bianchi, R., Binaglia, L., Margison, G. P., Watson, A. J., Orlando, L., Bonmassar, E., & D'Atri, S. (1995). O6-alkylguanine-DNA alkyltransferase attenuates triazene-induced cytotoxicity and tumor cell immunogenicity in murine L1210 leukemia. *Cancer Research*, *55*(24), 6231–6236.
- Hehre, W. J., & Radom, L. (1986). P. v R. Schleyer and JA Pople, Ab initio Molecular Orbital Theory. In *John Wiley and Sons*.
- Heo, L., Shin, W.-H., Lee, M. S., & Seok, C. (2014). GalaxySite: Ligand-binding-site prediction by using molecular docking. *Nucleic Acids Research*, *42*(W1), W210–W214.
- Hickman, J. A., Stevens, M. F., Gibson, N. W., Langdon, S. P., Fizames, C., Lavelle, F., Atassi, G., Lunt, E., & Tilson, R. M. (1985). Experimental antitumor activity against murine tumor model systems of 8-carbamoyl-3-(2-chloroethyl) imidazo [5, 1-d]-1, 2, 3, 5-tetrazin-4 (3H)-one (mitozolomide), a novel broad-spectrum agent. *Cancer Research*, *45*(7), 3008–3013.
- Hohenberg, P., & Kohn, W. (1964). Inhomogeneous Electron Gas. *Physical Review*, *136*(3B), B864–B871. <https://doi.org/10.1103/PhysRev.136.B864>
- Jensen, F. (2017). *Introduction to computational chemistry*. John wiley & sons.
- Jiang, T., Nam, D.-H., Ram, Z., Poon, W., Wang, J., Boldbaatar, D., Mao, Y., Ma, W., Mao, Q., You, Y., Jiang, C., Yang, X., Kang, C., Qiu, X., Li, W., Li, S., Chen, L., Li, X., Liu, Z., ... Wang, Q. (2021). Clinical practice guidelines for the management of adult diffuse gliomas. *Cancer Letters*, *499*, 60–72. <https://doi.org/10.1016/j.canlet.2020.10.050>

- Karran, P., & Hampson, R. (1996). Genomic instability and tolerance to alkylating agents. *Cancer Surveys*, 28, 69–85.
- Kassal, I., & Aspuru-Guzik, A. (2009). Quantum algorithm for molecular properties and geometry optimization. *The Journal of Chemical Physics*, 131(22), 224102. <https://doi.org/10.1063/1.3266959>
- Kohn, W., & Sham, L. J. (1965). Self-Consistent Equations Including Exchange and Correlation Effects. *Physical Review*, 140(4A), A1133–A1138. <https://doi.org/10.1103/PhysRev.140.A1133>
- Koopman, T. (1934). On the assignment of wave functions and eigenvalues to the individual electrons of an atom. *Physica*, 104–113.
- Krishnan, R., Binkley, J. S., Seeger, R., & Pople, J. A. (1980). Self-consistent molecular orbital methods. XX. A basis set for correlated wave functions. *The Journal of Chemical Physics*, 72(1), 650–654. <https://doi.org/10.1063/1.438955>
- Kuang, Y.-F., & Chen, Y.-H. (2004). Induction of apoptosis in a non-small cell human lung cancer cell line by isothiocyanates is associated with P53 and P21. *Food and Chemical Toxicology*, 42(10), 1711–1718. <https://doi.org/10.1016/j.fct.2004.06.009>
- Larkin, J. M. G., Hughes, S. A., Beirne, D. A., Patel, P. M., Gibbens, I. M., Bate, S. C., Thomas, K., Eisen, T. G., & Gore, M. E. (2007). A phase I/II study of lomustine and temozolomide in patients with cerebral metastases from malignant melanoma. *British Journal of Cancer*, 96(1), 44–48.
- Łaszcz, M., Kubiszewski, M., Jedynek, Ł., Kaczmarska, M., Kaczmarek, Ł., Łuniewski, W., Gabarski, K., Witkowska, A., Kuziak, K., & Malińska, M.

- (2013). Identification and Physicochemical Characteristics of Temozolomide Process-Related Impurities. *Molecules*, *18*(12), 15344–15356. <https://doi.org/10.3390/molecules181215344>
- Lee, J. W., & Cho, M. K. (2008). Phenethyl isothiocyanate induced apoptosis via down regulation of Bcl-2/XIAP and triggering of the mitochondrial pathway in MCF-7 cells. *Archives of Pharmacal Research*, *31*(12), 1604–1612. <https://doi.org/10.1007/s12272-001-2158-2>
- Lee, S. Y. (2016). Temozolomide resistance in glioblastoma multiforme. *Genes & Diseases*, *3*(3), 198–210. <https://doi.org/10.1016/j.gendis.2016.04.007>
- Lin, Z., Yang, R., Li, K., Yi, G., Li, Z., Guo, J., Zhang, Z., Junxiang, P., Liu, Y., Qi, S., & Huang, G. (2020). Establishment of age group classification for risk stratification in glioma patients. *BMC Neurology*, *20*(1), 310. <https://doi.org/10.1186/s12883-020-01888-w>
- Louis, D. N., Perry, A., Reifenberger, G., Von Deimling, A., Figarella-Branger, D., Cavenee, W. K., Ohgaki, H., Wiestler, O. D., Kleihues, P., & Ellison, D. W. (2016). The 2016 World Health Organization classification of tumors of the central nervous system: A summary. *Acta Neuropathologica*, *131*(6), 803–820.
- Middlemas, D. S., Stewart, C. F., Kirstein, M. N., Poquette, C., Friedman, H. S., Houghton, P. J., & Brent, T. P. (2000). Biochemical correlates of temozolomide sensitivity in pediatric solid tumor xenograft models. *Clinical Cancer Research*, *6*(3), 998–1007.
- Miwa, K., Ito, T., Yokoyama, K., & Shinoda, J. (2019). P14.08 Bevacizumab treatment for the lesion emerging after the radiotherapy for malignant glioma.

Neuro-Oncology, 21(Supplement_3), iii68–iii68.

<https://doi.org/10.1093/neuonc/noz126.244>

Mizuno, N. S., & Decker, R. W. (1976). Alteration of DNA by 5-(3-methyl-1-triazeno) imidazole-4-carboxamide (NSC-407347). *Biochemical Pharmacology*, 25(23), 2643–2647.

Moody, C., & Wheelhouse, R. (2014a). The Medicinal Chemistry of Imidazotetrazine Prodrugs. *Pharmaceuticals*, 7(7), 797–838.
<https://doi.org/10.3390/ph7070797>

Moody, C., & Wheelhouse, R. (2014b). The Medicinal Chemistry of Imidazotetrazine Prodrugs. *Pharmaceuticals*, 7(7), 797–838.
<https://doi.org/10.3390/ph7070797>

Morris, G. M., Huey, R., Lindstrom, W., Sanner, M. F., Belew, R. K., Goodsell, D. S., & Olson, A. J. (2009). AutoDock4 and AutoDockTools4: Automated docking with selective receptor flexibility. *Journal of Computational Chemistry*, 30(16), 2785–2791.

Murugavel, S., Ravikumar, C., Jaabil, G., & Alagusundaram, P. (2019). Synthesis, crystal structure analysis, spectral investigations (NMR, FT-IR, UV), DFT calculations, ADMET studies, molecular docking and anticancer activity of 2-(1-benzyl-5-methyl-1H-1, 2, 3-triazol-4-yl)-4-(2-chlorophenyl)-6-methoxypyridine—a novel potent human topoisomerase II α inhibitor. *Journal of Molecular Structure*, 1176, 729–742.

Newlands, E. S., Blackledge, G. R. P., Slack, J. A., Rustin, G. J., Smith, D. B., Stuart, N. S., Quarterman, C. P., Hoffman, R., Stevens, M. F. G., & Brampton,

- M. H. (1992). Phase i trial of temozolomide (CCRG 81045: M&B 39831: NSC 362856). *British Journal of Cancer*, *65*(2), 287–291.
- Newlands, E. S., Blackledge, G., Slack, J. A., Goddard, C., Brindley, C. J., Holden, L., & Stevens, M. F. (1985). Phase I clinical trial of mitozolomide. *Cancer Treatment Reports*, *69*(7–8), 801–805.
- Newlands, E. S., Stevens, M. F. G., Wedge, S. R., Wheelhouse, R. T., & Brock, C. (1997a). Temozolomide: A review of its discovery, chemical properties, pre-clinical development and clinical trials. *Cancer Treatment Reviews*, *23*(1), 35–61.
- Newlands, E. S., Stevens, M. F. G., Wedge, S. R., Wheelhouse, R. T., & Brock, C. (1997b). Temozolomide: A review of its discovery, chemical properties, pre-clinical development and clinical trials. *Cancer Treatment Reviews*, *23*(1), 35–61.
- Ostrom, Q. T., Cioffi, G., Gittleman, H., Patil, N., Waite, K., Kruchko, C., & Barnholtz-Sloan, J. S. (2019). CBTRUS statistical report: Primary brain and other central nervous system tumors diagnosed in the United States in 2012–2016. *Neuro-Oncology*, *21*(Supplement_5), v1–v100.
- Parr, R. G., & Yang, W. (1989). Density-functional theory of atoms and molecules Oxford Univ. Press. *Ed: Oxford*.
- Patel, A. P., Fisher, J. L., Nichols, E., Abd-Allah, F., Abdela, J., Abdelalim, A., Abraha, H. N., Agius, D., Alahdab, F., Alam, T., Allen, C. A., Anber, N. H., Awasthi, A., Badali, H., Belachew, A. B., Bijani, A., Bjørge, T., Carvalho, F., Catalá-López, F., ... Fitzmaurice, C. (2019). Global, regional, and national burden of brain and other CNS cancer, 1990–2016: A systematic analysis for

- the Global Burden of Disease Study 2016. *The Lancet Neurology*, 18(4), 376–393. [https://doi.org/10.1016/S1474-4422\(18\)30468-X](https://doi.org/10.1016/S1474-4422(18)30468-X)
- Ramirez, Y. P., Weatherbee, J. L., Wheelhouse, R. T., & Ross, A. H. (2013). Glioblastoma multiforme therapy and mechanisms of resistance. *Pharmaceuticals*, 6(12), 1475–1506.
- Rauhut, G., & Pulay, P. (1995). Transferable Scaling Factors for Density Functional Derived Vibrational Force Fields. *The Journal of Physical Chemistry*, 99(10), 3093–3100. <https://doi.org/10.1021/j100010a019>
- Reed, A. E., Curtiss, L. A., & Weinhold, F. (1988). Intermolecular interactions from a natural bond orbital, donor-acceptor viewpoint. *Chemical Reviews*, 88(6), 899–926. <https://doi.org/10.1021/cr00088a005>
- Shin, W.-H., Kim, J.-K., Kim, D.-S., & Seok, C. (2013). GalaxyDock2: Protein–ligand docking using beta-complex and global optimization. *Journal of Computational Chemistry*, 34(30), 2647–2656.
- St-Amant, A. (1996). Density functional methods in biomolecular modeling. *Reviews in Computational Chemistry*, 7, 217.
- Stevens, M. F. G., & Newlands, E. S. (1993). From triazines and triazenes to temozolomide. *European Journal of Cancer*, 29(7), 1045–1047.
- Stevens, M. F., Hickman, J. A., Langdon, S. P., Chubb, D., Vickers, L., Stone, R., Baig, G., Goddard, C., Gibson, N. W., & Slack, J. A. (1987). Antitumor activity and pharmacokinetics in mice of 8-carbamoyl-3-methyl-imidazo [5, 1-d]-1, 2, 3, 5-tetrazin-4 (3H)-one (CCRG 81045; M & B 39831), a novel drug with potential as an alternative to dacarbazine. *Cancer Research*, 47(22), 5846–5852.

- Stevens, M. F., Hickman, J. A., Stone, R., Gibson, N. W., Baig, G. U., Lunt, E., & Newton, C. G. (1984). Antitumour imidazotetrazines. 1. Synthesis and chemistry of 8-carbamoyl-3-(2-chloroethyl) imidazo [5, 1-d]-1, 2, 3, 5-tetrazin-4 (3H)-one, a novel broad-spectrum antitumor agent. *Journal of Medicinal Chemistry*, 27(2), 196–201.
- Szabo, A., & Ostlund, N. S. (2012). *Modern quantum chemistry: Introduction to advanced electronic structure theory*. Courier Corporation.
- Tolcher, A. W., Gerson, S. L., Denis, L., Geyer, C., Hammond, L. A., Patnaik, A., Goetz, A. D., Schwartz, G., Edwards, T., & Reyderman, L. (2003). Marked inactivation of O⁶-alkylguanine-DNA alkyltransferase activity with protracted temozolomide schedules. *British Journal of Cancer*, 88(7), 1004–1011.
- Trachootham, D., Zhang, H., Zhang, W., Feng, L., Du, M., Zhou, Y., Chen, Z., Pelicano, H., Plunkett, W., Wierda, W. G., Keating, M. J., & Huang, P. (2008). Effective elimination of fludarabine-resistant CLL cells by PEITC through a redox-mediated mechanism. *Blood*, 112(5), 1912–1922. <https://doi.org/10.1182/blood-2008-04-149815>
- Tsang, L. L. H., Farmer, P. B., Gescher, A., & Slack, J. A. (1990). Characterisation of urinary metabolites of temozolomide in humans and mice and evaluation of their cytotoxicity. *Cancer Chemotherapy and Pharmacology*, 26(6), 429–436. <https://doi.org/10.1007/BF02994094>
- Vennila, P., Govindaraju, M., Venkatesh, G., & Kamal, C. (2016). Molecular structure, vibrational spectral assignments (FT-IR and FT-RAMAN), NMR, NBO, HOMO-LUMO and NLO properties of O-methoxybenzaldehyde based

- on DFT calculations. *Journal of Molecular Structure*, *1111*, 151–156.
<https://doi.org/10.1016/j.molstruc.2016.01.068>
- Wang, Y., Jiang, Y., Wei, D., Singh, P., Yu, Y., Lee, T., Zhang, L., Mandl, H. K., Piotrowski-Daspit, A. S., Chen, X., Li, F., Li, X., Cheng, Y., Josowitz, A., Yang, F., Zhao, Y., Wang, F., Zhao, Z., Huttner, A., ... Mark Saltzman, W. (2021). Nanoparticle-mediated convection-enhanced delivery of a DNA intercalator to gliomas circumvents temozolomide resistance. *Nature Biomedical Engineering*. <https://doi.org/10.1038/s41551-021-00728-7>
- Wedge, S. R., Porteous, J. K., May, B. L., & Newlands, E. S. (1996). Potentiation of temozolomide and BCNU cytotoxicity by O6-benzylguanine: A comparative study in vitro. *British Journal of Cancer*, *73*(4), 482–490.
- Wedge, S. R., Porteous, J. K., & Newlands, E. S. (1996). 3-aminobenzamide and/or O6-benzylguanine evaluated as an adjuvant to temozolomide or BCNU treatment in cell lines of variable mismatch repair status and O6-alkylguanine-DNA alkyltransferase activity. *British Journal of Cancer*, *74*(7), 1030–1036.
- Wheelhouse, R. T., & Stevens, M. F. (1993). Decomposition of the antitumour drug temozolomide in deuteriated phosphate buffer: Methyl group transfer is accompanied by deuterium exchange. *Journal of the Chemical Society, Chemical Communications*, *15*, 1177–1178.
- Wiestler, O., Kleihues, P., & Pegg, A. E. (1984). O 6-alkylguanine-DNA alkyltransferase activity in human brain and brain tumors. *Carcinogenesis*, *5*(1), 121–124.

- Wu, X., Zhou, Q., & Xu, K. (2009). Are isothiocyanates potential anti-cancer drugs? *Acta Pharmacologica Sinica*, 30(5), 501–512.
<https://doi.org/10.1038/aps.2009.50>
- Yahiaoui, K., Seridi, L., & Mansouri, K. (2021). Temozolomide binding to Cucurbit[7]uril: QTAIM, NCI-RDG and NBO analyses. *Journal of Inclusion Phenomena and Macrocyclic Chemistry*, 99(1–2), 61–77.
<https://doi.org/10.1007/s10847-020-01027-5>
- Yang, P., Wang, Y., Peng, X., You, G., Zhang, W., Yan, W., Bao, Z., Wang, Y., Qiu, X., & Jiang, T. (2013). Management and survival rates in patients with glioma in China (2004–2010): A retrospective study from a single-institution. *Journal of Neuro-Oncology*, 113(2), 259–266.
<https://doi.org/10.1007/s11060-013-1103-9>
- Yuriev, E., Holien, J., & Ramsland, P. A. (2015). Improvements, trends, and new ideas in molecular docking: 2012–2013 in review. *Journal of Molecular Recognition*, 28(10), 581–604.
- Ziegler, Tom. (1991). Approximate density functional theory as a practical tool in molecular energetics and dynamics. *Chemical Reviews*, 91(5), 651–667.
<https://doi.org/10.1021/cr00005a001>

List of Publications

1. **Dipanta Gogoi**, Lalmalsawmtluangi and Zodinpuia Pachuau. Theoretical Study on the Mechanism of Alkylation At 0-6 Position of Guanine by Temozolomide and Bitc-Temozolomide. *Science & Technology Journal*, 6(2), 68–74.
2. Lalhruaizela, Brilliant N. Marak, **Dipanta Gogoi**, Jayanta Dowarah, Balkaran S. Sran, Zodinpuia Pachuau, Ved Prakash Singh. Study of supramolecular self-assembly of pyridone and dihydropyridone co-crystal: Synthesis, crystal structure, Hirshfeld surface, DFT and molecular docking studies. *Journal of Molecular Structure*, 1235, 130214.

Conferences and Symposium

1. ***Electronic and Spectroscopic study of Taxifolin by Density Functional Theory.*** International Seminar on Recent Advances in Science and Technology (ISRAST). 16th -18th November 2020). Organised by NEAST, Mizoram University, Aizawl-796004, Mizoram (India)
2. ***Theoretical investigation of structure, anticancer activity and molecular docking of temozolomide derivatives.*** International Conference on Fundamental and Applied Science s(ICFAS2021). From March 24-26, 2021. Organised by Faculty of Science and I.Q.A.C., Bharatiya Vidya Bhavan's. Mumbai (Affiliated to University of Mumbai).
3. ***A Density Functional Theory study of Temozolomide, an alkylating anti cancer drug.*** Mizoram Science Congress 2020. Dec 3-4, 2020, Mizoram science congress 2020(online). Organised by MISTIC, DST, Planning Department, Govt. of Mizoram.
4. ***DFT study of Apegenin, Myricetin and Cyanidin with the Docking Analysis as a Potent Inhibitors of Influenza H1N1 Virus Neuraminidase.*** February 13-15,2020. Organised By Department of Chemistry, Gauhati University, Guwahati, Assam

Theoretical Study on the Mechanism of Alkylation At O-6 Position of Guanine by Temozolomide and Bitc-Temozolomide

Dipanta Gogoi¹, Lalmalsawmtluangi² and Zodinpuia Pachuau^{3*}

^{1,2,3}Department of Chemistry, Mizoram University

Email: *zodinpuia@rediffmail.com

Abstract—Temozolomide, an alkylating prodrug mainly used in the treatment of malignant glioblastoma (brain cancer). However, after giving dose of TMZ, there is a chance of reappearance of cancer cell after few days. The purpose of this study is to shed more light on mechanism of alkylation at O-6 position of guanine by TMZ and BITC-TMZ through computationally. This study will lead to gain of useful information of drug design and development. Along with the geometrical optimization using density functional theory, MEP and FMO parameters are also calculated. As the alkylation takes place at the O-6 of guanine of DNA. Therefore, this study mainly focus on the guanine structures. The physiological properties of BITC-TMZ is found to be similar with the TMZ.

INTRODUCTION

Temozolomide (TMZ), an alkylating agent, is widely used for treating primary and recurrent high-grade gliomas. However, the ability of TMZ is often limited by the development of MGMT resistance (Yan *et al.*, 2016; Zhang *et al.* 2012). According to a survey in China, ~70% of primary malignant brain tumours occurred due to malignant glioma which cause severe damage to human health (Zhang *et al.*, 2013). TMZ is a novel type of glioma therapeutic drug which is able to penetrate the blood-brain barrier to exert targeted therapeutic effects on brain tumour tissue (Gai *et al.*, 2016). However, TMZ resistance is a major problem in malignant glioma. The cytoprotective DNA repair protein, O6-alkylguanine-DNA alkyltransferase (AGT) transfers the methyl group from methyl adducts at O6-guanine to an cysteine acceptor residue (Pegg 1990).

So, the modification of the 3-substituent of temozolomide, enabling group transfer to DNA G06 sites. The apparent anticipation as a poor substrate to MGMT or deficient of MGMT, and thus be susceptible to recognition or DNA repair by the protein will be chemically reassured as far as possible (Stevens *et al.*, 1984).

Benzyl isothiocyanate (BITC) shows a promising anticancer properties against a variety of human and murine tumour

cell lines (Hirose *et al.*, 1998; Pintão *et al.*, 1995). A computer-aided drug design (CADD) technology has been study on BITC-TMZ with alkylglycerone phosphate synthase and the result has been found accordance to the prediction of CADD (Yang *et al.*, 2018).

MATERIALS AND METHODS

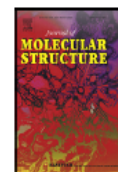
In this work, computational works were performed using GAUSSIAN 16 (Gaussian 16, Revision A.03, *et al.* n.d.), which is the latest repetition of a graphical interface used with Gaussian. It helps in the creation of Gaussian input files, enables the user to run Gaussian calculations from a graphical interface (GaussView) without the need for using a command line instruction, and helps in the interpretation of Gaussian output. All the structures were optimized at the B3LYP (Gill *et al.* 1992) method using the standard AM1, 6-31++G(d), 6-31++G(d,p), 6-311++G(d), 6-311++G(d,p) basis sets to obtain the results. The bond angles, bond length and dihedral angles of all the structures are also determined using the Gaussian. The Molecular Electrostatic Potential (MEP) and Frontier Molecular Orbital (FMO) of the molecule is done in the same basis set and visualized by Gaussview 6 (GaussView 6.0.16 n.d.)

DOI: 10.22232/stj.2018.06.02.12



Contents lists available at ScienceDirect

Journal of Molecular Structure

journal homepage: www.elsevier.com/locate/molstr

Study of supramolecular self-assembly of pyridone and dihydropyridone co-crystal: Synthesis, crystal structure, Hirshfeld surface, DFT and molecular docking studies

Lalhruaizela^a, Brilliant N. Marak^a, Dipanta Gogoi^a, Jayanta Dowarah^a, Balkaran S. Sran^b, Zodinpuia Pachuau^a, Ved Prakash Singh^{a,*}

^aDepartment of Chemistry, School of Physical Sciences, Mizoram University, Aizawl-796004, Mizoram, India
^bDepartment of Chemistry, Guru Nanak Dev University, Amritsar, Punjab 143005, India

ARTICLE INFO

Article history:

Received 29 November 2020
 Revised 25 February 2021
 Accepted 25 February 2021
 Available online 5 March 2021

Keywords:

Non-covalent interactions
 Docking
 Intra-molecular
 Intermolecular
 DFT
 Hirshfeld
 Crystal

ABSTRACT

Dihydropyridone is synthesized by the multi component condensation reactions (MCRs), followed by three different oxidation methods to synthesize pyridone. The 3-D self-assemblies of both the compounds were determined using the single-crystal X-ray diffraction method. Dihydropyridone products are found as a racemic mixture in synthesis and crystallized as co-crystal. Similar structural conformations are observed in both the compounds but stabilized with different non-covalent interactions. Hirshfeld surface analysis is done to analyze the various intermolecular interactions in both the structure. This study gives the clue of driving force in the self-assembly of molecules in crystal lattices. The propensity of inter-molecular contacts to construct the supramolecular assembly was further studied using DFT. The geometrical optimizations of both the compounds were done by the electronic structure method using density functional theory (DFT) to identify the active sites and explore the molecules' chemically reactive parameters. Further, both compounds were docked with Survivin Protein and Kinesin Eg5 protein to analyze the binding affinity with targeted protein.

© 2021 Elsevier B.V. All rights reserved.

Introduction

Dihydropyrimidinones (DHPM's) and their derivatives are heterocyclic compounds synthesized by multicomponent reactions [1,2]. This class of compounds are structural analogs of monastrol became important to the field of medicinal chemistry because monastrol is a very important bio-molecule having many biological activities [3]. Other DHPMs analogs have been synthesized since then, revealing several other pharmacological properties [4]. Monastrol is the protagonist of the DHPMs class. Several studies have revealed that its inhibitory action on human kinesin Eg5 leads to mitotic arrest and, consequently, to apoptosis [5]. At first, this was the main action described for this class of compounds, but some studies have shown other possible targets for these molecules, such as centrin [6], calcium channels [7] and topoisomerase I [8].

2-pyridones are a particular class of compounds with unique pharmacophores that exhibit several biological activities such as analgesic [9], antimalarial [10], antitumoral [11], anti-HIV [12], and

anti-inflammatory [13]. Cyanopyridines are important intermediates for synthesizing many biological important analogs like nicotinamide, nicotinic acid, and isonicotinic acid. 3-cyano-2-pyridone are very significant frameworks in the past few decades. These are the structural basis of the alkaloid ricinine, the first known cyano group-containing alkaloid. Milrinone is also a 3-cyano-2-pyridone derivative used for the treatment of congestive heart failure [14,15]. Some derivative of 3-cyano-2-pyridone has shown anticancer activity [16–18]. 3-cyano-4,6-diaryl-2-pyridone derivatives I and IV (Fig. 1) possess anticancer activity due to their ability to act as survivin inhibitors [19]. Undoubtedly, the need to bridge the gap between minimizing side effects and the mode of action of antimitotic drugs encourage us for further investigations towards the synthesis of the novel potent cytotoxic compound [20,21].

New analogs are designed based on Monastrol kinesin inhibitor and Survivin inhibitor pharmacophore analysis and bio-isoster group application (Fig. 2).

Given the pharmacological importance of 2-pyridone derivatives, the investigations of their structural and electronic properties are fundamental to know the influence of different groups in the molecule to discover the relationship of these groups with their biological properties [22–26].

* Corresponding author.

E-mail address: vedsinghbhu@gmail.com (V.P. Singh).

BIO-DATA

- 1. NAME** : Dipanta Gogoi
- 2. DATE OF BIRTH** : 25 Dec 1992
- 3. FATHER'S NAME** : Chandra Kanta Gogoi
- 4. PERMANENT ADDRESS** : Sivasagar, Assam, 785640
- 5. EMAIL ADDRESS** : dipantagogoi06@gmail.com

5. EDUCATIONAL QUALIFICATIONS

Examination passed	Year of Passing	Board/ University	Registration No.	Class/ Division	% of Marks	Subjects
High School Leaving Certificate Examination	2008	Board of Secondary Education, Assam	23V/0806/012371/06	I	78.8	Maths, Eng, Sci, S. sci, Adv Math, Hin
Higher Secondary School Leaving Certificate Examination	2010	Assam Higher Secondary Education Council	21-B-076295 YR 2008-2009	I	65.4	Chem, Phy, Maths, Biolg, Eng, Alt. Eng
B. Sc.	2013	Dibrugarh University (Assam)	11003336	I	60.9	Chem(M), Phy, Maths, Eng, Env Sci
M.Sc	2015	Mizoram university	88 of 2014	I	70.2	Org Chem(spl), Ing chem, Phy chem, Anal chem

PARTICULARS OF THE CANDIDATE

NAME OF CANDIDATE : Dipanta Gogoi
DEGREE : Doctor of Philosophy (Ph.D)
DEPARTMENT : Chemistry
TITLE OF THESIS : Computational Probe of an Alkylating
Prodrug: Temozolomide and its Derivatives.
DATE OF ADMISSION : 13/08/2016
APPROVAL OF RESEARCH PROPOSAL:
1. BOS : 2nd May, 2017
2. SCHOOL BOARD : 15th May, 2017
MZU REGN. NO. : 88 of 2014
Ph.D REGN. NO. & DATE : MZU/Ph.D/1006 of 15.05.2017
EXTENTION : NIL

Head
Department of Chemistry

ABSTRACT

**COMPUTATIONAL PROBE OF AN ALKYLATING PRODRUG:
TEMOZOLOMIDE AND ITS DERIVATIVES**

**A THESIS SUBMITTED IN PARTIAL FULFILLMENT OF THE
REQUIREMENTS FOR THE DEGREE OF DOCTOR OF
PHILOSOPHY**

DIPANTA GOGOI

MZU REGISTRATION NO. : 88 of 2014

Ph.D.REGISTRATION NO. : MZU/Ph.D/1006 of 15.05.2017



**DEPARTMENT OF CHEMISTRY
SCHOOL OF PHYSICAL SCIENCES
AUGUST, 2022**

**COMPUTATIONAL PROBE OF AN ALKYLATING PRODRUG:
TEMOZOLOMIDE AND ITS DERIVATIVES**

BY

DIPANTA GOGOI

Department of Chemistry

Under the supervision of

Dr. ZODINPUIA PACHUAU

Submitted

In partial fulfillment of the requirement of the Degree of Doctor of Philosophy in
Chemistry of Mizoram University, Aizawl.

ABSTRACT :

The most frequently diagnosed primary tumor in the central nervous system is glioma, further classified as astrocytoma, oligodendroglioma, or ependymoma, depending on histological and genetic features. The annual incidence of malignant gliomas is about 5 cases per 100,000 person-years. The most common of all malignant central nervous system (CNS) tumors is glioblastoma multiform (GBM; 48.3%), which accounts for approximately 41.8% to 57.3% of gliomas.

Temozolomide (TMZ) is a DNA alkylating agent that was first discovered to have anti-tumorigenic effects in the 1940s and became the first drug used in chemotherapeutics. TMZ is a second-generation imidazotetrazine alkylating prodrug used to treat glioblastoma. However, TMZ's cytoprotective DNA repair alkyltransferase (AGT) resistance efficacy in malignant glioma creates a major problem.

One issue with using TMZ to treat GBM patients is that their tumors may evolve TMZ resistance due to alteration in their expression of DNA alkylating proteins, DNA repair enzymes, and cell signaling pathways.

The present work focused on the detailed study of the electronic and spectroscopic properties of Temozolomide (TMZ) and its benzyl isothiocyanate derivatives (BITC). The structures were optimized in the gas phase and aqueous solution with the hybrid B3LYP/6-311++G(d,p) basis set using Gaussian 16 (Revision A.03) program. Natural population analysis (NPA), Molecular electrostatic potential (MEP), and stabilization energy were predicted with the same level of theory in both media using version 3.1 of the NBO (version 3.1) program. The GaussView program was employed to generate the mapped MEP surface. The electronic spectrum in the aqueous medium was predicted by using the Time-dependent DFT (TD-DFT) calculations. The frontier orbitals were calculated to predict reactivities in both phases. In contrast, the behaviours in both phases were assessed using reactivity descriptors such as chemical potential (μ), global hardness (η), electronegativity (χ), global electrophilicity index (ω), global softness (S), and nucleophilicity indexes (E).

Chapter 1 includes the background of Glioblastomamultiforme, the introduction of TMZ, the Chemistry of TMZ bio-synthesis, resistance mechanisms and literature review.

Chapter 2 contains the theoretical methodology used in this work. Gaussian 16, along with Gaussview, which is a visualizing software, have been used to analyse the Gaussian output files. Autodock 4.2.6 software is used, which is available under the Apache License and is currently maintained by The Scripps Research Institute. The conceptual method is to find the correct binding poses and to accurately predict the binding affinity between the ligand and the targeted protein.

Chapter 3 and **Chapter 4** includes the theoretical study of TMZ and TMZ-BITC derivatives. The TMZ's Potential Energy Surface revealed that the structure is more stable when the amine group is opposite the tetrazine ring. The complete vibrational studies and chemical shift data agree well with the experiment data. NBO analysis showed that the intramolecular charge transfer within the molecule was primarily from the lone pairs of the electrons in N-atom and O-atom.

Chapter 5 entails pharmacological and molecular docking investigations. Molecular docking was performed with the crystal structure of the target protein complex PDB ID: IQH4 with TMZ and its derivatives. Molecular docking studies revealed that the TMZ-BITC(3) with the lesser binding energy of -8.6 kcal/mol has inhibitor effects than TMZ and its derivatives. The *in silico* biological activity results suggest predicted using the PASS and CLC-Pred database suggested that all the compounds possess relatively anticancer activity, mostly of apoptosis and antineoplastic.

Chapter 6 is the summary and conclusion of our research work.

In summary, the present treatise deals with electronic and spectroscopic studies of TMZ and its BITC derivatives.

We hope that our research will aid in the development and synthesis of new TMZ derivatives.